AD-A088 226   SYSTEMS RESEARCH LABS INC   DAYTON OH RESEARCH APPLICA--ETC F/8 20/5
ADVANCED CONCEPTS IN CLOSED-CYCLE LASERS.(U)
MAR 80   R A OLSON, D F GROSJEAN   F33615-76-C-2177
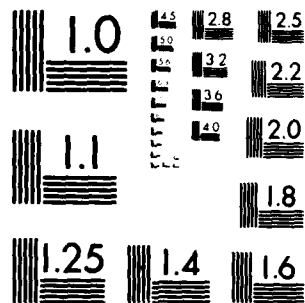UNCLASSIFIED   AFWAL-TR-80-2026   NL

1 of 2

AD
A088 226

MICROCOPY RESOLUTION TEST CHART
NATIONAL BUREAU OF STANDARDS 1963 A

AFWAL-TR-80-2026

LEVEL

ADVANCED CONCEPTS IN CLOSED-CYCLE LASERS

ROBERT A. OLSON
DENNIS F. GROSJEAN

RESEARCH APPLICATIONS DIVISION
SYSTEMS RESEARCH LABORATORIES, INC.
2800 INDIAN RIPPLE ROAD
DAYTON, OHIO 45440

MARCH 1980

DTIC
ELECTED
AUG 19 1980
A

AERO PROPULSION LABORATORY
AIR FORCE WRIGHT AERONAUTICAL LABORATORIES
AIR FORCE SYSTEMS COMMAND
WRIGHT-PATTERSON AIR FORCE BASE, OHIO 45433
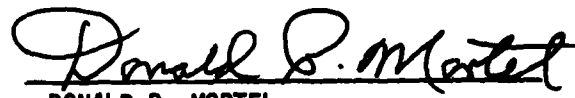
AD A088226

DDC FILE COPY

80 8 19 005

This technical report has been reviewed and is approved for publication.

PETER RLETZINGER
Project Engineer

DONALD P. MORTEL
Actg Chief, Energy Conversion Branch
Aerospace Power Division

FOR THE COMMANDER

JAMES D. REAMS
Chief, Aerospace Power Division
Aero Propulsion Laboratory

REPORT DOCUMENTATION PAGE	READ INSTRUCTIONS BEFORE COMPLETING FORM

1. REPORT NUMBER	2. GOVT ACCESSION NO.	3. RECIPIENT'S CATALOG NUMBER
AFWAL-TR-80-2026	AD-A088 226	

4. TITLE (and Subtitle)	5. TYPE OF REPORT & PERIOD COVERED
ADVANCED CONCEPTS IN CLOSED-CYCLE LASERS	Final Technical Report, 6 Dec 1976 — 30 Sep 1979
	6. PERFORMING ORG. REPORT NUMBER

7. AUTHOR(s)	8. CONTRACT OR GRANT NUMBER(s)
Robert A. Olson Dennis F. Grosjean	F33615-76-C-2177

9. PERFORMING ORGANIZATION NAME AND ADDRESS	10. PROGRAM ELEMENT, PROJECT, TASK AREA & WORK UNIT NUMBERS
Systems Research Laboratories, Inc. 2800 Indian Ripple Road Dayton, OH 45440	2301 Task S2 Work Unit 01

11. CONTROLLING OFFICE NAME AND ADDRESS	12. REPORT DATE
Aero Propulsion Laboratory Air Force Wright Aeronautical Laboratories (AFWAL/POOC), Wright-Patterson AFB, OH 45433	March 1980
	13. NUMBER OF PAGES
	187

14. MONITORING AGENCY NAME & ADDRESS(if different from Controlling Office)	15. SECURITY CLASS. (of this report)
187	UNCLASSIFIED
	15a. DECLASSIFICATION/DOWNGRADING SCHEDULE

16. DISTRIBUTION STATEMENT (of this Report)

Approved for public release; distribution unlimited

17. DISTRIBUTION STATEMENT (of the abstract entered in Block 20, if different from Report)

18. SUPPLEMENTARY NOTES

19. KEY WORDS (Continue on reverse side if necessary and identify by block number)

Closed-cycle laser, recirculating loop, annular-flow return, velocity profile, ultrahigh vacuum, He-Xe laser, CO_2 laser, XeCl laser, high repetition rate, laser lifetime, preionization, thyratron, spark source, photoabsorption, photoionization, photoexcitation, mercury halides.

20. ABSTRACT (Continue on reverse side if necessary and identify by block number)

The status of closed-cycle-laser technology is reviewed. The technology and performance of closed-cycle lasers in a recirculating loop and in a novel annular-flow-return configuration are discussed. High-repetition-rate laser operation has been achieved in high-pressure mixtures of Ar:Xe, Ne:Xe, He:Xe, He:Kr, He:Ar, and CO_2:CO:Xe:He. New laser lines at 5.13 and 5.44 μ have been observed for the He-Xe laser which generated a maximum average laser output power of 5.1 W at 9.5 kHz. Closed-cycle

DD FORM 1473 EDITION OF 1 NOV 65 IS OBSOLETE

XeCl laser operation employing a recirculating-loop configuration is discussed. Previously measured laser-seeding-agent photoabsorption cross sections and photoionization yields have been verified. Absolute measurements of UV emission from a CO spark source and measurements of UV emission from a $CO_2:N_2:He$ capillary discharge have been made. A sliding spark and a dielectric-coupled discharge have been investigated as laser-preionization sources. Mercury-halide photolytic excitation studies have been made, and $HgBr_2$ photoabsorption cross sections have been measured.

PREFACE

This final report was prepared by the Research Applications Division of Systems Research Laboratories, Inc., under Contract No. F33615-76-C-2177, Project 2301, Task S2, Work Unit 01, with Dr. Peter Bletzinger as Government Project Monitor. The research was conducted by Mr. Robert A. Olson, Mr. Dennis F. Grosjean, and Mr. Benjamin Sarka, Jr.

This research was funded jointly by the AFWAL Aero Propulsion Laboratory and the Air Force Weapons Laboratory, with partial support being given by the Avionics Laboratory.

TABLE OF CONTENTS

TABLE OF CONTENTS (Cont'd)

LIST OF ILLUSTRATIONS (Cont'd)

LIST OF ILLUSTRATIONS (Cont'd)

LIST OF ILLUSTRATIONS (Cont'd)

SECTION I

INTRODUCTION

Efficient high-power lasers in the UV, visible, and IR are needed for a wide spectrum of Air Force applications. The type of laser having the greatest potential for development in these areas is the pulsed gas laser operating at medium to high pressure (50 Torr to several atmospheres). High-pressure operation results in high-peak-power output and large pressure-broadened linewidths (tunability). High average power is achievable by increasing the pulse repetition rate; this, however, requires a fast gas flow which increases the complexity of the laser system considerably. In addition to satisfying high-average-power requirements, a practical fast-flow high-pressure gas laser must be capable of economical and reliable operation for long periods of time (at least hours). This demands the closed-cycle mode of operation.

This report describes the results of (1) studies to improve the performance, reliability, and lifetime of closed-cycle lasers and (2) an investigation of improved methods of photoionization in UV-preionized discharges. The following aspects of closed-cycle lasers were studied: (1) performance with Xe-buffer gas mixtures and with CO_2-laser gas mixtures, (2) aerodynamics of recirculating-flow systems, (3) electrical pulse excitation and power conditioning, and (4) operation with corrosive gases.

The status of closed-cycle laser technology is discussed in Section II. The current state of development of cw CO_2, pulsed CO_2, pulsed Xe, and pulsed rare-gas-halide closed-cycle lasers is described.

Studies carried out on a high-repetition-rate, closed-cycle, fast-flow, transversely excited laser,[1] developed under AF Contract F33615-73-C-4130, are described in Section III. Details of the design and performance of a compact closed-cycle laser utilizing a novel recirculating-flow configuration (annular flow return) are given in Section IV. Both of these laser systems permitted investigation of laser media excited by short (100 ns), fast-rising (30-ns) high-voltage (10-20 kV) pulses under conditions of high pressure, recirculating flow, and low-background-impurity level. The systems exhibited long laser-gas-fill lifetime as a result of the ultrahigh-vacuum materials and techniques used in their construction.

Section V is a discussion of closed-cycle XeCl laser operation employing the recirculating loop used for the studies of Section III. Measurements of the UV emission and absorption of various types of gas discharges are presented in Section VI. Section VII contains a discussion of metal-halide photoexcitation and measurements of $HgBr_2$ photoabsorption cross sections.

SECTION II

STATUS OF CLOSED-CYCLE LASER TECHNOLOGY

Since the inception of the gas-dynamic laser in 1963,[2] gas flows have been used with great success for the convective mixing and cooling of laser media and for the production of population inversions during rapid gas expansion. The outstanding feature of the convectively cooled laser is the proportionality of average laser output power to mass flow rate. The average output of lasers employing static or slowly flowing gas is proportional to length and is limited by diffusion cooling to the walls. As pointed out by Wilson,[3] the maximum average power density obtainable from a laser is

$$\frac{P}{V} = \left(\frac{\eta}{1-\eta}\right) \frac{NE}{\tau} \qquad (1)$$

where η = laser efficiency, N = gas density, E = waste energy, and τ = waste energy removal time. The power ratio in the convection and diffusion cases is

$$\frac{P_{conv}}{P_{diff}} = \frac{\tau_{diff}}{\tau_{conv}} = \frac{d}{\lambda} \frac{v_F}{v_T} \qquad (2)$$

where d = width of laser interaction region, λ = mean free path, v_F = flow velocity, and v_T = thermal velocity. For room temperature CO_2 at a pressure of 20 Torr, d = 1 cm and v_F = 30 m/sec, the ratio is approximately 500. The maximum average laser power obtainable from a convectively cooled laser is

$$P = \left(\frac{\eta}{1-\eta}\right) \dot{m} c_p \Delta T \qquad (3)$$

where $\dot{m}$ = mass flow rate, c_p = specific heat of gas, and ΔT = temperature rise of gas.

The development of compact high-average-power gas lasers has been based on the use of fast-flow high-pressure laser media. The large mass flow rates required to achieve high repetition rates in pulsed lasers or medium-to-high average power in cw or pulsed lasers mandate closed-cycle operation. Recirculation of the laser medium avoids the considerable gas-handling facilities required to supply and exhaust large quantities of gas. It also significantly improves the economics of operation. This is particularly true of isotopic gases for which convective cooling is economically feasible only in the closed-cycle mode of operation. In the case of toxic and/or corrosive laser media, safety requirements are met much more easily with closed- than with open-cycle operation.

This review covers four types of closed-cycle lasers: 1) cw CO_2, 2) pulsed CO_2, 3) pulsed Xe, and 4) pulsed rare-gas halides. The pulsed lasers utilize line-type pulsers which generate pulses on the order of 100 ns or less. The class of CO_2 lasers having long pulses on the order of microseconds and exemplified by the e-beam sustainer discharge is not covered here. The long-pulse CO_2 lasers have two to three times the energy loading of the short-pulse CO_2 lasers; closed-cycle operation of these lasers has not been reported in the literature.

Examples of various configurations which have been employed for closed-cycle lasers are found in Refs. 1, 4, and 5. In the master oscillator-power amplifier configuration of Hill's[4] electro aerodynamic cw CO_2 laser, the TEM_{oo} mode beam from a 200-W oscillator made 17 passes through the gain medium. Roots blowers were used to circulate gas through

4

the $5.6 \times 76 \times 100$ cm^3 discharge channel at flow rates up to 21,000 CFM. Turbulence introduced into the flow upstream of the anode promoted the formation of a large-volume, uniform-glow discharge. The discharge was established, in line with the flow, between an individually ballasted multi-pin anode and a wire-array cathode.

The closed-cycle rare-gas electric-discharge laser of Ref. 1 was used in the study of He-Xe and Ar-Xe lasers. In order to establish and maintain a high-purity laser medium, this system was constructed entirely from ultra-high-vacuum components, including a vaneaxial fan externally driven through a ferrofluidic rotary vacuum seal, and research-grade gases were used. Transverse double-discharge excitation using Rogowski electrodes and pre-ionization wires at the electrode midplane was employed. A high-repetition-rate pulser drove the laser discharge via a thyratron-switched, low-inductance energy-storage capacitor charged through a tetrode pulse modulator. A 7-ft-long flow loop (6-in. diam) with a circuit length of 16 ft was used.

In Fahlen's[5] closed-cycle KrF laser, a vaneaxial fan was used to circulate the gas through two rail electrodes (2-cm gap × 70 cm long) at up to 100 m/s. The transverse discharge was excited by a thyratron-switched LC inversion generator utilizing storage capacitors comprised of parallel arrays of coaxial cables. Corona from a dielectric-covered wire adjacent to the cathode provided preionization concurrent with the discharge pulse. The system was about 6 ft long.

An overview of the closed-cycle cw CO_2 lasers which have been reported in the literature is given in Table 1. The lasers are listed chronologically, beginning with the first fast-flow closed-cycle laser reported by Tiffany, et al.,[6] in 1969. All of these lasers utilized discharges transverse to

Table 1

CLOSED-CYCLE CW CO$_2$ LASERS

REFERENCE	OUTPUT POWER (kW) (W/cm^3)	EFF. (%)	PRESSURE (Torr)	FLOW	DISCHARGE DIMENSIONS (cm)	COMMENTS
Tiffany, et al. (1969)	1 0.9 Single-Pass Osc.	6 (Overall)	20	30 m/s 0.15 lb/s	100 4 cm^2 Beam	Gas Makeup
Hill (1971)	19 0.45 200-W Input 17-Pass Amp.	24	50	230 m/s 0.55 lb/s	5.6 × 100 × 76	
Rabe (1978)	15 0.35 250-W Input	10	50	230 m/s 0.55 lb/s	5.6 × 100 × 76	2-s Shot (Window Limit) 15 Shot Hr
Seguin and Sedgwick (1972)	0.2 0.18 Double-Pass Osc.	5 (Overall)	11	40 m/s 0.015 lb/s	3.8 × 8.3 × 36	
Brown and Davis (1972)	27.2 0.33 150-W Input 11-Pass Amp.	17.2	30	110 m/s 1 lb/s	6.3 × 53 × 244	27.2 kW After Continuous Run of ~ 1 hr
Hoag, et al. (1974)	17 Unstable Res.	6.8 (Overall)				5 SCFM Gas Makeup
Lancashire, et al. (1976)	6 1.11 Unstable Res.	8	160	160 m/s 1.6 lb/s	5 × 9 × 120	Up to 31 min.
Seguin, et al. (1978)	1.2 0.3 Multipass Hole-Coupled	3.7	50	50 m/s 0.09 lb/s	6 × 13 × 50	Stable Sealed Off Operation for Several hr

the flow, except those of Hill[4] and Brown and Davis[7] which used in-line discharges and MOPA configurations. Hill's data are atypical for that particular laser, and data which are more representative for the same laser have been obtained recently by Rabe.[8] A rich variety of technology has been applied in achieving the results of Table 1. Tiffany, et al.,[6] used a rod to multi-strip anode discharge in a vaneaxial-fan-driven recirculating flow. Seguin and Sedgwick[9] used a modified centrifugal compressor from an aircraft supercharger to provide gas flow and a discharge with individually ballasted multiple hollow cathodes and a multi-pin anode. Brown and Davis[7] utilized an individually ballasted multi-pin cathode, cylindrical anodes at top and bottom of the flow channel, an auxiliary rf discharge perpendicular to the dc discharge, and individually adjustable flow-conditioning vanes[10] upstream of the cathode. Hoag, et al.,[11] used an e-beam sustainer-type discharge. Lancashire, et al.,[12] in order to avoid the use of makeup gas, constructed their system from high-vacuum components, including a centrifugal blower (6-ft.-diam. impeller) externally driven through a ferrofluidic seal. They used a pin-to-plane discharge having an individually ballasted multi-pin cathode. Seguin, et al.,[13] used a flow system similar to that of Seguin and Sedgwick and a pulser-sustainer[14,15] type of discharge with photopreionization provided by a UV spark array situated behind a transparent anode.

The Brown and Davis laser exhibited the best performance of the lasers listed in Table 1 with 27.2 kW laser output at 17.2% electrical-to-optical conversion efficiency. Even more significant is the achievement of this power after a continuous run of 1 hr, during which the output power was greater than 20 kW for 30 min.

The laser-output-power/mass-flow-rate data of Table 1 are plotted in Fig. 1. This plot does show (except for Lancashire's data) that laser output power is approximately proportional to mass flow rate, as predicted by Eq. (3). Lancashire's results were obtained at a pressure of 160 Torr; the other data were obtained at pressures in the 10-50 Torr range. This indicates that Lancashire did not use his mass flow efficiently and should have been able to achieve the same output power at much lower pressure.

The inherent limitation to the output power density of any gas laser is the power-loading level at which the glow-to-arc transition occurs. Examination of the power-loading data for the lasers in Table 1 reveals that the input power density is inversely proportional to the gas residence time in the discharge volume. This is shown in Fig. 2 where τ_R is the gas residence time. It is assumed that each laser was power loaded to a maximum level beyond which arcing occurred (except for the Seguin and Sedgwick laser which apparently was greatly underloaded). These data are replotted in Fig. 3 where they are compared with the data of Wiegand and Nighan[16] who studied the influence of gas residence time and turbulence upon the power density threshold for glow collapse. The cross-hatched region represents the data Wiegand and Nighan obtained for various turbulence generators upstream of the cathode of a discharge in 80-Torr $CO_2:N_2:He$ (0.5:0.35:0.6). Nighan and Wiegand's interpretation[17] of these findings is that glow collapse occurs at a power density where the growth time of a vibrational instability becomes comparable to the gas residence time. A vibrational instability is the temporal amplification of disturbances in vibrational temperature which are driven by the large response of electron density to the initial gas-density disturbance.

8
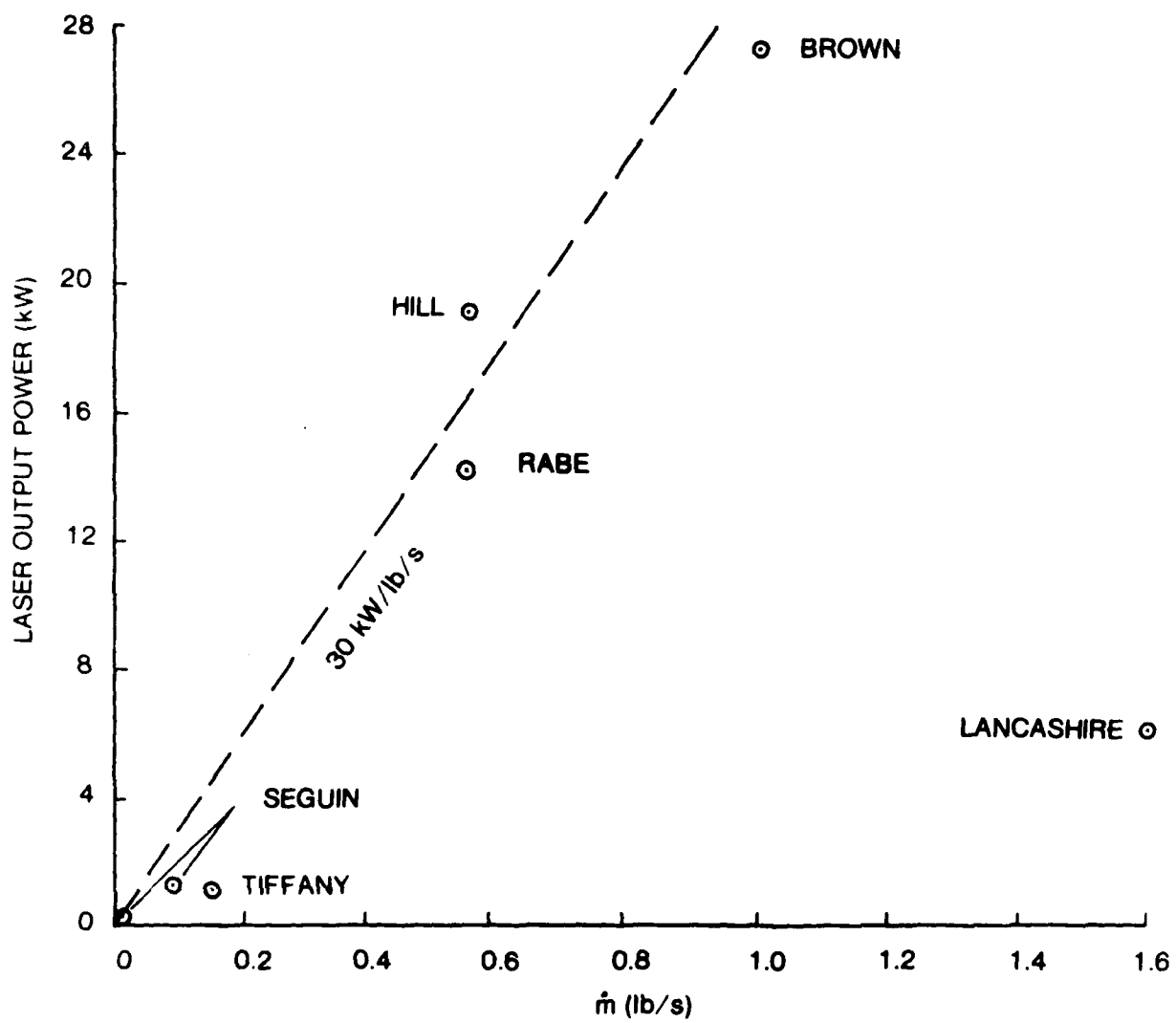
Figure 1. Closed-cycle cw CO_2 laser output vs. mass flow rate.
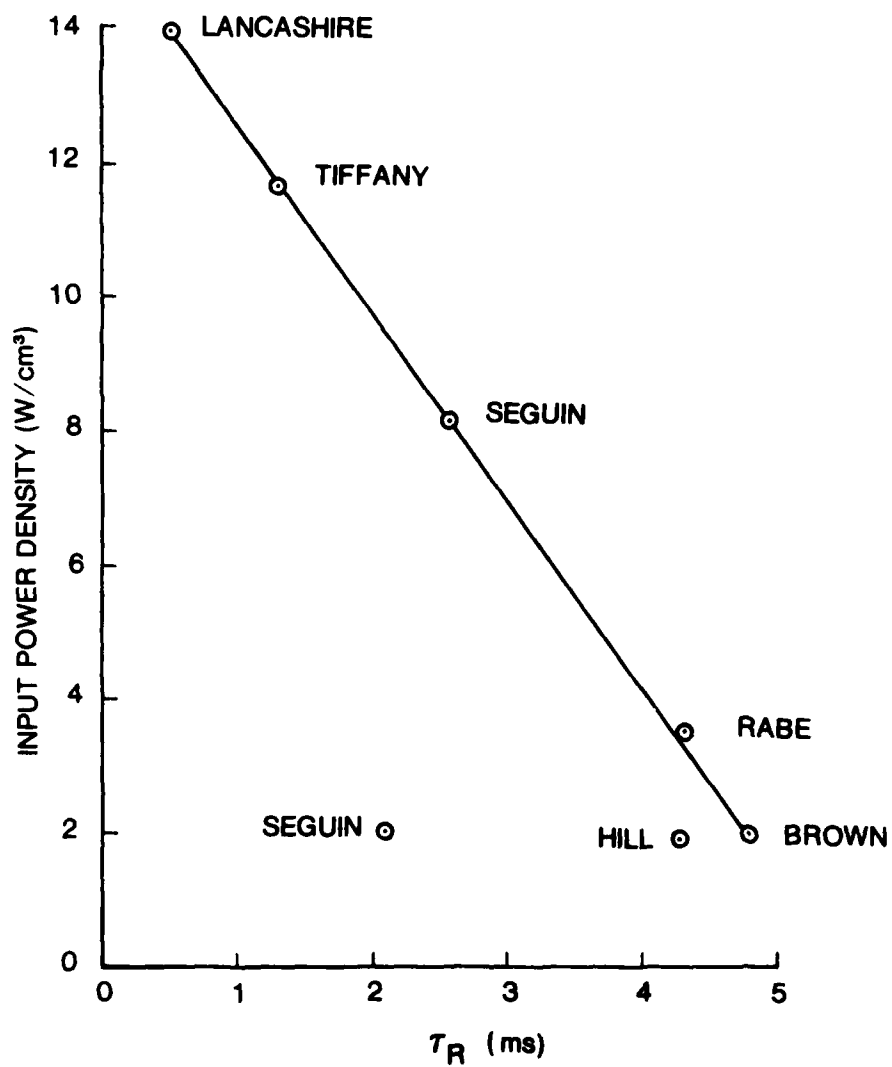
Figure 2. Closed-cycle cw CO_2 laser input power density vs. gas residence time.
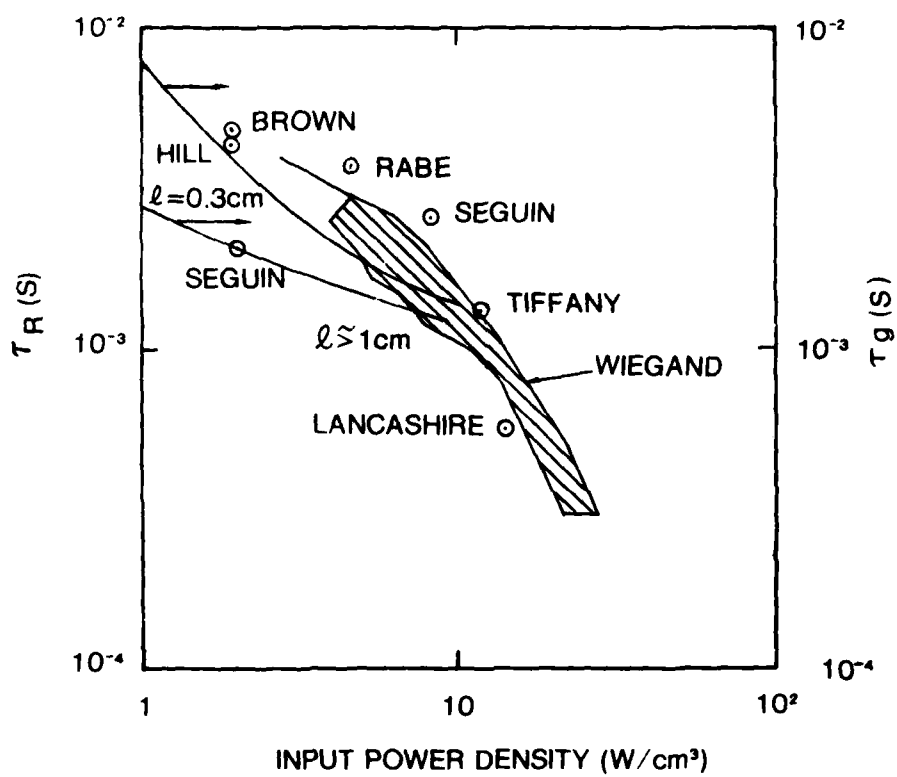
Figure 3.   Closed-cycle cw CO_2 laser gas residence time vs. input power density.

The instability growth times (τ_g) shown in Fig. 3 were computed by Nighan and Wiegand[17] for a pressure of 20 Torr and a gas temperature of 300°K in a recombination-dominated plasma. The parameter ℓ is the scale size of a local disturbance in the plasma properties. The correlation of instability growth times with gas residence times which is apparent in Fig. 3 suggests that convective flow serves to remove local regions of instability from the discharge volume before they can develop into arcs.

The next category of closed-cycle lasers is the pulsed CO_2 laser. An overview of the performance data reported for these lasers is given in Table 2, where once again the listing is chronological. All of the authors utilized transverse discharges, and all except Beaulieu employed some type of preionization: Beaulieu[18] used an individually ballasted multi-pin cathode and a rod anode; Dumanchin, et al.,[19] used a parallel-blade cathode with dielectric-covered trigger wires between blades and a planar anode; Glanford, et al.,[20] used Rogowski electrodes with trigger-wire preionization; Dzakowic and Wutzke[21] used Bruce-profiled electrodes with corona initiators offset to either side for preionization; Tulip, et al.,[22] used profiled electrodes with downstream spark gaps to provide switching and UV for pre-ionization; in the present investigation Rogowski electrodes with trigger-wire preionization were used; and Laughman, et al.,[23] used Rogowski elec-trodes with downstream spark gaps for UV preionization.

In contrast to the cw CO_2 lasers of Table 1, the pulsed CO_2 lasers 1) are smaller--discharge volumes of tens to hundreds of cm^3 vs multiliter volumes, 2) operate at much higher pressure--hundreds of Torr vs tens of Torr, 3) have much shorter gas residence times--tenths of ms vs ms, and 4) have much higher power loading--50 - 140 W/cm^3 vs 2 - 14 W/cm^3. Although the pulsed lasers generate less average power, they provide peak powers up to the milliwatt level.

12

Table 2

CLOSED-CYCLE PULSED CO_2 LASERS

REFERENCE	PRF (kHz)	ENERGY/ PULSE (J)	AVG. OUTPUT POWER (W)	(W/cm^3)	EFF. (%)	PRESSURE	FLOW (m/s)	DISCHARGE DIMENSIONS (cm)
Beaulieu (1971)	1.2	0.5	600			1 atm		150
Dumanchin, et al. (1972)	0.1	20	2000	0.2		1 atm	50	10 × 10 × 100
Glanford, et al. (1973)	1	0.32	320	6.4	4.5	1 atm	50	1 × 1 × 50
Dzakowic and Wutzke (1973)	0.6	0.33	200	3.7	6	510 Torr	41.5	1.1 × 1.5 × 33
Tulip, et al. (1976)	2	1			5	1 atm	100	2.5 × 2.5 × 60
Olson, et al. (1977)	2	0.035	70	5.6	3.9	500 Torr	49	1 × 0.5 × 25
Laughman, et al. (1978)	1	0.86	860	4.3	8.2	250 Torr	47	2 × 4 × 25

13

The results of Laughman, et al.,[23] are the best that have been reported
to date. Under conditions of reduced flow (19 m/s) and reduced power loading
(9.2 J at 100 Hz), they achieved an average laser output of 58 W over a
period of 7 hr with no decrease in output power. This excellent performance
can be attributed in part to the construction of the laser from vacuum-
compatible materials and the use of a relatively contaminant-free blower
driven externally through a magnetic coupling.

Although closed-cycle operation of fast-flow lasers is desirable, there is
a disadvantage in that the concentration of plasma-generated species can build
up to the point where laser gain and eventually discharge stability are
affected. In the case of the CO_2 laser, electron-impact dissociation of CO_2
produces large amounts of CO and O_2:

$$e + CO_2 \rightarrow CO + O + e \tag{4}$$

The CO is not a problem since it is only slightly less effective than N_2
in populating the upper laser level of CO_2. The oxygen, however, promotes
the formation of negative ions which cause discharge instabilities. The
presence of negative ions in low-pressure CO_2 discharges was recently
verified by Prince and Garscadden[24] using an on-line quadrupole mass
spectrometer. Their results showed that NO_2^- is the dominant ion in
a typical low-pressure CO_2 laser mixture.

Shields, et al.,[25] have studied TEA-laser discharges for both low- and
high-pressure conditions. They modeled the plasma chemistry of the TEA
laser,selecting from over 60 relevant reactions and using 13 rate equations.
Simulating the low-pressure conditions of Prince and Garscadden's negative-
ion measurements, they established satisfactory correlation of their model
with the low-pressure experimental data (normalizing their results to the

14

O^- peak). For the high-pressure case, they found CO_3^- and CO_4^- to be the dominant negative ions. When the reaction products were allowed to accumulate in the laser (as under closed-cycle operation), the dominant ion became CO_4^- as a result of the buildup of oxygen from the dissociation of CO_2. The concentration of CO_4^- increased as the oxygen concentration was increased, with the result that the negative-ion concentration doubled for an addition of ~ 2% oxygen. Shields showed that the addition of CO reduces the CO_2 dissociation and thereby the oxygen which is responsible for generating the negative ions. It is interesting that Shields found the nitrogen oxides to be unimportant at high pressure, measuring less than 25 - 75 ppm of the various oxides in his discharges.

It should be emphasized that the work of Shields, et al., is only one example of modeling. They assumed a constant E/N of 2×10^{16} V cm^2 and excitation by a 300-ns square pulse of electrons at 10^{13} cm^{-3} and 1 eV for their modeling. Under somewhat different conditions—microsecond pulse lengths at high-energy loading (755 J/ℓ atm)—the plasma-chemistry model of Thoenes, et al.,[26] for repetitively pulsed, closed-cycle electric discharges at atmospheric pressure has shown that the presence of hydrogen (H_2 or H_2O) in CO_2:N_2:He or CO_2:CO:N_2 laser gas mixtures leads to the formation of the highly electrophilic species HNO_2 and HNO_3. With these species present, steady-state energy loading stabilizes at 27 J/ℓ atm, whereas elimination of these species results in steady-state loading at nearly the initial loading of 755 J/ℓ atm.

The results of these theoretical models must be regarded with caution since the ionization and attachment coefficients as a function of E/N have yet to be determined for specific gas mixtures.

While the conditions in sealed TEA lasers have been analyzed to some extent, the plasma chemistry in e-beam sustainer lasers is less well known. The plasma chemistry of atmospheric-pressure e-beam discharges has recently been studied by Bletzinger and DeJoseph.[27] They used a closed-cycle UHV fast-flow loop similar to that of Ref. 1 and a 5×15 cm cross-section e-beam capable of producing total currents to 10 mA at up to 200 keV energy. The UHV loop, having base pressure in the 10^{-9} Torr range, provided a clean reaction vessel with minimal contamination by leaks and outgassing. They diagnosed the reaction products of e-beam-irradiated atmospheric-pressure mixtures of CO_2, N_2, and He. The identity and concentration of infrared active species were determined off-line via infrared absorption spectroscopy, with gas samples in a 20-m White cell analyzed by a high-resolution (0.07 cm^{-1}) interferometer-spectrometer. On-line monitoring of selected species was performed using a diode laser tuned to known absorption lines of the gases of interest. They demonstrated the plasma-chemical production of nitrogen oxides in atmospheric-pressure e-beam discharges and a large increase in the generation of dissociation products caused by the addition of O_2. These results show the need to use high-purity vacuum systems for long-term closed-cycle operation of atmospheric-pressure CO_2 lasers.

The third category of closed-cycle lasers to be discussed is the pulsed Xe laser. Results obtained for He-Xe and Ar-Xe lasers are presented in Table 3. The He-Xe laser is important in reconnaissance and countermeasure applications as a result of its simultaneous oscillation at various wavelengths in atmospheric transmission windows in the $2 - 5$ μ range. Moderate power (watts) and high repetition rates (kHz) are required for these applications. Fahlen and Targ[28] have achieved the highest average power (11 W) to date; the highest repetition rate to date (12 kHz) has been achieved in the present investigation. The Ar-Xe

16

Table 3

CLOSED-CYCLE PULSED Xe LASERS

GAS	REFERENCE	λ (μ)	PRF (kHz)	ENERGY/PULSE (mJ)	AVG. OUTPUT POWER (W)	(W/cm³)	EFF. (%)	PRESSURE (Torr)	FLOW (m/s)	DISCHARGE DIMENSION (cm)
He-Xe	Fahlen and Targ (1973)	2.03, •2.65, 3.43, 3.65	1.2 (2 kHz at reduced voltage)	9	11 (90 kW [peak])	0.01	0.13	He:400 Xe:1	40 (6000 cfm)	4.75 × 3 × 76
He-Xe	Olson, et al. (1977)	2.03, 2.65, 3.65	6	0.28	1.68	0.034	0.08	He:400 Xe:4	49 (370 cfm)	1 × 2 × 25
Ar-Xe	Olson, et al. (1977)	1.73 2.65, 2.03 3.1, 2.48 3.37, 2.63 5.57	8.65	0.26	2.27	0.045	0.86	Ar:400 Xe:2	49 (370 cfm)	1 × 2 × 25
He-Xe	Olson, et al. (1979)	2.03, 2.65, 3.65	9.5	0.43	4.1	0.082	0.12	He:1200 Xe:12	60	1 × 2 × 25
He-Xe	Fahlen (1979)	2.03, 2.65, 3.43, 3.65, (3.87)	7	1.14	8 Double-Pass Osc.	~ 0.08	0.13 (Total)	He:600 Xe:1	100 (Design)	2 × ~ 1 × 50

results are significant because of the good efficiency achieved (near 1%); however, most of the output is at 1.73 µ which is outside the range required for the above applications.

The 1977 He-Xe and Ar-Xe laser data were obtained using the recirculating-loop configuration.[1] The 1979 He-Xe laser data were obtained using a novel, compact closed-cycle configuration employing an annular-flow return surrounding the discharge channel. The size of this laser was considerably reduced over that required for an open-loop configuration, making it more suitable for airborne applications. This laser is discussed in detail in Section 4. When an output mirror of higher reflectance was used with the compact He-Xe laser, simultaneous lasing was observed at 2.03, 2.65, 3.04, 3.43, 3.65, 3.87, 4.02, 5.13, and 5.44 µ. The 5.13- and 5.44-µ lines have not been reported in the literature but have been observed by W. Schuebel (AFWAL Avionics Laboratory) in a static discharge.

Fahlen's 1979 results[29] were obtained for a compact closed-cycle configuration utilizing a stainless-steel vacuum enclosure and blowers externally driven through ferrofluidic seals. The laser was designed to satisfy requirements for airborne applications--compact, lightweight, and capable of long-term operation.

The 1977 He-Xe data from the present investigation reflect conditions under which maximum power was generated by the laser. Lower-voltage operation would have been more efficient but at a sacrifice of laser output power. This is also true of the 1979 data which were obtained at a charging voltage of 12 kV; operation at a pressure of 600 Torr and a charging voltage of 4 kV yielded an efficiency of 0.22%.

The lifetime of closed-cycle He-Xe lasers has proved to be excellent. The compact annular-return laser was operated continuously for 8 hr. at 5 kHz (1.4×10^8 pulses) under sealed-off conditions with no addition of make-up gas. During this time there was no degradation of the 1-W laser output power. Fahlen's compact He-Xe laser was operated continuously for 4 hr. at 6 kHz, during which time the 5.5-W laser output decreased by about 4%. The excellent lifetime performance of the closed-cycle He-Xe laser can be attributed to the ultrahigh-vacuum nature of the laser construction which ensures minimum contamination of the laser medium. The lifetime of the closed-cycle Ar-Xe laser is not so impressive as that of the He-Xe laser, exhibiting a 30% decrease from a 1-W output during 4 hr. of operation. The greater fall-off in output power for the Ar-Xe laser may be due to the greater sputtering rate of Ar, as compared to He, which could result in the rapid evolution of impurity gases or Xe gas cleanup at the Al cathode.

The model developed by Dzakowic and Wutzke[21] for predicting the stability of pulsed transverse discharges with fast transverse flow predicts a boundary-layer-diffusion-dominated clearing ratio (minimum time between arc-free pulses/gas transit time through gap) of $\sqrt{3}$ at low energy inputs. In our work with He-Xe and Ar-Xe, however, clearing ratios of less than one were observed. This corresponds to the overlapping of discharge pulses in the interelectrode gap which has been observed visually through the dependence of discharge width upon repetition rate. The discharge tends to concentrate in the spatial-overlap region of successive pulses due to the preionization provided by previous-pulse residual ionization. The laser-beam-intensity profile is probably

affected by the nonuniform discharge intensity which results from over-lapping discharge pulses. This has not yet been confirmed by beam-profile measurements.

The role played by Ar and He buffer gases in achieving population inversion in Xe has been analyzed in several recent publications. Shuker, et al.,[30] have proposed for He-Xe mixtures that the upper laser levels are populated by radiative cascade from highly excited Xe atoms formed by recombination of Xe ions generated by Penning ionization reactions with metastable He atoms and molecules. A recombination-cascade pumping mechanism has also been suggested by Silfvast, et al.,[31] to explain the population inversion in laser-produced He-Xe plasma lasers. Another likely pumping mechanism for He-Xe is the dissociative recombination of Xe_2^+. It appears from the results of Shiu, et al.,[32] that dissociative recombination can produce any Xe* state which is lower in energy than the initial $(Xe_2^+ + e)$ state.

Population inversion in Ar-Xe mixtures appears to be a more complex process. Gedanken, et al.,[33] have shown that there is efficient molecule-atom energy transfer to Xe* levels which overlap the Ar_2* second molecular continuum. However, in a recent study of the high-pressure Ar-Xe laser by Lawton, et al.,[34] transfer from Ar_2* was shown to be of minor impor-tance. Their kinetic model identifies electron-impact excitation from lower-lying Xe* states, dissociative recombination pumping, and recombination-cascade pumping as the most plausible population inversion mechanisms in Ar-Xe mixtures. The relative importance of each process was not determined by Lawton, et al., due to a lack of data for excited-state cross sections, recombination and quenching rates, and branching

ratios. They ascribe the effectiveness of Ar as a buffer gas in an Ar-Xe e-beam ionizer-sustainer discharge laser to the high e-beam stopping power of Ar, the lower electron mobility in Ar which improves the impedance match to the external sustainer circuit, and the low electron-scattering cross section in Ar which ensures efficient sustainer power transfer to excited species.

The above discussion of pumping mechanisms leads to the conclusion that efficient laser action in high-pressure He-Xe and Ar-Xe mixtures requires a rapidly recombining dense-plasma gain medium such as the afterglow of a pulsed transverse discharge. A high-power pulse with a steep trailing edge is needed to generate the high ion density and rapid electron cooling required for inversion.[35] Rapid depopulation of the lower laser level by, for example, de-exciting collisions with cold electrons or heavy particles is also necessary. In the Ar-Xe laser, electron-impact excitation of Xe metastables appears to be an important pumping mechanism which could lead to higher laser efficiency through a recycling of the energy stored in the metastables.[34]

The fourth and last category of closed-cycle lasers includes XeF, KrF, and XeCl lasers as shown in Table 4. Christensen's laser[36] is better described as a recycled rather than closed-cycle laser since the longitudinal flow through the laser is discharged into a dump tank and later processed via cold traps in order to reclaim Xe and NF_3 which are then recycled through the laser along with fresh gas which has been added. Christensen achieved many recyclings without cumulative contamination. On-line processing proved to be unsuccessful due to inefficient cold trapping at high flow rates. A thyratron-switched Blumlein circuit was used for excitation.

Table 4

CLOSED-CYCLE PULSED RARE-GAS-HALIDE LASERS

GAS	REFERENCE	λ (nm)	PRF (kHz)	ENERGY/PULSE (mJ)	AVG. OUTPUT POWER	EFF. (%)	PRESSURE (Torr)	FLOW	DISCHARGE DIMENSIONS (cm)
He:Xe:NF$_3$ 100:3:1	Christensen (1977)	351	0.2	0.26	52 mW		720	6.8 ℓ atm/ min.	0.1 × 1 × 50
He:Kr:F$_2$ 680:30:5	Fahlen (1978)	248	1	10	10 W	0.13	715	70 m/s	2 × ? × 70
He:Kr:F$_2$	Fahlen (1978)	248	1	48	48 W		1300		
He:Xe:HCl 1230:70:3.5	Miller, et al. (1979)	308	0.6	75	45 W		1400	20 m/s	2 × ? × 60
	LASL (PROPOSED)	248	1	1000	1 W	(10-min. runs at 1 kHz)			

Fahlen's laser is truly closed cycle and has yielded the highest rep

rate (1 kHz) and highest average power (48 W) to date for KrF.[5]

The rep-rate dependence of average output power from Fahlen's laser revealed

a decrease in pulse energy with rep rate which may be due to discharge

instabilities induced by heating of the gas or electrodes or by decomposi-

tion or contamination of the initial gas fill. Fahlen reported[37] a rep-

rate-dependent falloff in pulse energy of 10% in 17 min. at 30 Hz and 10%

in 1 sec at 1 kHz. The pulse energy recovers fully after the discharge

is turned off for a few minutes.

Recently, Miller, et al.,[38] investigated the performance of a high-

repetition-rate, closed-cycle, UV-preionized rare-gas-halide laser of

high-purity construction. The characteristics of the laser operating

with ArF, KrF, XeF, and XeCl were obtained. The best performance was

demonstrated by the XeCl laser, as shown in Table 4. With XeCl, they

were able to maintain an average power of greater than 35 W for over

1 hr at a repetition rate of 500 Hz. The lifetime was limited by

coating of the laser windows rather than gas degradation.

Also shown in Table 4 are the truly ambitious performance specifica-

tions desired by Los Alamos for a proposed high-rep-rate closed-cycle KrF

laser. The stringent switch and capacitor requirements for such a laser

are given on the following page.

SWITCH REQUIREMENTS

Voltage Holdoff	50 kV
Peak Current	50 kA
Current Pulse Width	< 100 ns
Repetition Rate	1 kHz
Lifetime	5×10^8 MTBF
Jitter	< 10 ns
di/dt	> 2×10^{12} A/s
Inductance	< 10 nH

CAPACITOR REQUIREMENTS

Energy Storage	50 – 100 J
Charging Voltage	50 – 100 kV
Inductance	< 10 nH
ESR	< 0.05 Ω
MTBF	> 10^8 Shots
PRF	1 kHz

Considering the present state-of-the-art, the switch requirements can probably be met only by using a parallel array of thyratrons. The requirements for capacitors having high-voltage standoff, low inductance, and long lifetime at high rep rate can probably best be met by a large array of coaxial cables.

Beyond the stringent circuit-component requirements, there are severe materials problems associated with rare-gas-fluoride lasers as a result of the extreme reactivity of the laser medium. The magnitude of the problem is pointed up by Tennant's results[39] on the reaction of fluorine with various materials in a static, well-passivated test cell, which

24

showed that fluorine reacts quite well with most dielectrics commonly used in the fabrication of lasers. Tennant measured reaction products using a TOF mass spectrometer and added the major contaminants, thus identified, to a KrF laser. The results showed that every contaminant reduced the laser output energy. Particularly striking was the fact that the addition of 0.6 Torr of CO_2 to the 1400-Torr laser gas mixture reduced the laser output to zero. Clearly, the high-rep-rate closed-cycle rare-gas-halide laser has significant problems yet to be solved.

In conclusion:

1. Closed-cycle operation is necessary for practical fast-flow high-pressure lasers.

2. The parameter of merit for closed-cycle lasers is lifetime.

3. There is a need to scale the kinetics modeling for these lasers to higher pressure.

4. There is a need for experimental studies and validation of theoretical models of the chemistry of high-rep-rate lasers operating in the closed-cycle mode under conditions of high pressure and fast flow.

SECTION III

RECIRCULATING-LOOP LASER

3.1 VELOCITY PROFILE

The importance of establishing a uniform velocity profile in the discharge region of a flowing gas laser has been discussed by Eckbreth and Owen.[10] Nonuniform flow results in nonuniform energy deposition with consequent temperature nonuniformities which promote arcing. The velocity profile in the discharge region of the recirculating-loop laser[40] was measured by translating a 1/16-in.-o.d. Pitot-static probe along the 28-cm length of the Rogowski electrodes at the midplane of the electrode gap. The flow geometry is shown at the top of Fig. 4, with velocity profiles shown below. Profiles were obtained for each of two fans--one being equipped with stator vanes and the other without vanes. Stator vanes, which transform the kinetic energy of whirl into pressure head, were added to the axial fan assembly, as shown in Fig. 5, in order to increase the flow velocity and uniformity. The addition of stator vanes increased the maximum velocity by only 6%. More importantly, however, the variation of the velocity profile was improved. Over the central 25 cm of the electrodes (where the discharge is established), the velocity at the electrode ends decreased ~ 7% from the maximum for the fan without vanes and ~ 5% for the fan with vanes. The results of Ref. 10 indicate that velocity profiles uniform to within 4% are desirable for discharges aligned with the flow.

Prior to these velocity-profile measurements, the flow velocity in the interelectrode gap (V_2) had been obtained from the measured flow velocity in the 6-in.-o.d. pipe (V_1) and the cross-sectional areas of the 6-in. pipe (A_1) and the interelectrode region (A_2) using $V_2 = (A_1/A_2)V_1$. This yielded

FLOW GEOMETRY (TOP VIEW)

ROGOWSKI ELECTRODES

PITOT-STATIC PROBE

GLASS WALL

FLOW

WITH STATOR VANES

WITHOUT STATOR VANES

160

120

80

40

0

POSITION (cm)
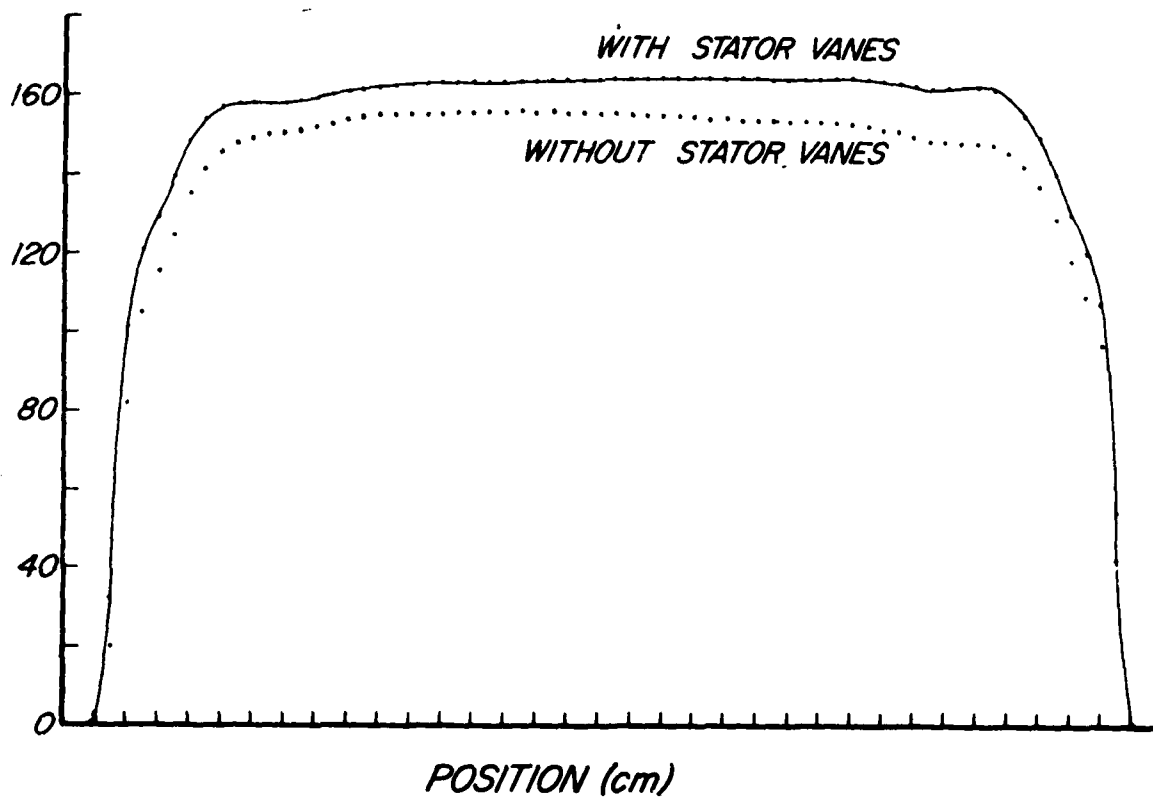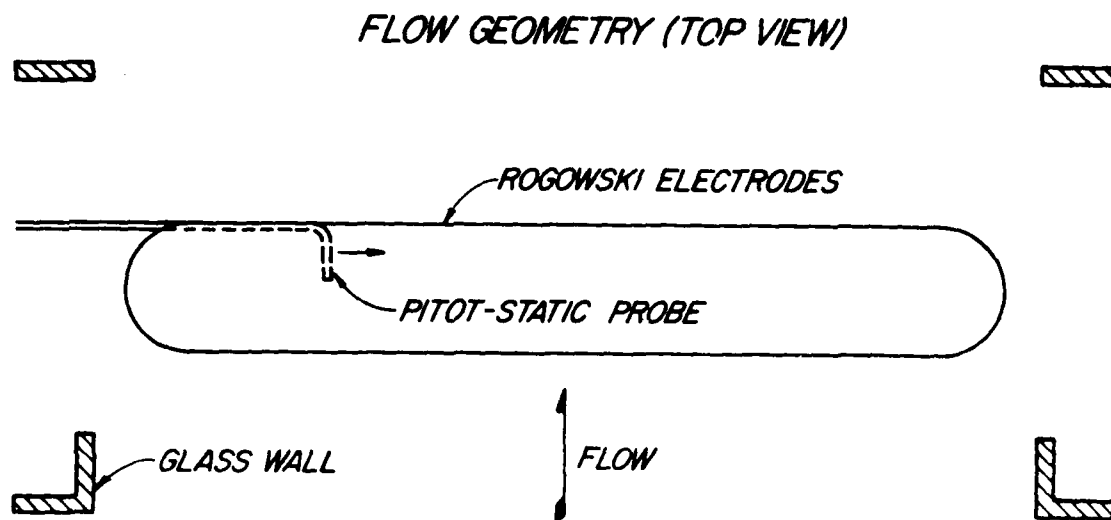
Figure 4.   Velocity profiles for 25-cm-gain-length laser.
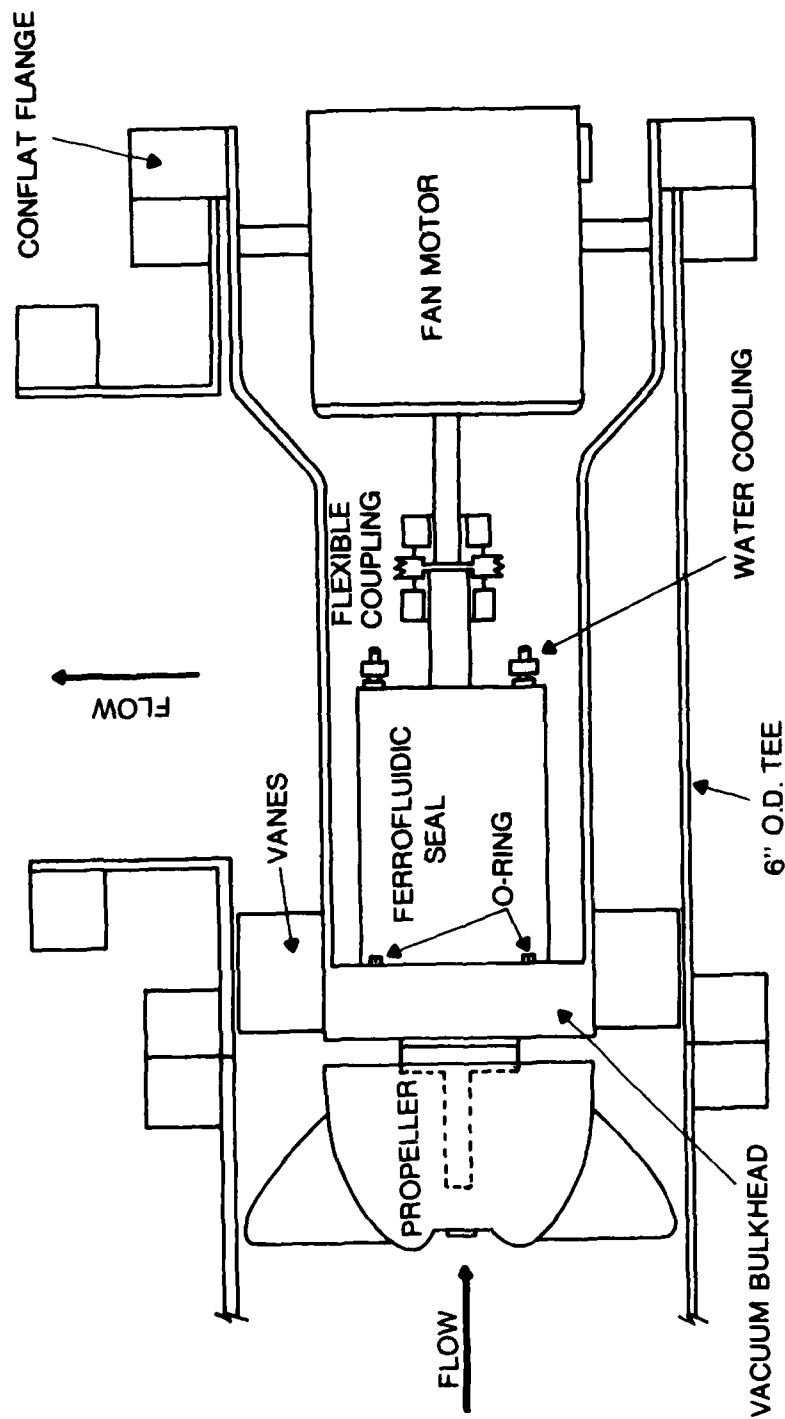
Figure 5. Vaneaxial fan assembly.

CONFLAT FLANGE

FAN MOTOR

FLEXIBLE COUPLING

FLOW

WATER COOLING

VANES

FERROFLUIDIC SEAL

O-RING

6" O.D. TEE

PROPELLER

FLOW

VACUUM BULKHEAD

a velocity of 180 ft/sec compared with the present value of 156 ft/sec.
The difference in these values may be due to the fact that the fixed probe
was located on the axis of the 6-in. pipe, and measurements were made,
therefore, at the peak of the velocity distribution across the pipe.

3.2 PULSER-CIRCUIT INDUCTANCE

Fast-rising short-duration pulses are beneficial in achieving uniform
high-pressure glow discharges and rapid heating of electrons to high energy.
The limiting factor in achieving fast risetime is circuit inductance. In
the lumped-parameter circuit of the high-repetition-rate pulser used for
the recirculating-loop laser, most of the inductance is associated with the
HY-5 thyratron and the energy-storage capacitor. In order to measure the
inductance of the pulser, the output was short circuited and the ringing
frequency of the resulting damped oscillation was observed. The instan-
taneous current is given by

$$i(t) = \frac{V_o}{\omega L} e^{-Rt/2L} \sin \omega t \qquad (5)$$

where V_o is the charging voltage, L the inductance, R the internal resis-
tance of the pulser, t the time, and $\omega = \sqrt{1/LC - R^2/4L^2}$. The inductance
can be calculated from the expression for the ringing frequency, which for
small R is given by

$$f = \frac{1}{2\pi} \sqrt{\frac{1}{LC}} \quad . \qquad (6)$$

29

Unambiguous measurements of the ringing frequency were impossible since little inverse current is conducted by the thyratron, which is a unidirectional switch. In fact, the inverse voltage aids in extinguishing the thyratron discharge. An estimate of the oscillation period made from the primary current-pulse width was used to calculate an inductance of 410 nH. It was suspected that the thyratron contributed most of this inductance; therefore, the HY-5 was replaced by an 8354 thyratron in a tightly coupled coaxial configuration. Shorter pulses of higher current were then obtained. A calculation of the circuit inductance (as above) yielded a value of 250 nH. A comparison of the pulses obtained with the different thyratrons for a 2-nF capacitor charged to 5 kV is shown in Fig. 6.
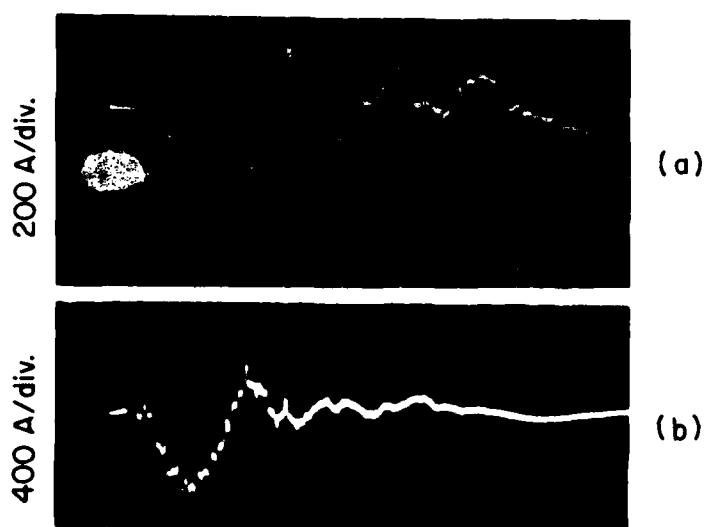
Figure 6. Short-circuit output current of high-repetition-rate pulser using (a) HY-5 and (b) 8354 thyratrons.

Approximately the same value of inductance was obtained for short-circuit pulses from 1-, 2-, and 5-nF capacitors switched by the 8354. This indicates that the thyratron is the main source of inductance in the pulser circuit.

3.3 INDEPENDENT PREIONIZATION

The use of capacitively coupled trigger wires to provide preionization for He-Xe discharges has proved to be adequate, although at low repetition rate (< 1 kHz) the discharge tends to become filamentary and the laser output sharply decreases. The effectiveness of trigger wires in Ar-Xe discharges has been less satisfactory, with pressure being limited to below 400 Torr and discharge voltage limited to ~ 8 kV. It has been demonstrated for TEA discharges in CO_2 laser mixtures and rare-gas fluorides that there is an optimum delay between preionization and application of the main discharge voltage.[41,42] In an attempt to improve the effectiveness of the trigger-wire technique, the high-repetition-rate pulser was modified by the addition of a variable delay (0.1 to 1000 μs) in the main discharge pulse and an independent preionization pulser, as shown in Fig. 7.

The circuit of Fig. 7 was evaluated for discharges in 700 Torr of He. It was found that for short delay times (< 5 μsec), the main discharge was not established between the Rogowski electrodes but instead followed a path from cathode to wires to anode. A uniform discharge could be established for delay times of ~250 μsec. As the delay was increased beyond 250 μsec, a "hollow" developed in the center of the discharge. A glow discharge could not be achieved in Ar (300 Torr).
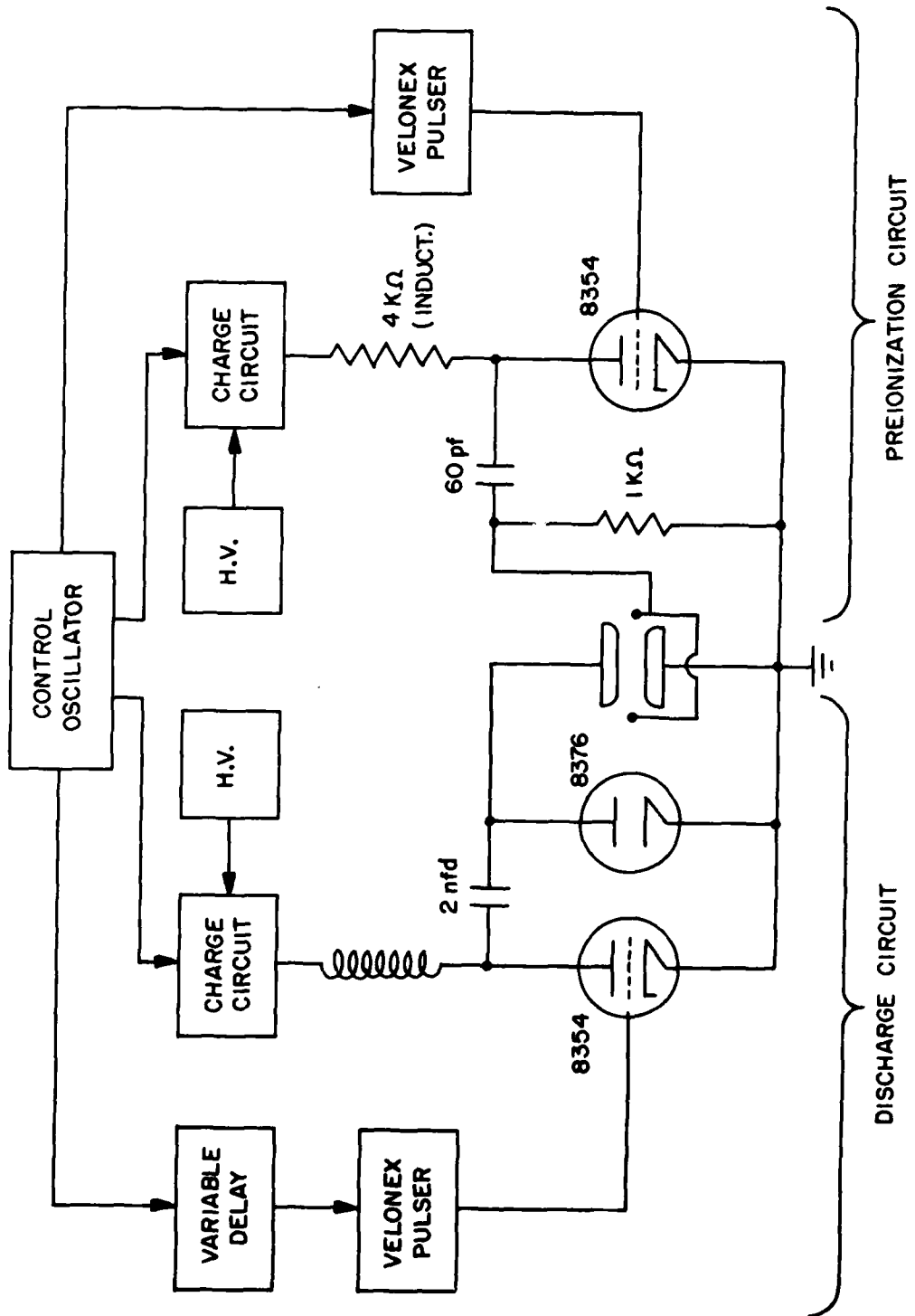
Figure 7. Block diagram of high-rep-rate pulser with independent preionization circuit.

In order to decouple the preionization circuit from the main discharge circuit (to avoid discharges from cathode to wires), the preionization wires were lowered from the electrode midplane to the plane of the anode. According to W. Schuebel (AFWAL Avionics Lab), this is the optimum position for the wires as determined by tests using a static discharge. Unfortunately, this geometry was found to be impractical when used with transverse gas flow. Under flowing gas conditions, standing waves were induced in the downstream preionization wire. The standing waves experienced a rotation about the axis of the wire which resulted in periodic shorting of the wire to the anode.

3.4 OPTICAL SWITCH EVALUATION

The independent-preionization study was terminated and the capacitive-coupling configuration reinstalled in order to make the laser operational as an IR source for evaluating the characteristics of an optical switch. It was necessary to use a 5-nF capacitor switched by an HY-5 thyratron since the 2-nF capacitor had been damaged by overheating during operation with an uncooled 8354 thyratron at 10 kHz. A new 2-m reflector and a Si partial transmitter were used for the optical cavity.

Previously,[40] the maximum laser output power had occurred at 400-Torr He-Xe (100:1). Using this gas fill in the present setup, the data of Fig. 8 were obtained, Fig. 8(a) showing the dependence of average laser output power upon PRF and Fig. 8(b) the dependence of output power and efficiency upon input power (i.e., the average output power of the energy-storage capacitor). The 1.68-W output at 6 kHz was the highest power achieved to date for He-Xe in the recirculating-loop laser. More importantly, the efficiency was much higher than the 0.03% achieved previously.

33
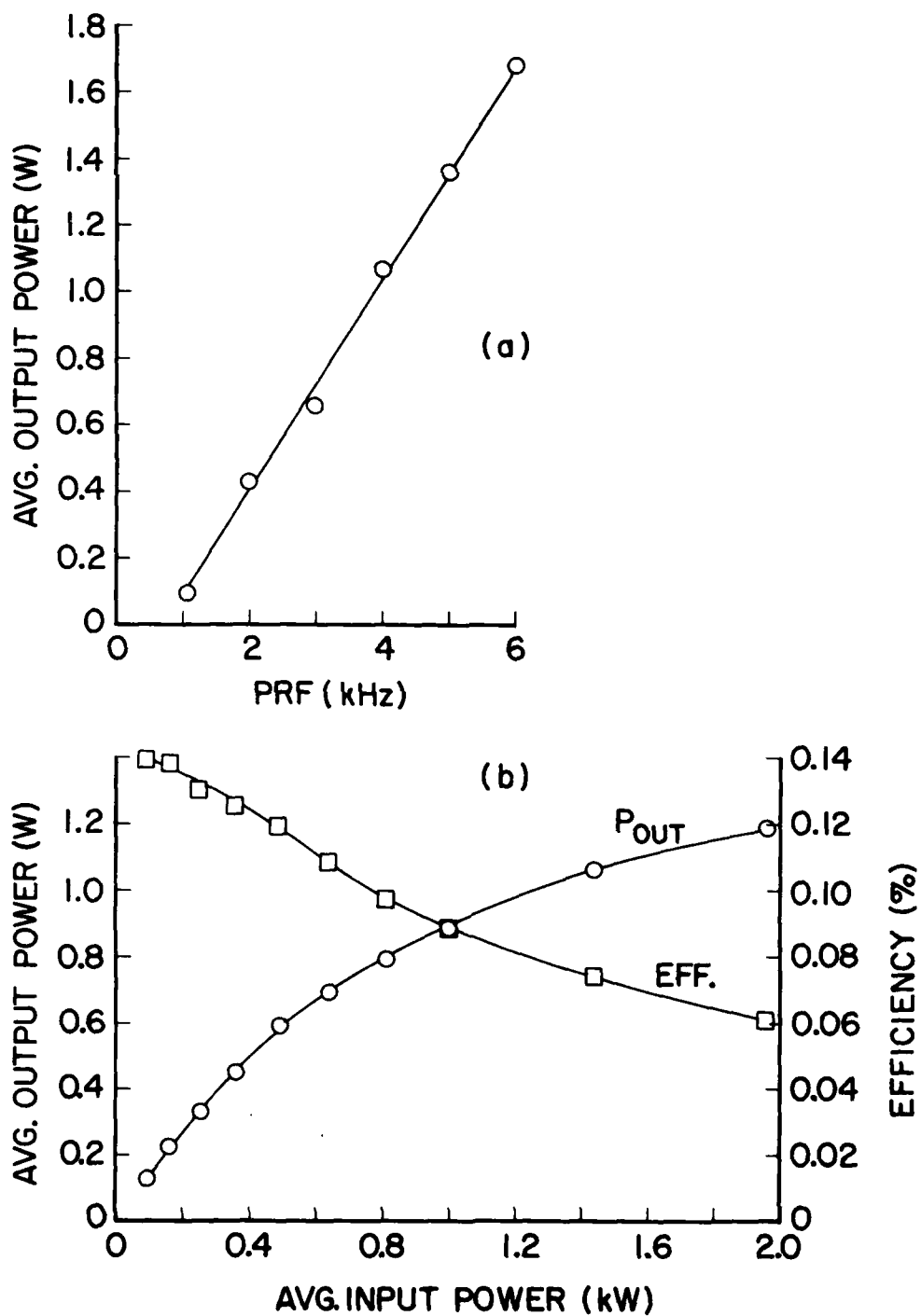
Figure 8. (a) Dependence of average laser output power upon PRF for 400-Torr
He-Xe (100:1) at 12-kV charging voltage, (b) dependence of average
laser output power and efficiency upon average input power for
400-Torr He-Xe (100:1) at a PRF of 4 kHz.

34

The increased efficiency was probably due to a more effective power loading with the 5-nF than with the 2-nF capacitor. The continuous decrease in efficiency with increasing input power may be due to the worsening impedance mismatch between pulser and discharge with increasing input power, which results in less-effective power loading into the discharge.

Evaluation of the optical switch was performed in cooperation with F. Nichols of AFWAL/Avionics Lab and R. Hemphill of Vought Corp. The optical transmittance of the switching material undergoes a rapid change from ~50% to ~0% T in the vicinity of 65°C. The material had been successfully switched (at Vought) by a 500-μJ, 1-μsec pulse from a visible dye laser focused to a 600-μ spot. Dynamic switching could not be achieved with the recirculating-loop He-Xe laser; however, when the substrate temperature was increased to ~60°C, the entire laser pulse was attenuated, presumably due to the average laser-heating effect. The laser beam was focused with a 1-in.-diam. CaF_2 lens to a 0.0075-in. × 0.0025-in. spot on the switching material. Operation at 4 kHz and an average laser output power of 0.95 W yielded 237-μJ pulses which provided a spot intensity of ~ 1 J/cm^2. Although this was approximately five times the intensity at which switching had been observed with the visible laser, it was insufficient to induce switching, probably because the absorption of IR by the material is much less than for visible.

3.5 AFTERGLOW ELECTRON-DENSITY DECAY MEASUREMENTS

The capability of the recirculating-loop laser to operate at rep rates higher than the inverse of the flow transit time has not yet been explained. This mode of operation is important not only because high rep rate is achieved but also because the laser output is enhanced under this condition.

A similar effect observed for CO_2 waveguide lasers[43] has been ascribed to the preionization provided by interpulse residual ionization.

The level of interpulse residual ionization is given by the electron density in a recombination-controlled afterglow plasma

$$\frac{1}{n} = \frac{1}{n_o} + \alpha t \tag{7}$$

where n is the electron density at time t after the discharge pulse, n_o is the initial electron density, and α is the recombination coefficient. For the conditions existing in the closed-cycle laser, dissociative recombination is the dominant recombination mechanism represented by

$$X_2^+ + e \rightarrow (X_2)^* \rightarrow X^* + X + K.E. \tag{8}$$
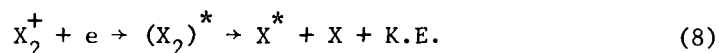
The form of Eq. (7) suggests plotting data from recombination measurements as 1/n vs t. This is done in Fig. 9 for measurements in 300-Torr He and 300-Torr He-Xe (100:1) at a charging voltage of 5 kV and a rep rate of 285 Hz. Following each discharge pulse a square pulse of 250 V was applied to the discharge electrodes through a blocking triode. The electron density was obtained from current-vs-time oscillograms using

$$j = nev_d \tag{9}$$

where j is the current density and v_d is the drift velocity which was obtained from Ref. 44.

36
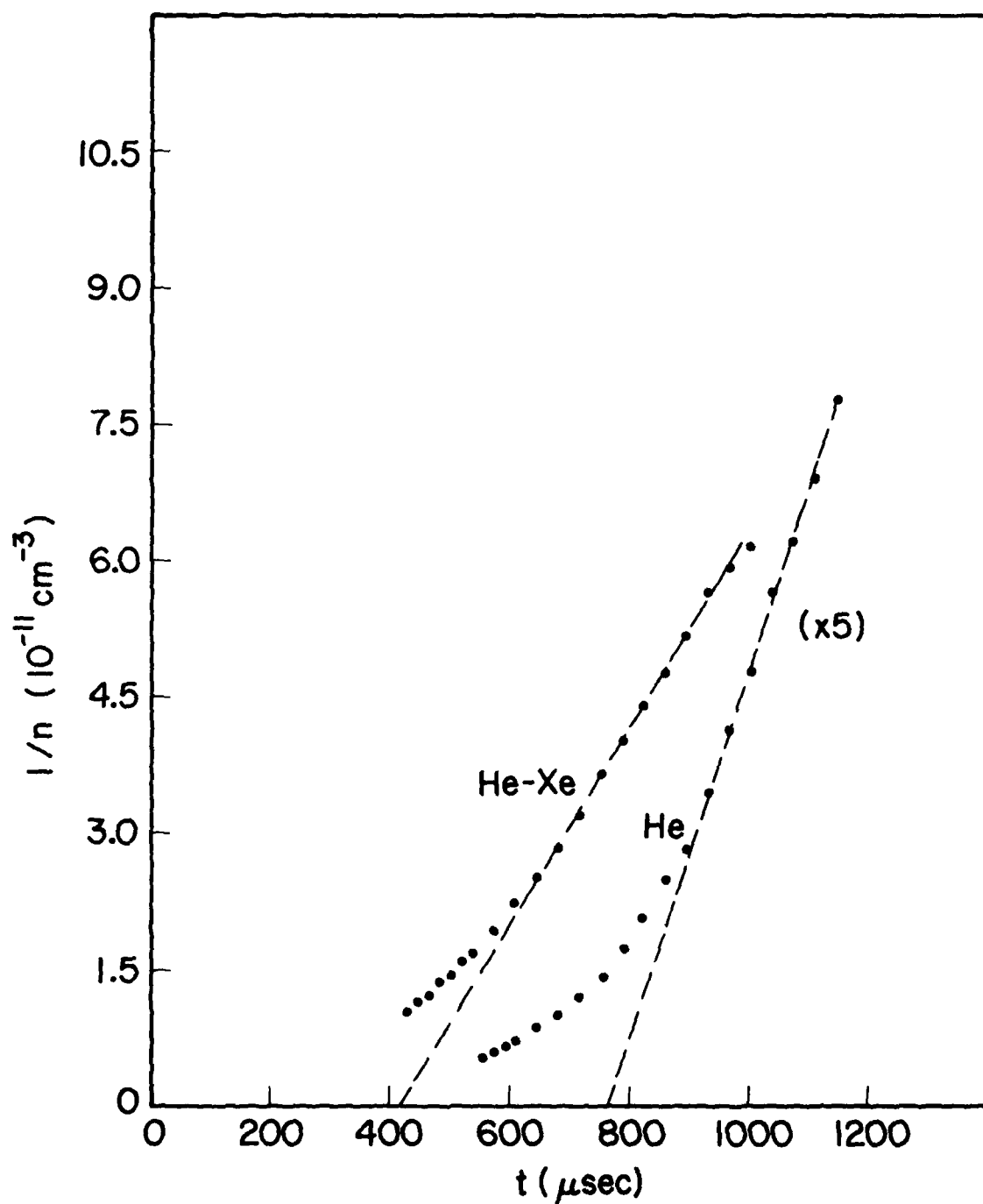
Figure 9. Electron-density decay in the afterglow of He and He-Xe
discharges in the closed-cycle laser.

Recombination coefficients obtained from straight-line slopes in Fig. 9 are 4×10^{-8} cm^3/sec for He and 1.1×10^{-7} cm^3/sec for He-Xe. These are to be compared with published values[45] of the dissociative recombination coefficients for He_2^+ of $< 1 \times 10^{-8}$ cm^3/sec and for Xe_2^+ of 1.4×10^{-6} cm^3/sec. Note that initially the rate of recombination is much slower than that in the straight-line region. This behavior resembles that attributed in Ref. 46 to atomic-ion recombination followed by molecular-ion recombination. It is somewhat surprising that even after 1 msec, the electron density in the He-Xe afterglow is $\sim 1.6 \times 10^{10}$ cm^{-3}. At actual laser operating voltages of 10 kV and above, the residual density may be as high as 10^{11} cm^{-3}. This is a substantial amount of preionization and must influence the discharge above a rep rate of $\sim$ 1 kHz. In fact, there is some evidence of this in the observation that the discharge voltage decreased from 10 to 7 kV as the rep rate was increased from 1 to 4 kHz.

The addition of up to 3 Torr of O_2 to the He-Xe discharge changed the electron-decay curve very little. The same was true for 0.1 Torr of SF_6 which, however, did induce arcing at relatively low voltage. The discharge electrodes were removed from the system after operation in the presence of SF_6, and the electrode surfaces were found to be severely damaged due to arcing.

3.6 HIGH-REPETITION-RATE CO_2 LASER

The performance of the recirculating-loop laser was evaluated for CO_2 laser mixtures. A mixture of 400-Torr He, 50-Torr CO_2, 50-Torr CO, and 1-Torr Xe was used initially. The replacement of N_2 in the conventional laser mix by an equal amount of CO is beneficial for long-time operation

as a result of the discharge-stabilizing effect of electron detachment from O^- by CO and the minimization of the formation of nitrogen oxides.[47] A 5-nF capacitor switched by an HY-5 thyratron was used to load up to 0.9 J into the discharge. A 2-m Si reflector and a 92% R (at 10.6 μ) Ge flat were used for the optical cavity.

Maximum laser output was achieved for PRF's in the neighborhood of 2 kHz. Arcing occurred slightly above 2 kHz, and the average laser output power decreased to zero as the PRF was decreased to 1 kHz. The reason for the cessation of lasing at 1 kHz is probably the low energy-loading density of < 18 J/ℓ. Above 1 kHz, however, the discharge contracted to ~ 0.5 cm in width (as evidenced by laser burn patterns) which quadrupled the energy-loading density.

The long-time performance of the laser is shown in Fig. 10 for a 50-min. run time. The initial output of 70 W decreased within 5 min. as filamentary arcs appeared within the glow discharge. The PRF was decreased from 2.2 to 2 kHz to eliminate arcing, and the laser was operated for an additional 40 min. before arcing recurred. Approximately 6×10^6 laser pulses were generated during the 50-min. operation.

The low gain of the laser was pointed up by varying the cavity out-coupling. When the 92%-R output mirror was replaced by a mirror having 80% R, the average laser output power was ~ 16 W. Lasing could not be achieved with a 65%-R output mirror.

The superiority of the laser mix containing CO over the N_2-bearing mix was demonstrated by the fact that an arc-free discharge could not be established above 1 kHz and that lasing was not observed for a mixture of 400-Torr He, 50-Torr CO_2, and 50-Torr N_2.
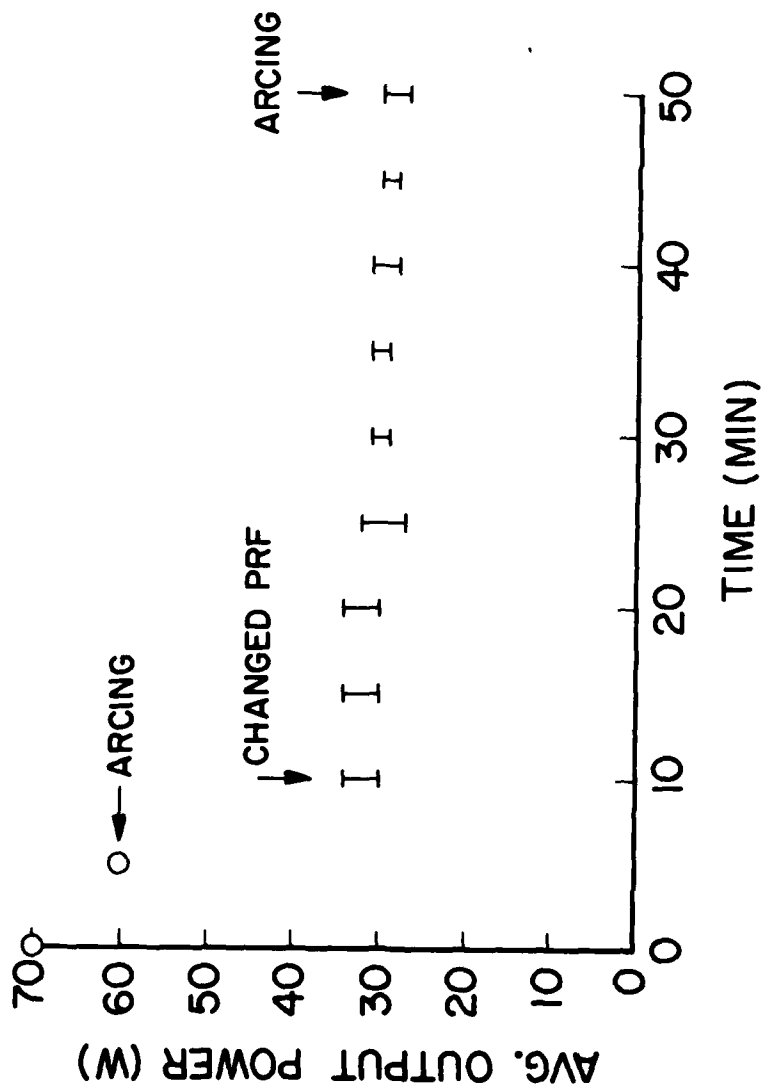
Figure 10. Dependence of average laser output power upon continuous operating time for a 501-Torr mixture of 400 He:50 CO_2:50 CO:1 Xe; C = 5 nF, charging voltage = 19 kV, PRF = 2 kHz.

A parametric evaluation of the CO_2 laser performance was not undertaken because of insufficient energy-loading capability. Neither higher voltage nor a larger capacitor was available.

3.7 LC INVERSION GENERATOR

An LC inversion generator[48] was fabricated and evaluated as a high-rep-rate pulser for the CO_2 closed-cycle laser. A simplified schematic of the pulser is shown in Fig. 11.
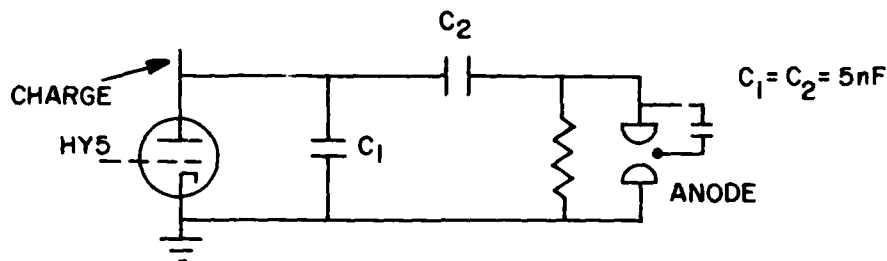
Figure 11. LC inversion generator.

Since C_1 and C_2 are charged in parallel, their opposing polarities result in zero voltage across the discharge electrodes prior to erection. Firing the thyratron induces a ringing of the LC circuit comprised of C_1 and the thyratron inductance and results in a reversal in the polarity of C_1. At the peak of the voltage reversal (one-half cycle later), the voltage across the discharge electrodes--which is also oscillating at the LC ringing frequency--should be twice the charging voltage. In practice, the voltage across the discharge electrodes is limited by breakdown.

Discharge current and voltage oscillograms are shown in Fig. 12(a) for the LC inversion generator and in Fig. 12(b) for the conventional circuit with C_1 omitted. The gas mixture was 400-Torr He, 50-Torr CO_2.

41

CURRENT (1000 A/DIV)

VOLTAGE (5 kV/DIV)

CURRENT (400 A/DIV)

VOLTAGE (10 kV/DIV)
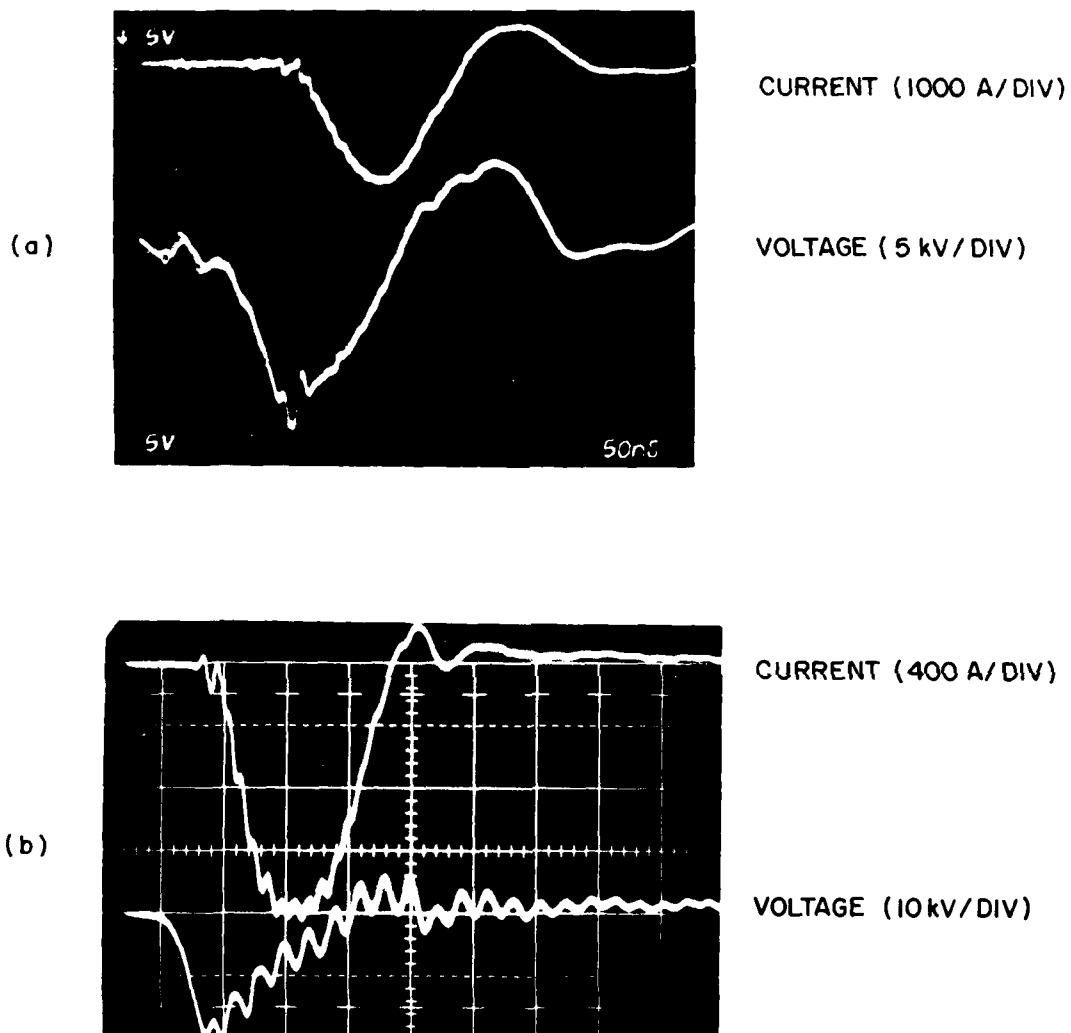
Figure 12. Discharge current and voltage oscillograms for
(a) LC inversion generator and (b) single-
capacitor pulser. Gas mixture: 400-Torr He,
50-Torr CO_2, 50-Torr CO, 1-Torr Xe.

50-Torr CO, and 1-Torr Xe in both cases. The charging voltage was 20 kV for the circuit of 12(a) and 19 kV for 12(b); the rep rate was 100 Hz for 12(a) and 2 kHz for 12(b). Compared with the conventional circuit, the LC generator achieved higher discharge current but less peak voltage, had slower current and voltage risetimes, and had a poorer impedance match. The average laser output power was ~ 20 W at 600 Hz for the LC generator and a maximum of 70 W at 2 kHz for the conventional circuit. Discharge arcing limited the rep rate for the LC generator to values below 700 Hz. The poor performance of the LC generator was probably due to excessive inductance in the LC ringing circuit.

3.8 POKER PULSER

In order to evaluate the poker discharge-excitation technique,[15] the circuit of Fig. 13 was utilized with the recirculating-loop laser. Both pure He and a 1:1:8 CO_2:N_2:He mix were used at pressures from 400 to 700 Torr. Poker capacitance (C_p) values of 0.2 and 1 nF were used. A maximum poker burst rate of 20 kHz and voltage pulses of ~ 14 kV peak with 50-nsec rise and fall time were achieved.

Poker excitation of He produced a visually uniform discharge for sustainer fields of up to ~ 500 V/cm at 400 Torr pressure. Discharge and source impedance control appeared to be the main problem since the entire sustainer capacitor was dumped in ~ 5 μsec.

Arc-free operation in the CO_2 mix could not be achieved, with even a small sustainer field applied. This is believed to be due to thermal instabilities and the presence of electronegative species produced by the discharge. It should be pointed out that the circuit of Fig. 13 did not
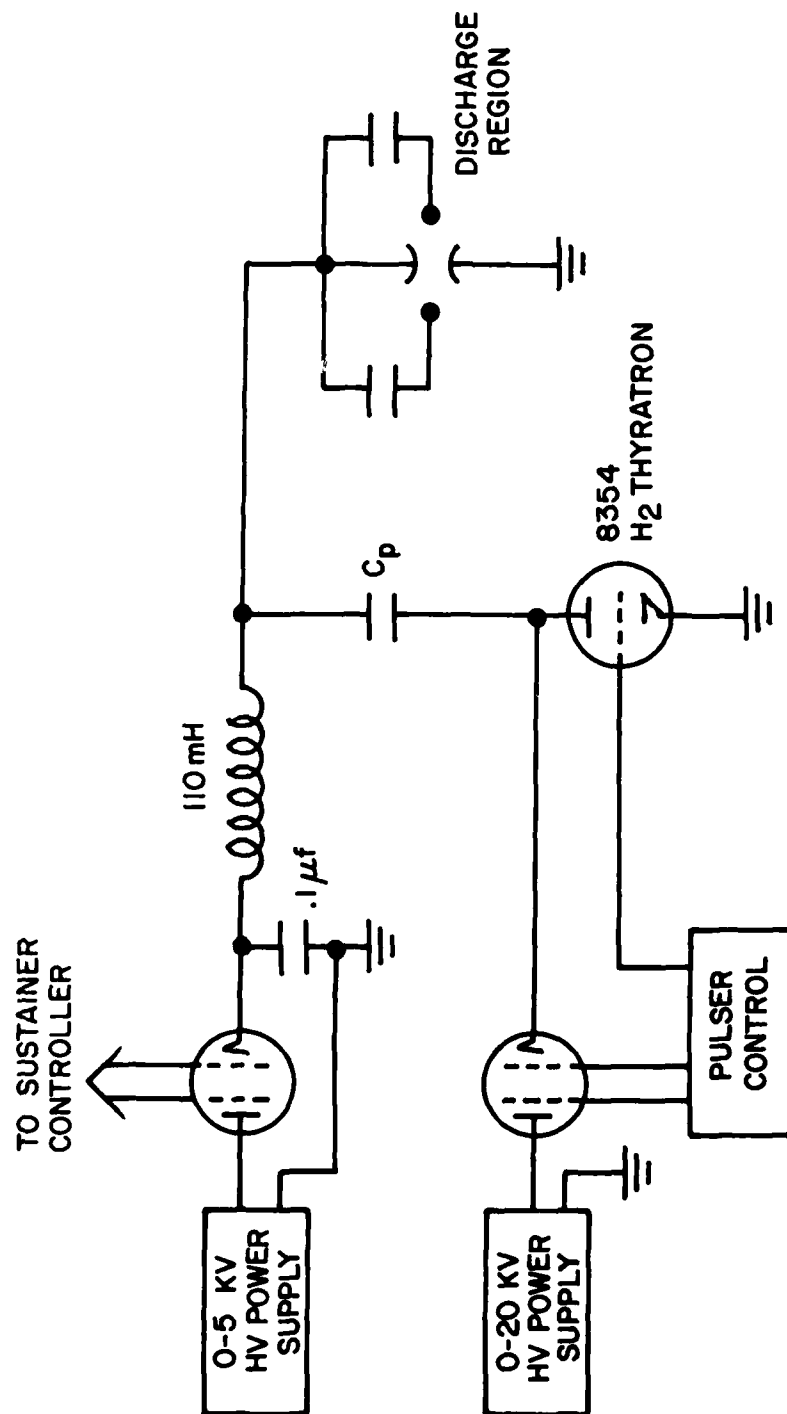
Figure 13. Schematic of simple poker pulser.

provide a fast initial high-voltage spike. Consequently, the electron density gradually increased over the first three to six pulses. This may have resulted in instabilities which prevented an appreciable electron-density buildup.

A simplified computer model was developed in order to evaluate the effect of the E/N-dependent attachment of electronegative discharge products upon electron density. Assuming diffusion and electron detachment to be negligible, the electron continuity equation is

$$n_e \, \alpha W - \gamma n_e^2 - n_e \, aW = 0 \qquad (10)$$

where n_e is the electron density, W is the drift velocity, and α, γ, and a are the ionization, recombination, and attachment coefficients, respectively. Using a Runge-Kutta integration method and the values of Lowke, et al.,[49] for W. α, γ, and a, the electron number density was calculated and plotted as a function of time for various sustainer levels. Figure 14 shows the temporal evolution of the electron density generated by a single poker pulse for a 1:1:8 CO_2:N_2:He mixture at several sustainer voltages. The pulse was assumed to be triangular with a 22-kV peak and a 100-nsec total width, superimposed on the sustainer level. The high decay rate for E/N = 1.5×10^{-16} V-cm^2 shows the effect of the high attachment rate. However, at the lower applied fields, the plasma appears to be entirely recombination dominated. This effect is, of course, dependent upon the gas composition. For a 1:2:3 mixture, for example, attachment would not be significant until E/N reaches ~ 2.5×10^{-16} V-cm^2 whereas for the mixture studied here (1:1:8), an E/N of as low as 1.3×10^{-16} V-cm^2 would result in an appreciable electron loss.
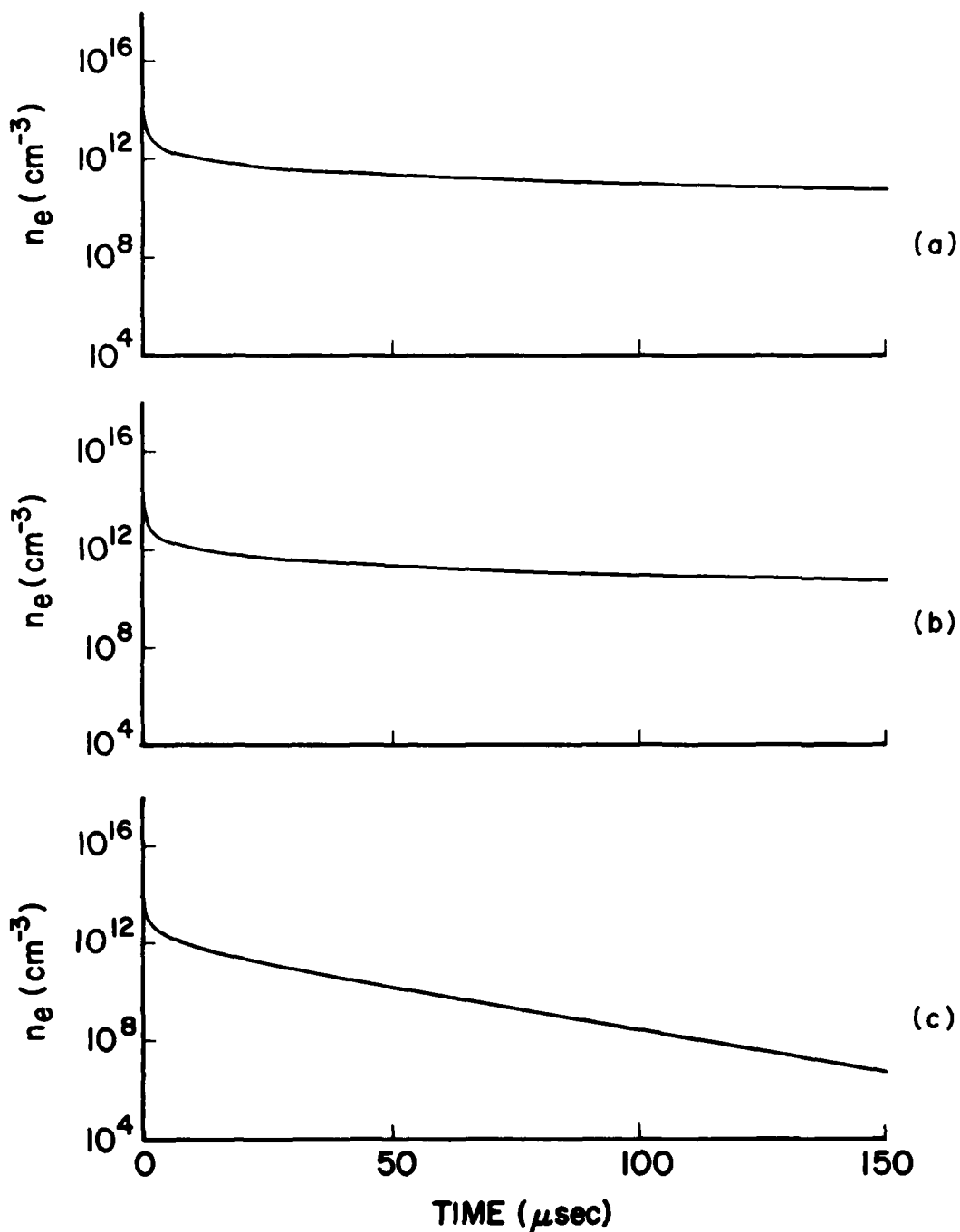
Figure 14. Computed electron-density decay in a 1:1:8 $CO_2:N_2:He$ laser mix.
Electrode gap = 1 cm; pressure = 400 Torr; poker pulse = 22 kV
peak amplitude, triangular shape of 100 nsec total width.
(a) Sustainer voltage = 20 V (E/N = 1.5 × 10^{-18} $V-cm^2$),
(b) Sustainer voltage = 1000 V (E/N = 7.6 × 10^{-17} $V-cm^2$),
(c) Sustainer voltage = 2000 V (E/N = 1.5 × 10^{-16} $V-cm^2$).

Figure 15 shows the computed time-varying electron density resulting from a series of 20-kHz, 20-kV poker pulses with a sustainer field of 1 kV on a 1-cm gap in a 400-Torr 1:1:8 mixture at room temperature. An initial uniform electron density of 10^4 cm^{-3} was assumed. Each high-voltage pulse generates a peak n_e of $\sim 10^{17}$ cm^{-3} with a rapid decay to 10^{13} cm^{-3}. The interpulse period shows a two-decade fall-off of n_e. For the fixed E/N of the sustainer field, this corresponds to a variation in current density of two orders of magnitude--from ~ 10 A/cm^2 to ~ 0.1 A/cm^2. Experimental results have indicated that this plasma-impedance change does exist. It appears that a poker repetition rate of greater than 100 kHz would be required just to limit the power-loading fluctuations to within one order of magnitude; ten times this rate would be necesssary for $\sim 20\%$ variation.

A more stringent control of the poker-pulse height and width would be advantageous in controlling the large overshoot in current density, but this would not change the interpulse characteristics. That is, a high repetition rate would still be required in order to maintain an appreciable power loading.

Considering the extent of current-density fluctuations in a CO_2 laser mix, it does not seem practical to utilize the poker concept in our configuration for quasi-cw operation. When taking into account the added problems of decreased preionization and increased thermal instabilities at higher pressures, the use of poker pulses for ionization-level control is unattractive for closed-cycle TEA laser operation.

The poker concept, however, may be promising for rare-gas-discharge lasers in the case where excitation is a result of electron-energy transfer, as with the ArXe laser. On the other hand, the poker circuit would be

47
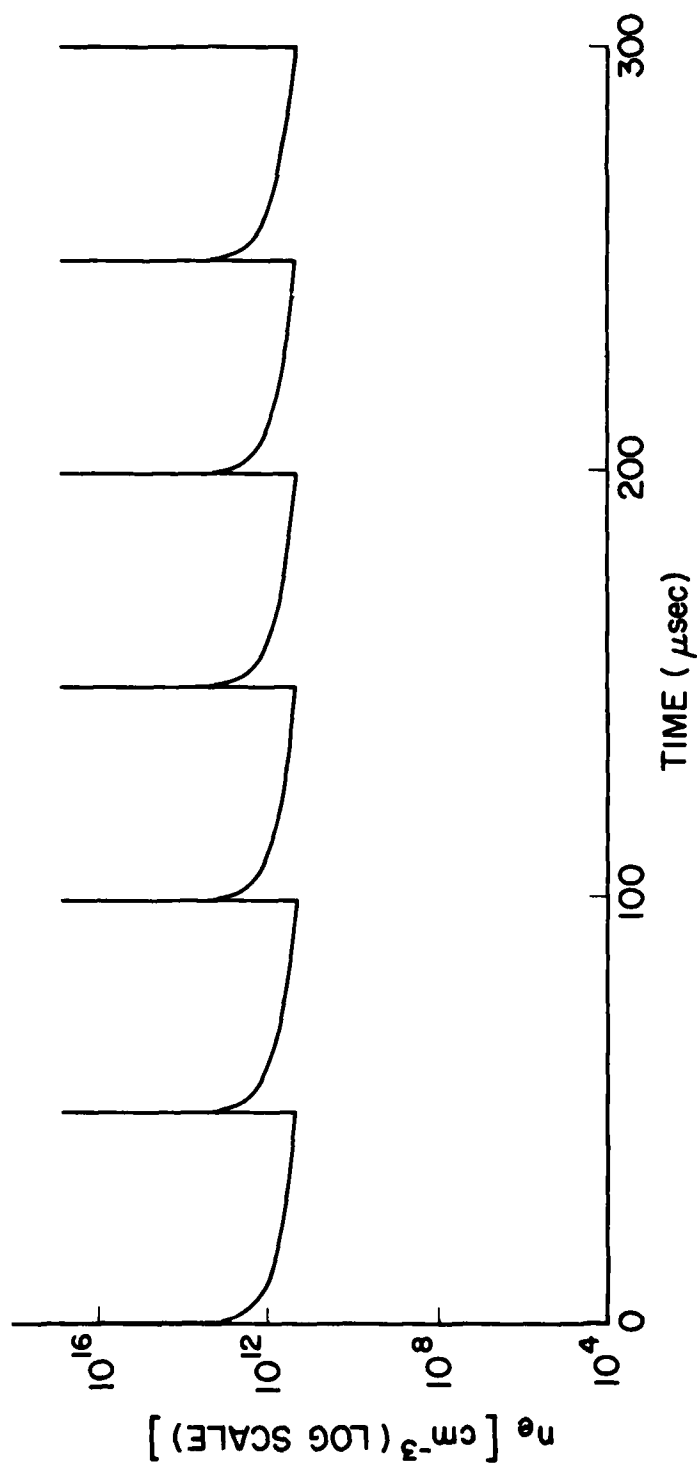
Figure 15. Calculated electron density for a 20-kHz poker pulse repetition rate in a 1:1:8 $CO_2:N_2:He$ laser mix. Electrode gap = 1 cm; pressure = 400 Torr; poker pulse = 20 kV peak amplitude, triangular shape of 100 ns total width.

detrimental if excitation were due to recombination, as suspected in the HeXe laser. An increase of the sustainer field should decrease the afterglow laser output in this case, due to the reduced recombination at higher electron temperature.

The circuit of Fig. 13 was modified for operation with a mixture of 400-Torr He, 1-Torr Xe. The sustainer-control tetrode would not operate properly due to the anode-cathode bias condition; therefore, it was replaced with a short, and a 10-Ω ballast resistor was installed between the 0.1-μf filter capacitor and the choke. Only the 2.03-, 2.65-, and 3.65-μ laser pulses were observed. The amplitude of the 2.03- and 3.65-μ pulses decreased ~ 30%, while the afterglow portion of the 2.65 μ pulse disappeared when the sustainer field was varied from 0 to 160 V (E/N = 1.2 $\times$ 10^{-17} V-cm^2).

In a mixture of 300-Torr Ar, 1.5-Torr Xe, six laser lines were observed: 2.03, 2.48, 2.63, 2.65, 3.11, and 5.57 μ. A slight increase in power was seen with increasing sustainer field, but the results are inconclusive due to discharge-stability limitations. However, the increase in intensity of the 2.65-μ pulse appeared to follow the decrease in overshoot of the poker pulse. In other words, the sustainer may have cancelled the field present during the afterglow pulse.

SECTION IV

ANNULAR-FLOW-RETURN LASER

4.1   DESIGN

A compact, closed-cycle, fast-transverse-flow, high-repetition-rate laser
was achieved in a novel design utilizing an annular flow return surrounding
the laser flow channel. The annular-flow-return configuration was chosen
for applications having severe size and weight restrictions since it is the
most compact geometry for recirculating flow.

The laser was constructed of ultrahigh-vacuum components and low-
outgassing materials to ensure minimum contamination of the laser medium.
A side view of the laser is shown in Fig. 16. The outer stainless steel
vacuum envelope is 12 in. in diam. and 50 in. long. A 6-in.-diam.
vaneaxial fan capable of 600 CFM provides up to 275 ft/sec flow through
a 1-cm gap between Rogowski-profile electrodes. Equal-area turning vanes
are used to channel the flow from the annular return to a settling chamber
in which a honeycomb flow straightener is used to remove swirl and large-
scale lateral velocity variations. A bellmouth inlet is used to channel
the flow into the interelectrode region of 1×28 cm^2 cross section. A
diffuser, comprised of a short length of 6-deg. expansion followed by
a wide-angle expansion, channels the flow from the discharge region to
the fan inlet.

Contamination by the gas-recirculation fan is avoided by employing
an external drive through a ferrofluidic rotary vacuum seal. The externally
driven fan assembly is flange-mounted to one end of the vacuum envelope.
A ferrofluidic seal is mounted through a hole in a vacuum bulkhead using
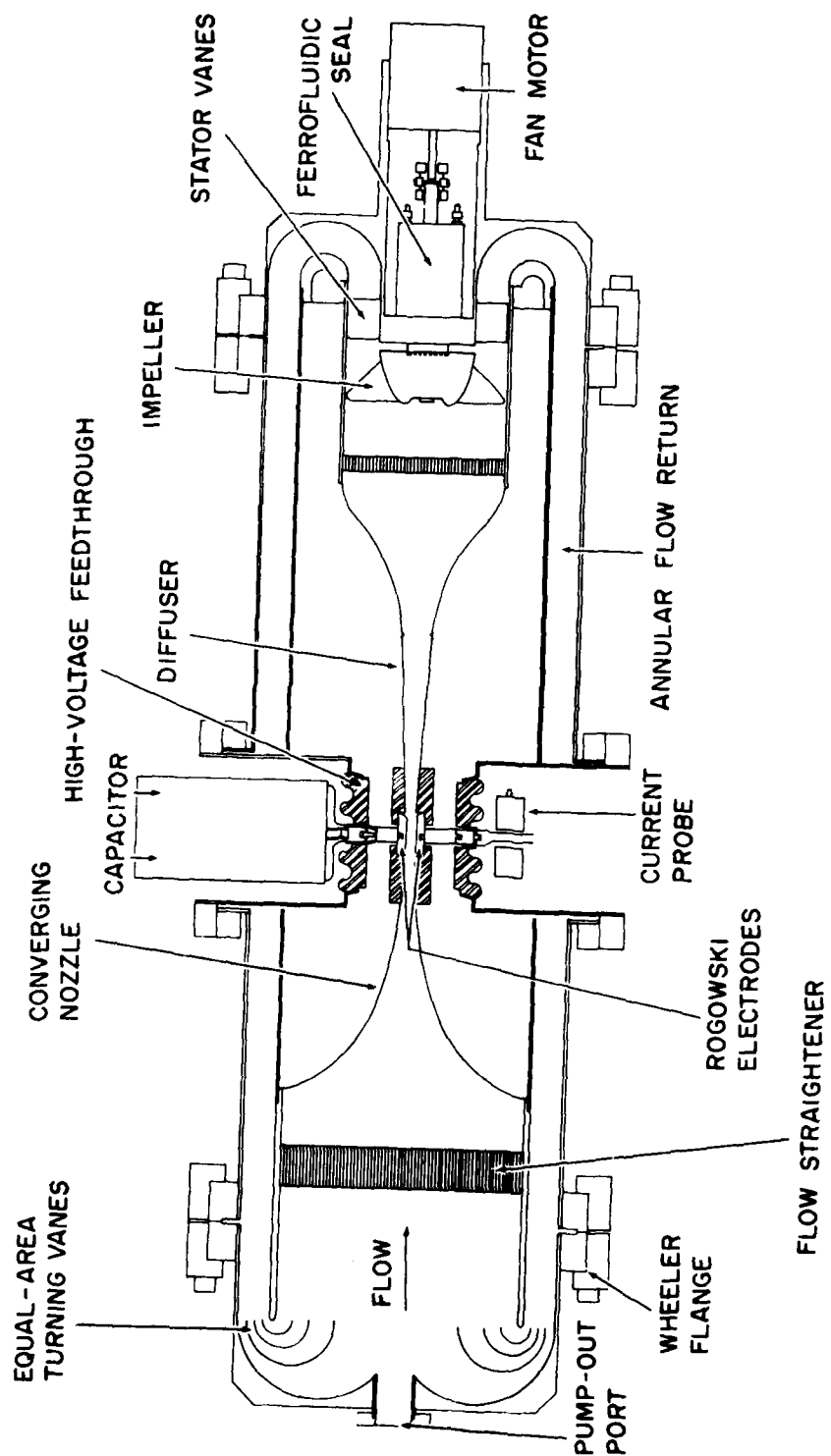
Figure 16. Closed-cycle annular-flow-return laser.

a Viton O-ring as a vacuum seal between the bulkhead and the body of the seal. An aluminum impeller is mounted on the rotary seal shaft extending into the laser flow channel. The atmospheric side of the shaft is connected to the shaft of a 400-Hz motor via a high-speed flexible coupling.

Rogowski-profile electrodes are mounted to flat glass plates, and the electrode gap is set to 1 cm by means of glass spacers at the outer ends of the plates. Preionization wires (0.25-mm diam.) positioned at the electrode midplane are suspended along the length of the electrodes on the upstream and downstream sides. The energy-storage capacitor is connected to the discharge cathode through a low-inductance,high-voltage, high-vacuum feedthrough. A thyratron is coaxially mounted atop the energy-storage capacitor. A schematic diagram of the pulser circuit is given in Fig. 22 of Ref. 40.

An optical cavity is established at right angles to the discharge and flow axes as shown in Fig. 17. The internal-mirror mounting configuration employs 1-in.-diam. mirrors affixed to 2 3/4-in. Conflat flanges which are bellows-mounted to 8-in.-diam. flanges. A micrometer-driven pivoting mechanism (mounted to the 8-in.-diam. flange) is used for mirror alignment.

4.2   VELOCITY PROFILE

The velocity profile in the discharge region of the annular-flow-return laser (AFRL) was measured by translating a 1/16-in.-o.d. Pitot-static probe along the 28-cm length of the Rogowski electrodes at the midplane of the electrode gap. Measurements were made in atmospheric-pressure air. Data obtained for the fan operating at ~ 70% of its

THYRATRON

FAN

DIFFUSER

MIRROR MOUNT

DISCHARGE SECTION

INLET

FLOW STRAIGHTENER

TURNING VANES
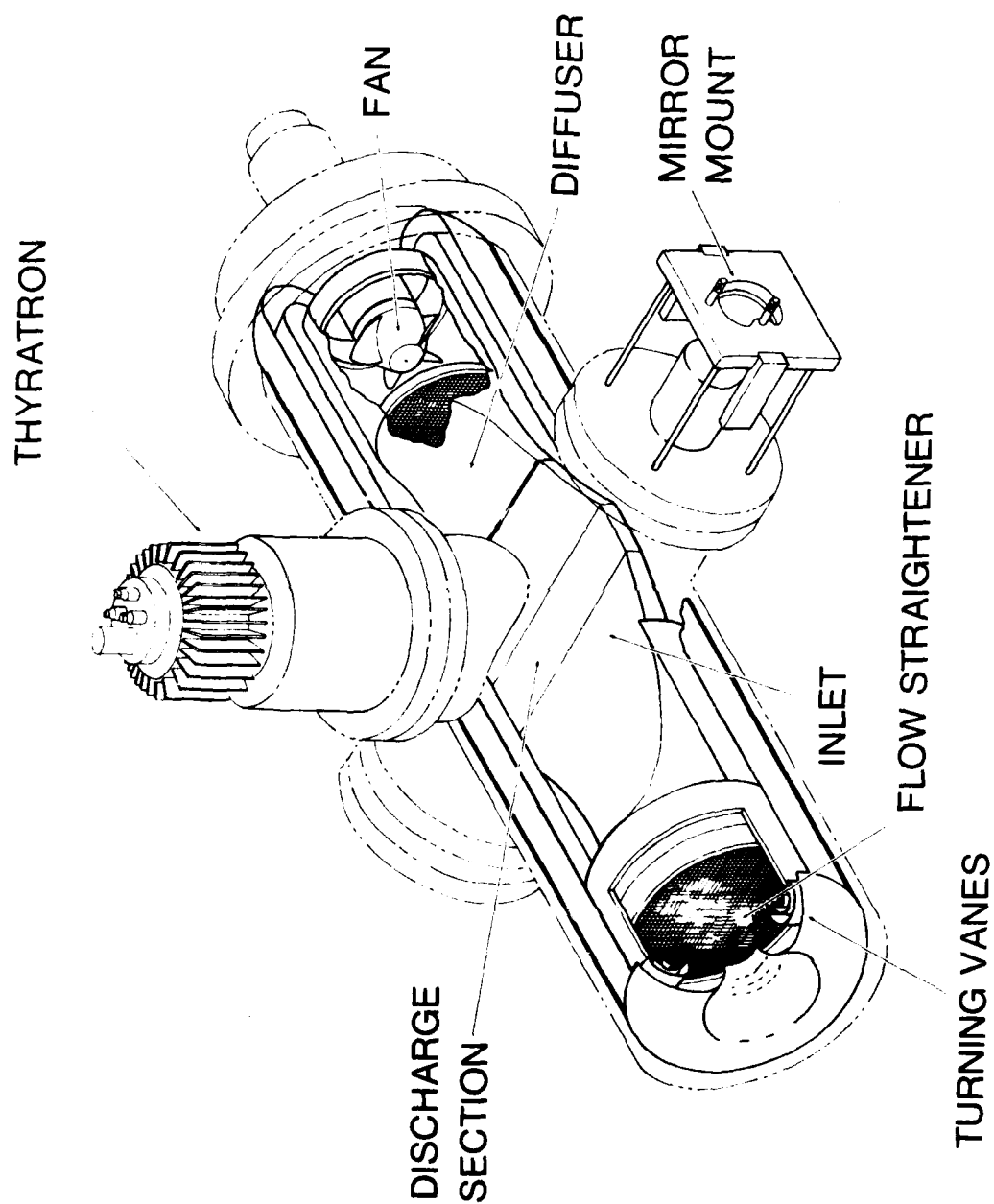
Figure 17. Isometric drawing of closed-cycle annular-flow-return laser.

rated speed are shown in Fig. 18. The maximum Δp in this figure corresponds to a velocity of 156 ft/sec which is approximately the same velocity as was obtained in the recirculating-loop system with the fan operating at 100% of its rated speed (see Fig. 4). It was not possible to measure the velocity profile in the AFRL with the fan operating at full speed because motor overheating activated the thermal cutout after a few minutes of operation. During intermittent operation at full speed, velocities of up to 275 ft/sec were attained. This is a 70% increase over the velocity in the recirculating-loop system and points up the superiority of the AFRL-system flow geometry.

The actual velocity profile in the AFRL system is probably more uniform than that shown in Fig. 18 which is influenced by the geometry of the measurement setup. The velocities on the left-hand side of the profile are depressed due to blockage of the flow channel by the length of the Pitot probe. As the probe is withdrawn (to the right) and the blockage decreases, the velocity increases leading to a skewed velocity profile. The glitch on the right-hand side of the profile is probably an artifact due to flow through the Pitot-probe entrance hole.

4.3   DATA-ACQUISITION SYSTEM

In order to facilitate the acquisition and reduction of data for the parametric study of the AFRL, a data-acquisition system was developed around an existing H-P 2116C minicomputer. The configuration is shown in Fig. 19. The boxcar integrator, with a sample gate of 15 nsec, is swept in time across the optical-detector output. The boxcar is provided with a scan ramp by the signal averager, which digitizes and stores the boxcar output.
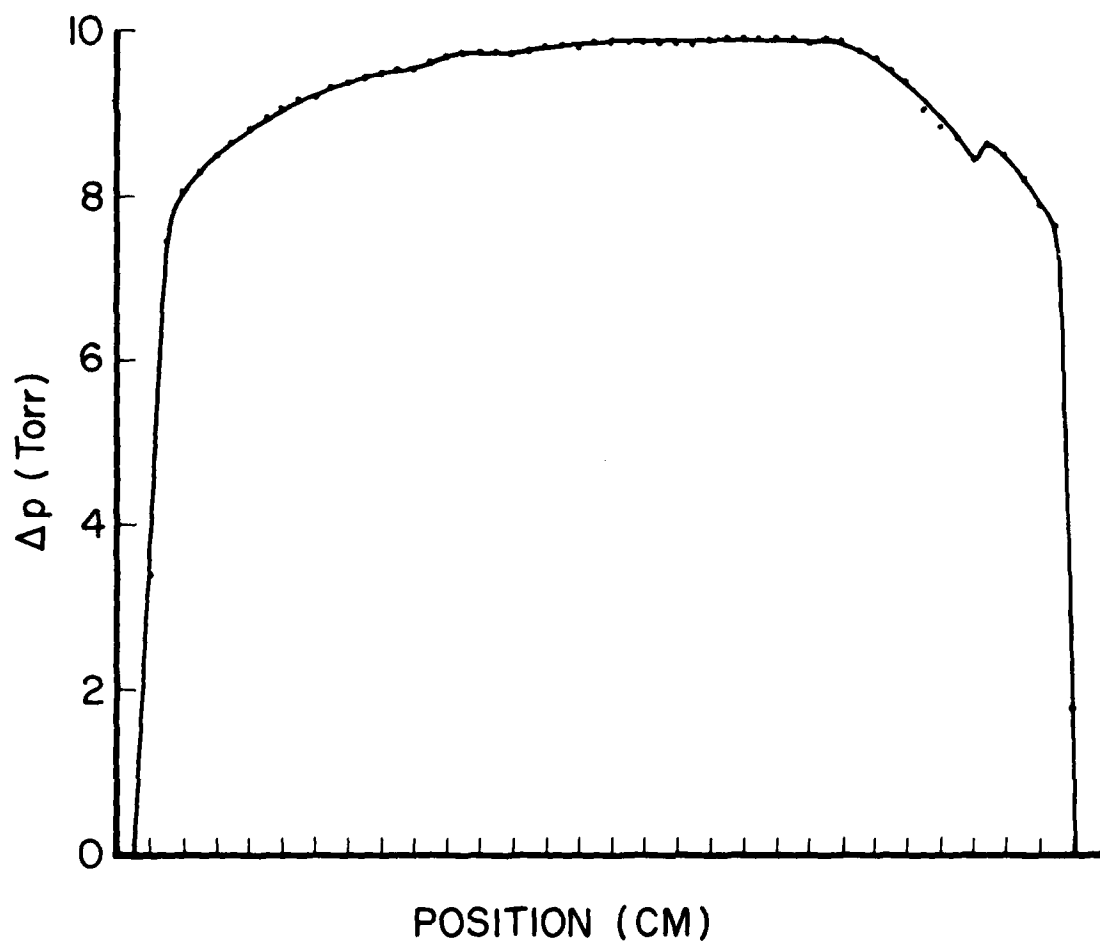
Figure 18. Velocity profile for annular-flow-return laser.
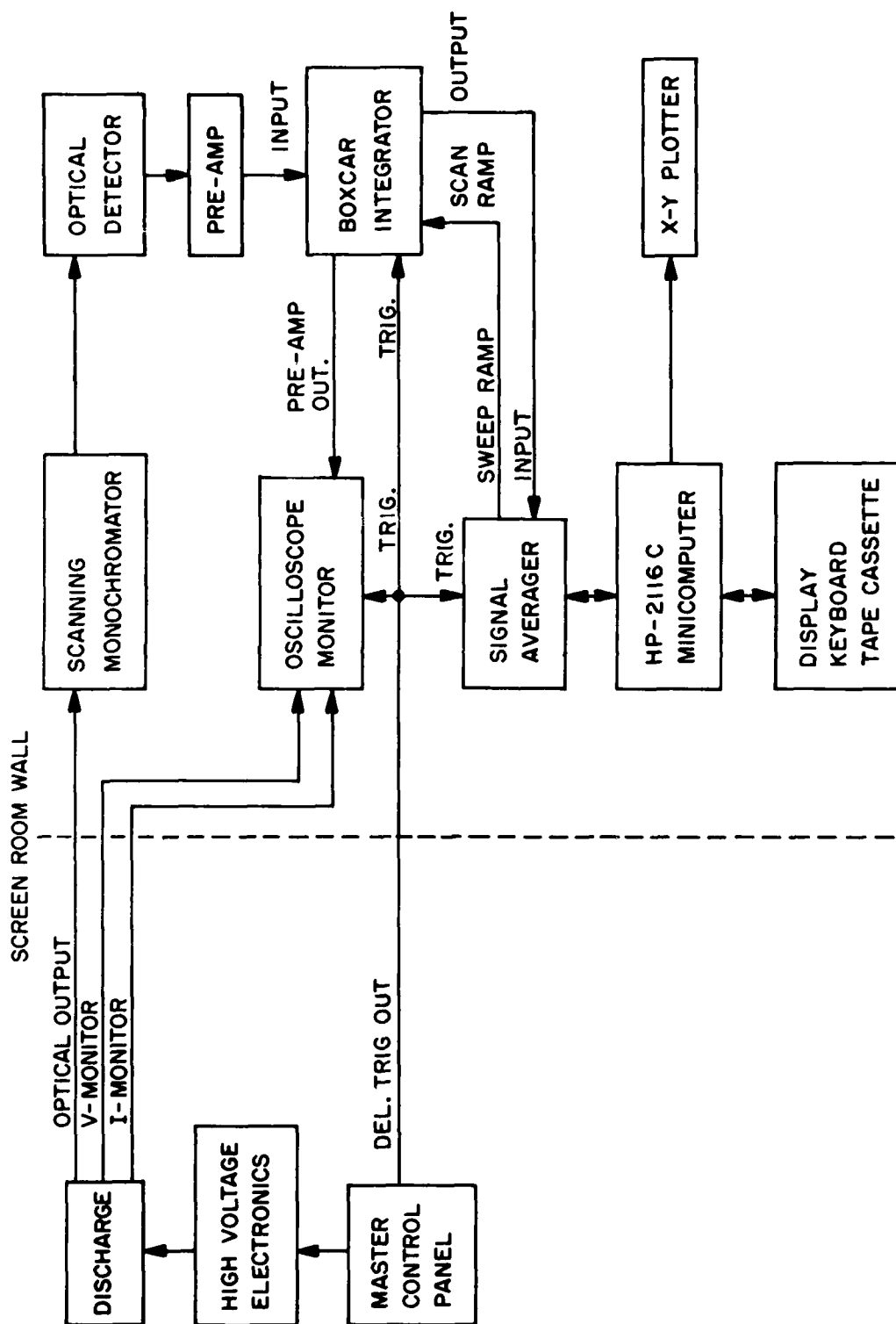
Figure 19. Data-acquisition system.

The digitized optical signal can be smoothed by averaging successive sweeps. Ideally, the detector output should be fed directly to the signal averager. However, the time region of interest is only ~ 10 μsec wide, which is much too short for the digitizing circuits. The function of the boxcar, therefore, is to stretch the signal to manageable levels (> 10 msec).

The main limitation of this scheme is a result of the 15-nsec gate time. Input-level fluctuations of 15 nsec or less are averaged by the boxcar circuitry and, as a result, the output is not a true representation of the input signal. This appears to be a problem only on the initial spike of the 2.03-μm line. A spike does appear on the digitized output, but the height is less than that shown on a high-speed scope.

A second limitation of the system can be attributed to the smoothing capability of the signal averager. If a large number of sweeps is averaged, a "clean" signal may be recorded--even though the actual input level may fluctuate a great deal. Care must be taken to average a minimal number of sweeps to insure that only electronic noise is filtered out.

Time synchronization with the discharge is provided by triggering the boxcar and signal averager with a delayed pulse from the thyratron discharge circuitry. The digitized data are passed from the signal averager through the minicomputer to a data terminal and stored on tape cassette along with other pertinent data. The original waveform can be recalled later for display on the signal-averager CRT, for hard-copy plotting, or for data analysis.

4.4 LASER-PERFORMANCE/PARAMETRIC STUDY

Preliminary measurements of the laser output from the AFRL indicated performance superior to that of the recirculating-loop laser. Measurements were made using a 68-cm optical cavity (internal mirrors) formed by a 2-m reflector and a Si output flat. A plot of the multiline, multimode average laser output power as a function of repetition rate for a 400-Torr, 2000:1 He-Xe mixture is shown in Fig. 20. The 3 W of average power at 12 kHz was the highest power at the highest rep rate achieved to that date. The fall-off in power at rep rates above 8 kHz was probably due to gas heating at high-power loading of the discharge (for example, at 12 kHz and 14 kV, the average power loading was 5.9 kW).

Oscillograms of the laser output pulses for the 400-Torr, 2000:1 He-Xe mixture are shown in Fig. 21. These data were obtained using a 5-nF capacitor charged to 12 kV at a repetition rate of 1 kHz. A previously unreported line was observed at 5.13 μ. This line has also been observed by W. Schuebel (AFAL) in a static discharge. He identified the transition as $4f[9/2]_5 - 6d[7/2]_4^o$. This line was not observed previously because the output-mirror transmission was too high (83%); the present mirror has 0.5% T at 5.13 μ.

The effect of gas temperature upon laser output is shown in Fig. 22, which is a strip-chart recording of the average laser output power as a function of continuous operating time. The fall-off in output power with time was attributed to gas heating since the power recovered when the laser was shut down and allowed to cool to room temperature.

A constant laser output was necessary for a parameter study of the AFRL because a data-acquisition time of 1 hr is required for a given set of

400 TORR He-Xe (1000:1)
$V_f \sim 75$ m/s
STORAGE CAP=5nF
CHARGING VOLTAGE=14kV
ACTIVE VOLUME=1x2x25 cm^3

AVERAGE OUTPUT POWER (W)

PRF (kHz)
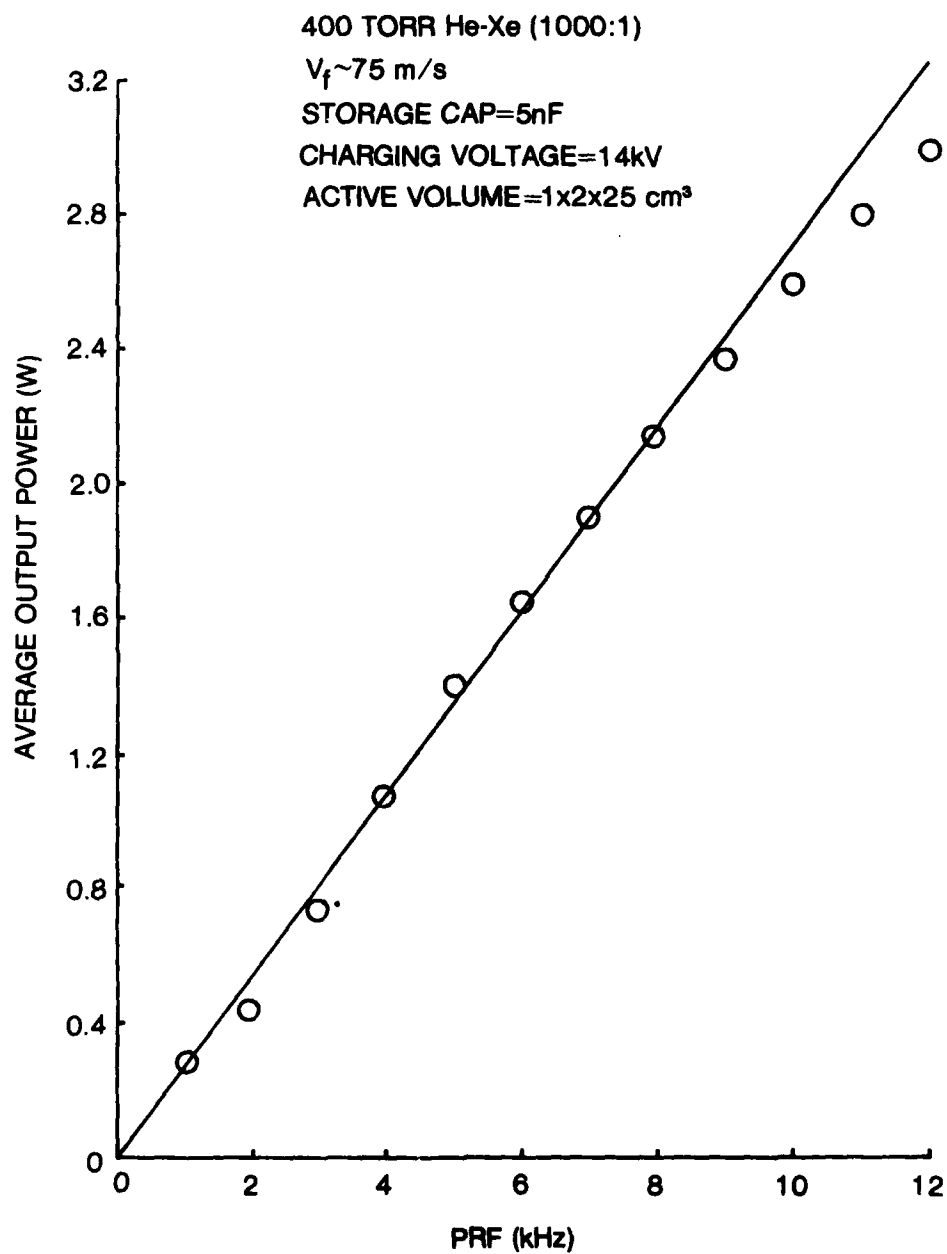
Figure 20. Dependence of average laser output power
upon PRF for 400-Torr He-Xe (1000:1)
mixture.

59

2.03μ

2.65μ

3.43μ

3.65μ

3.87μ

5.13μ
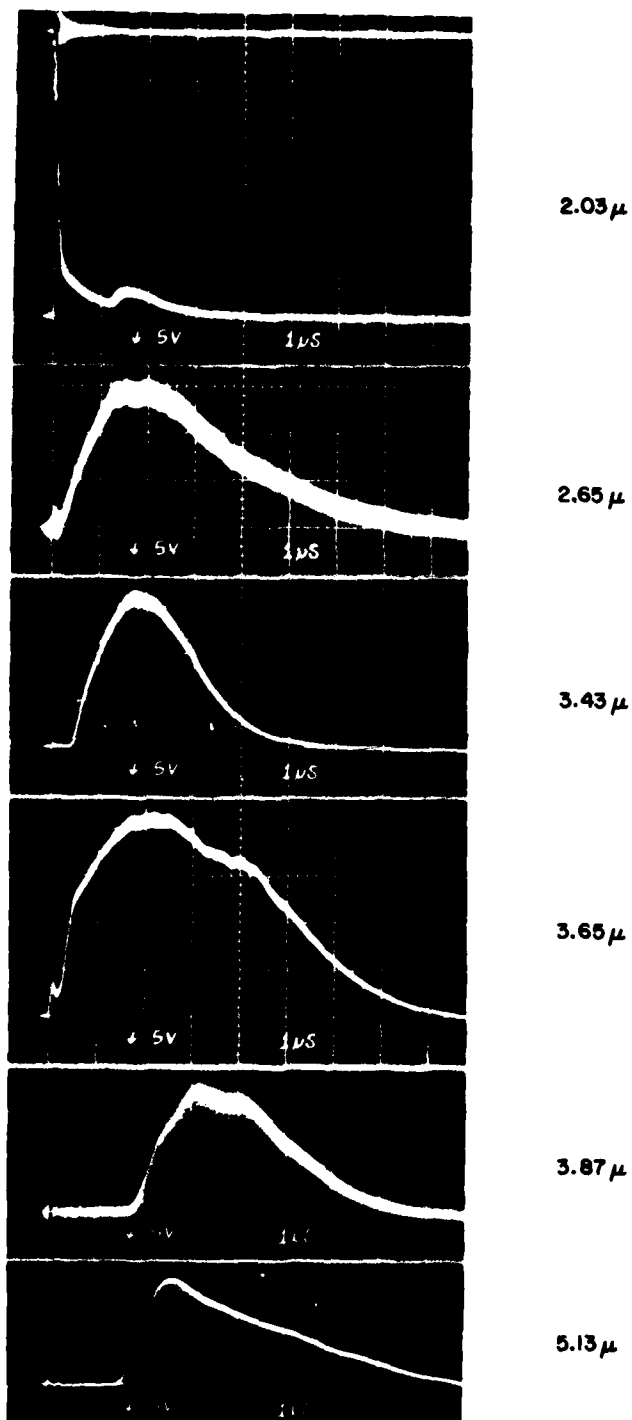
Figure 21. Oscillograms of laser pulses from annular-flow-return laser.
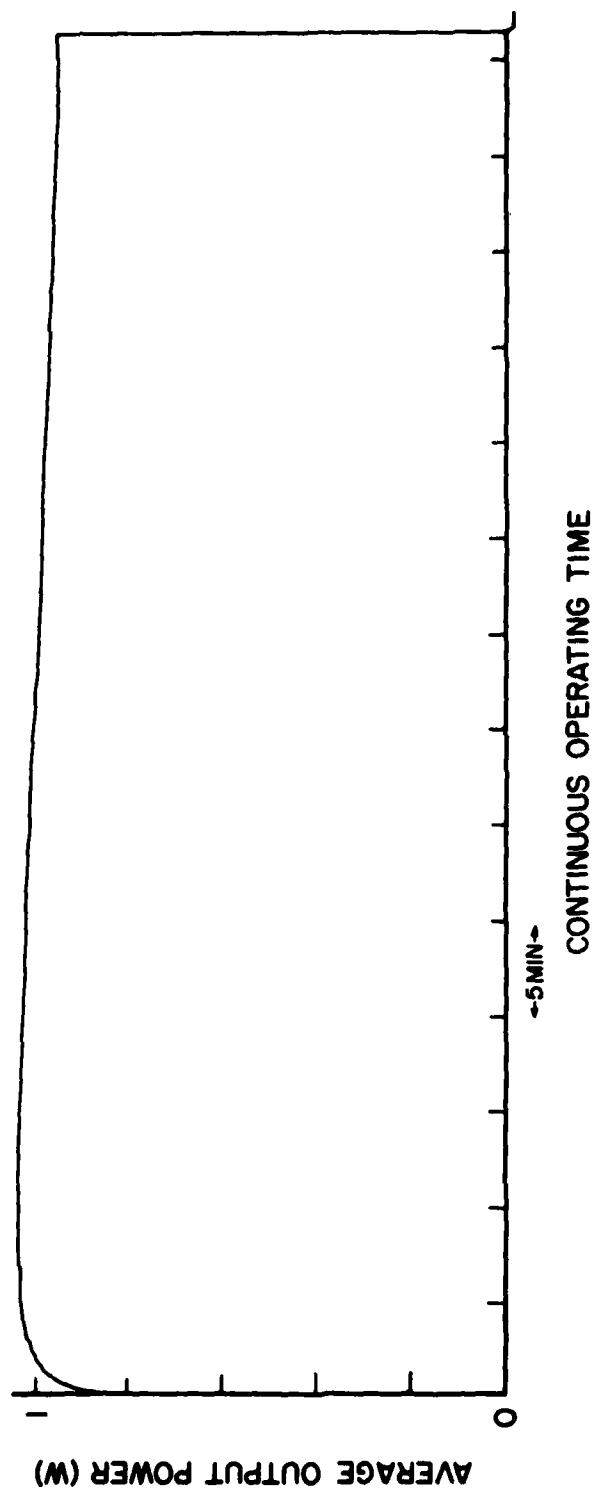
Figure 22.   Dependence of average laser output power upon continuous
operating time of annular-flow-return laser.

CONTINUOUS OPERATING TIME

←5MIN→

AVERAGE OUTPUT POWER (W)

61

parameters. In order to achieve the required constant laser output, the walls of the laser enclosure were cooled to maintain them near room temperature.

At rep rates of 1 kHz and above, the He-Xe discharge was found to operate satisfactorily without capacitive coupling of the discharge voltage to the preionization wires; in fact, this resulted in a slight increase in laser output power. The laser was thenceforth operated with the preionization wires floating.

A parametric evaluation of the performance of the annular-return laser was made for He-Xe mixtures with ratios from 200:1 to 10,000:1 at pressures from 200 to 1000 Torr. A CaF_2 lens was used to focus the laser output on the entrance slit of a Jarrell-Ash 0.5-m Ebert scanning spectrometer equipped with an infrared grating blazed at 5 μ. A liquid-nitrogen-cooled PbSnTe detector was used at the exit slit. Multiline, multimode average laser output power was measured with a Scientech 1-in. disc calorimeter placed ~ 4 in. from the laser output mirror.

The dependence of the laser output upon the following parameters was investigated: (1) total pressure, (2) He-Xe mixture ratio, (3) charging voltage, (4) PRF, (5) fan speed, and (6) gas temperature. All of the data were taken at a fan speed of 9700 rpm and a laser wall temperature near room temperature, unless otherwise indicated. A 5-nF energy-storage capacitor was used throughout the study.

Plots of discharge breakdown voltage and peak current as a function of charging voltage are shown in Figs. 23-26. The discharge voltage was

62
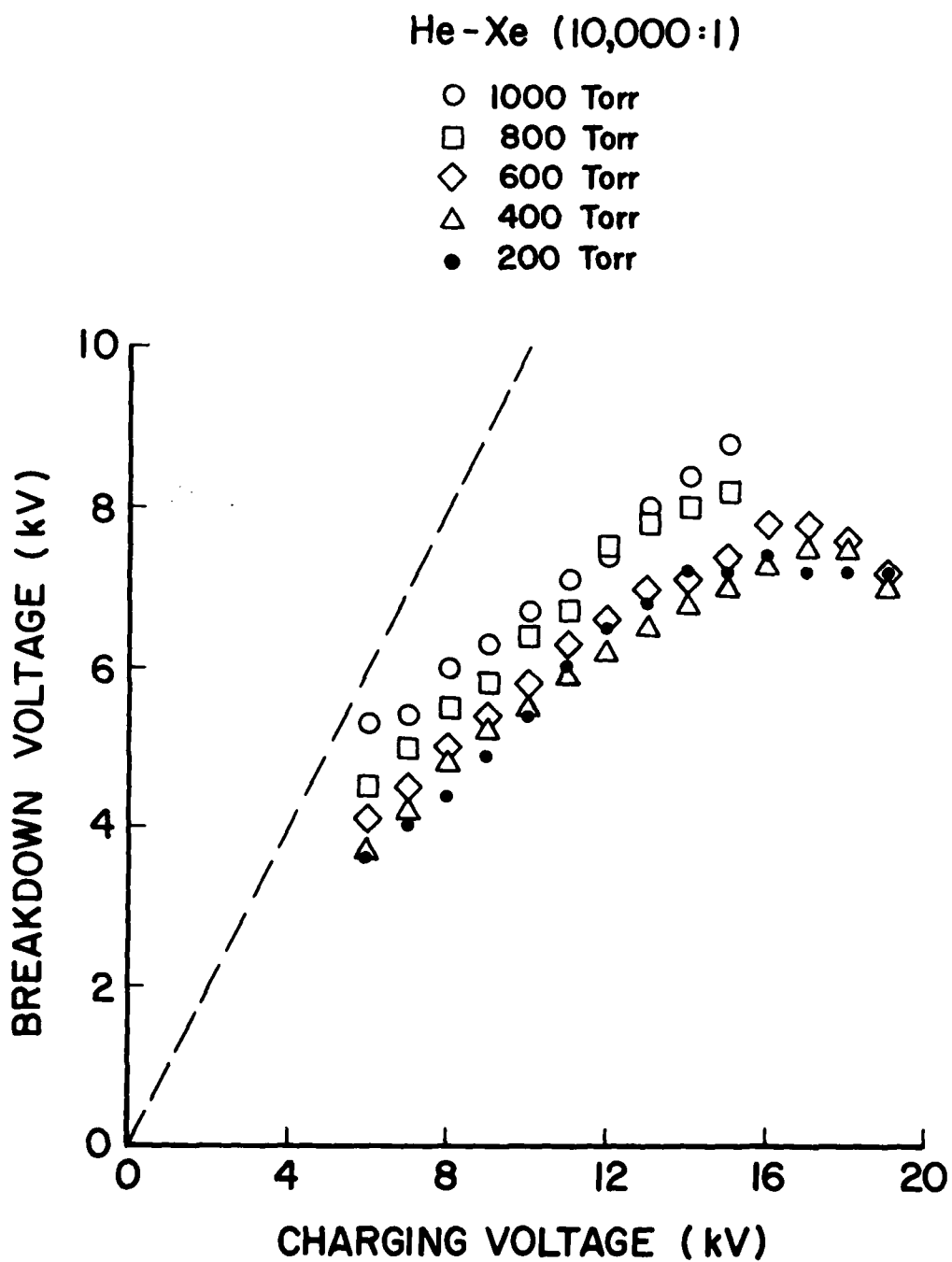
Figure 23. Dependence of discharge breakdown voltage upon charging
voltage for a 10,000:1 He-Xe mixture at pressures from
200 to 1000 Torr.
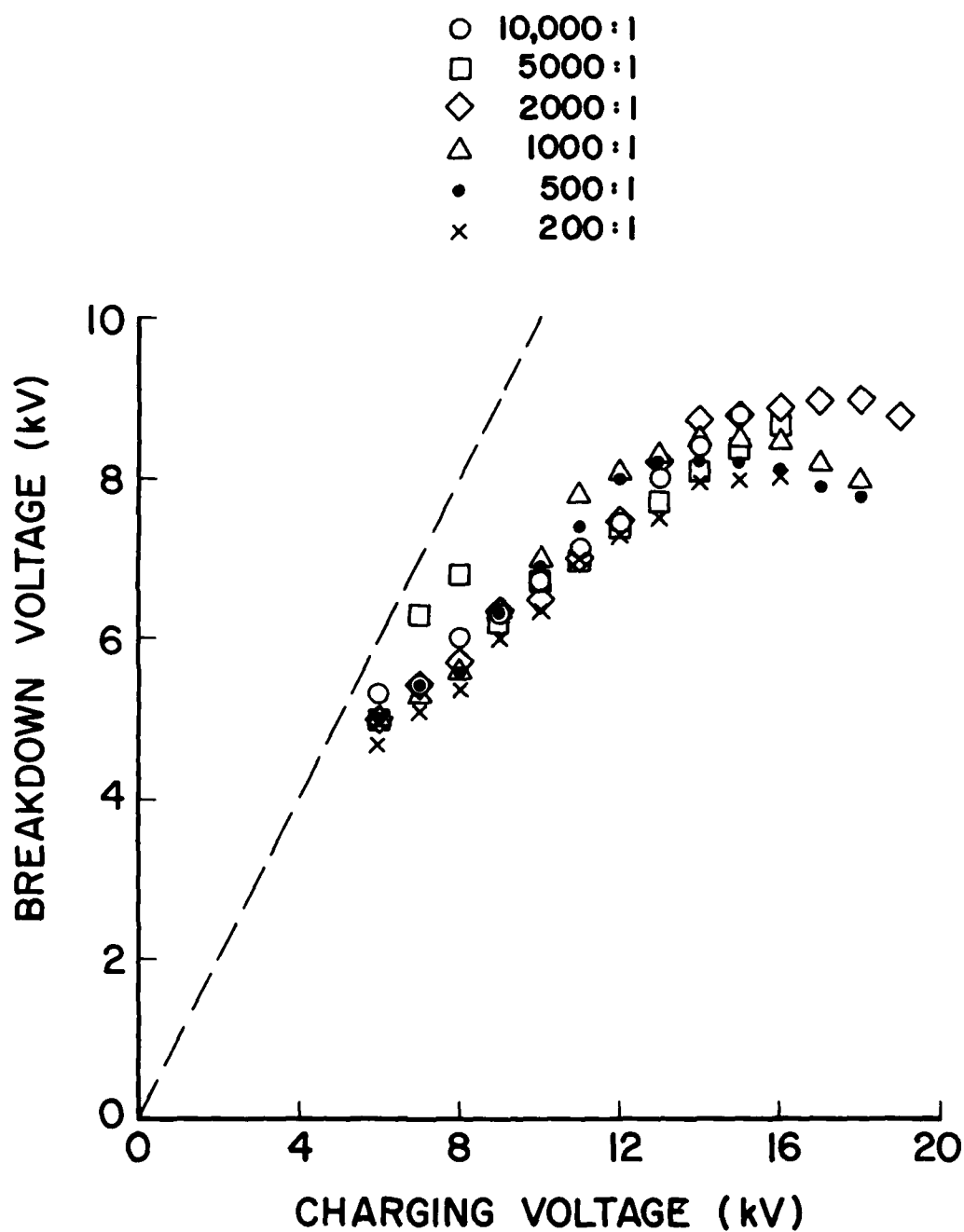
Figure 24.   Dependence of discharge breakdown voltage upon charging
voltage for He-Xe mixtures from 200:1 to 10,000:1 at a
pressure of 1000 Torr.
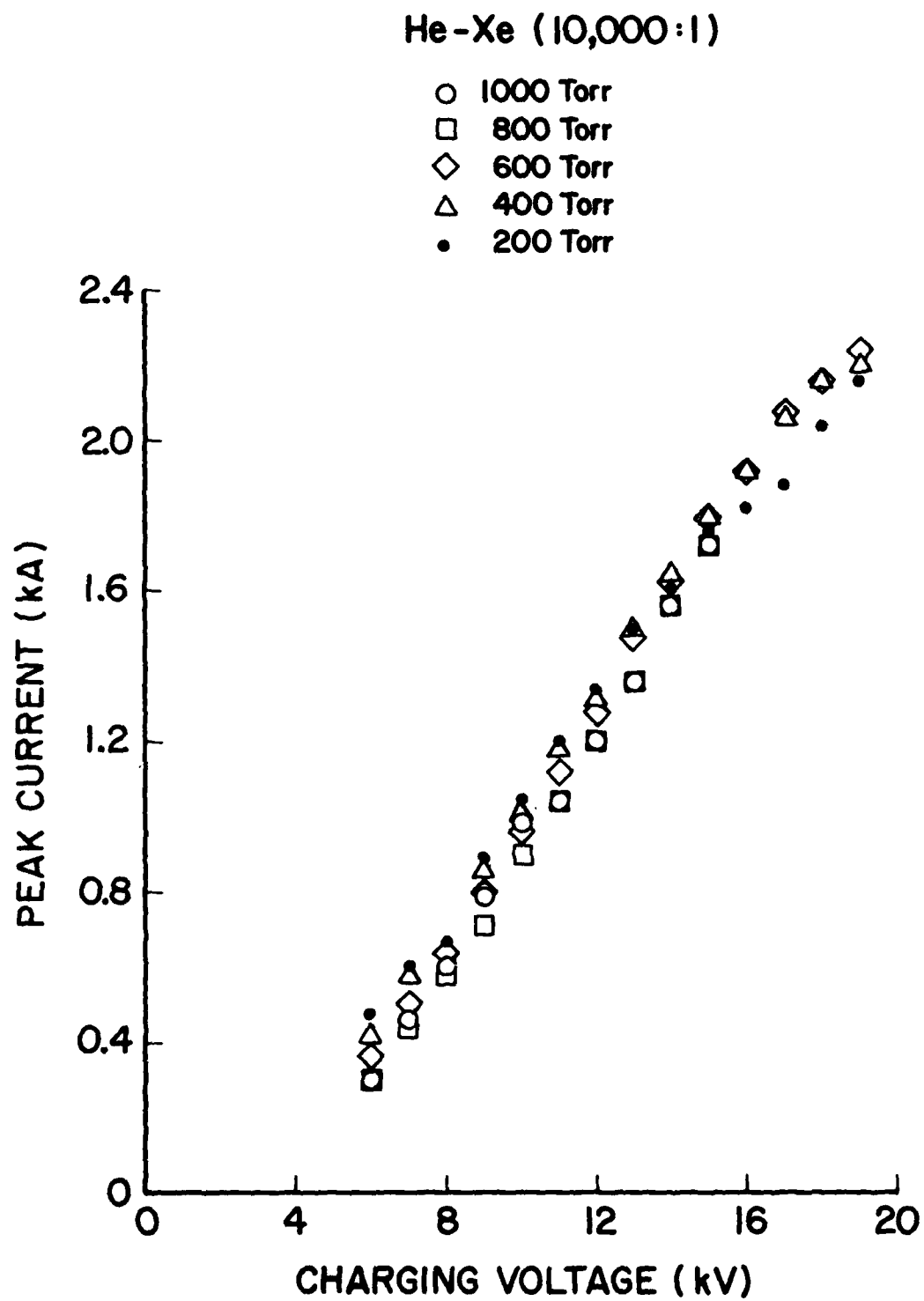
Figure 25. Dependence of peak discharge current upon charging voltage for a 10,000:1 He-Xe mixture at pressures from 200 to 1000 Torr.
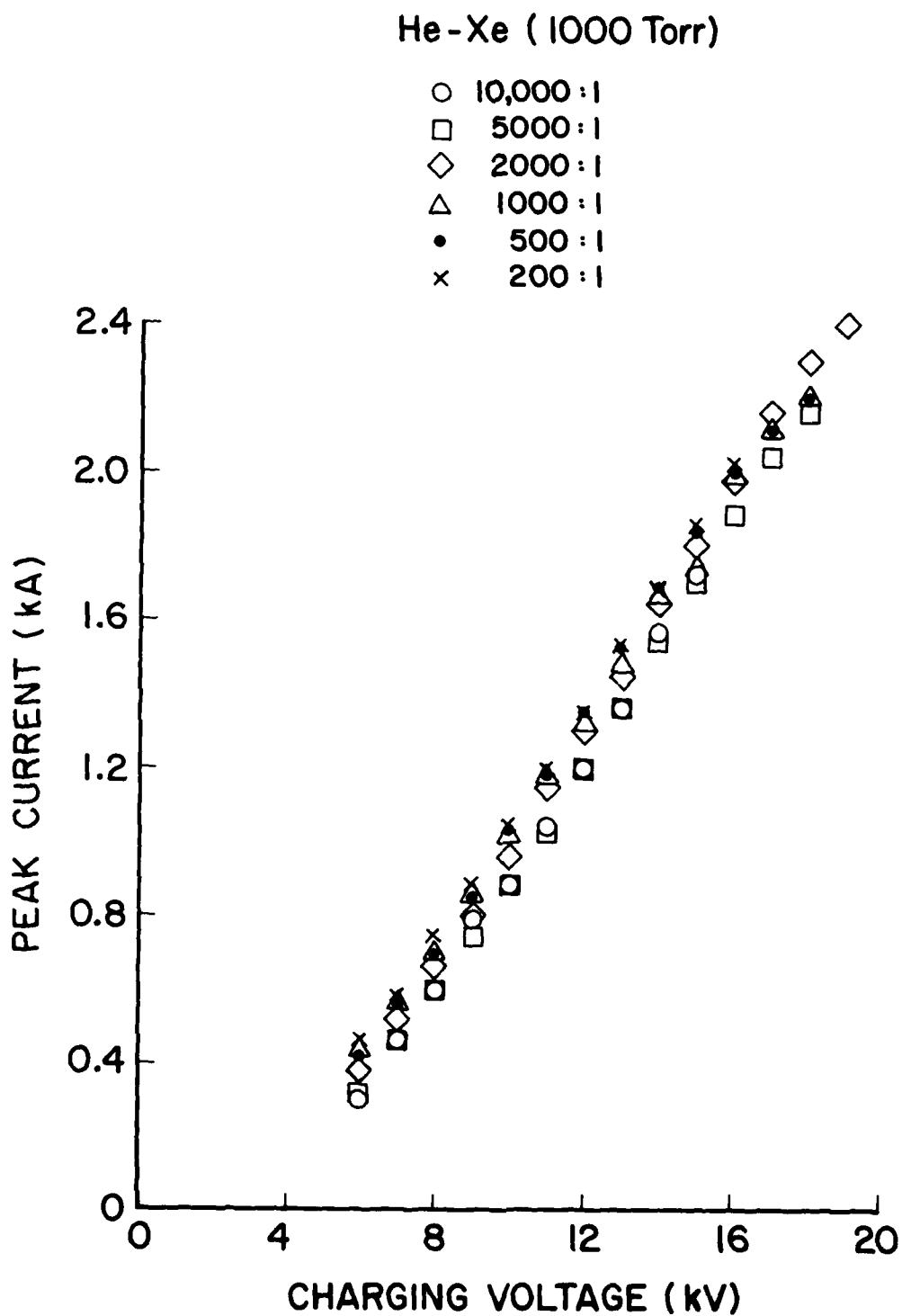
Figure 26. Dependence of peak discharge current upon charging voltage for He-Xe mixture at pressures from 200:1 to 10,000:1 at a pressure 1000 Torr.

measured with a Tektronix P 6013A high-voltage probe and the current with a Pearson Model 411 current transformer which surrounded the anode lead. A Tektronix 7904 oscilloscope was used to display the pulses thus recorded. The data were obtained at a PRF of 5 kHz. A saturation in discharge overvoltage at a level which increased with increasing pressure is evident in Fig. 23. Deviation from the 45-degree line indicates that the risetime of the applied voltage exceeded the discharge formative time lag,[50] resulting in breakdown at a level below the full capacitor-charge voltage. The breakdown voltages were lower than those obtained using a 2-nF capacitor,[40] indicating a slower voltage risetime due to higher inductance of the pulser circuit. Although the breakdown voltage tended to saturate with increasing charging voltage, the peak discharge current increased approximately linearly with charging voltage. In general, the discharge current increased with decreasing pressure and increasing Xe concentration.

The effect of gas temperature upon laser output is illustrated in Fig. 27. The falloff in laser output power with increasing wall (gas) temperature is probably due to the reduced recombination at higher temperature. Recombination pumping of upper laser levels is probable for He-Xe mixtures.[40] The data of Fig. 27 were obtained by cooling the laser end flanges and body with liquid nitrogen to the lowest temperature achievable and then permitting the laser to warm up while monitoring the laser output. During the parameter study, the laser wall temperature was maintained near room temperature by means of liquid-nitrogen cooling. The slow thermal response and poor heat transfer of the stainless steel wall resulted in

67
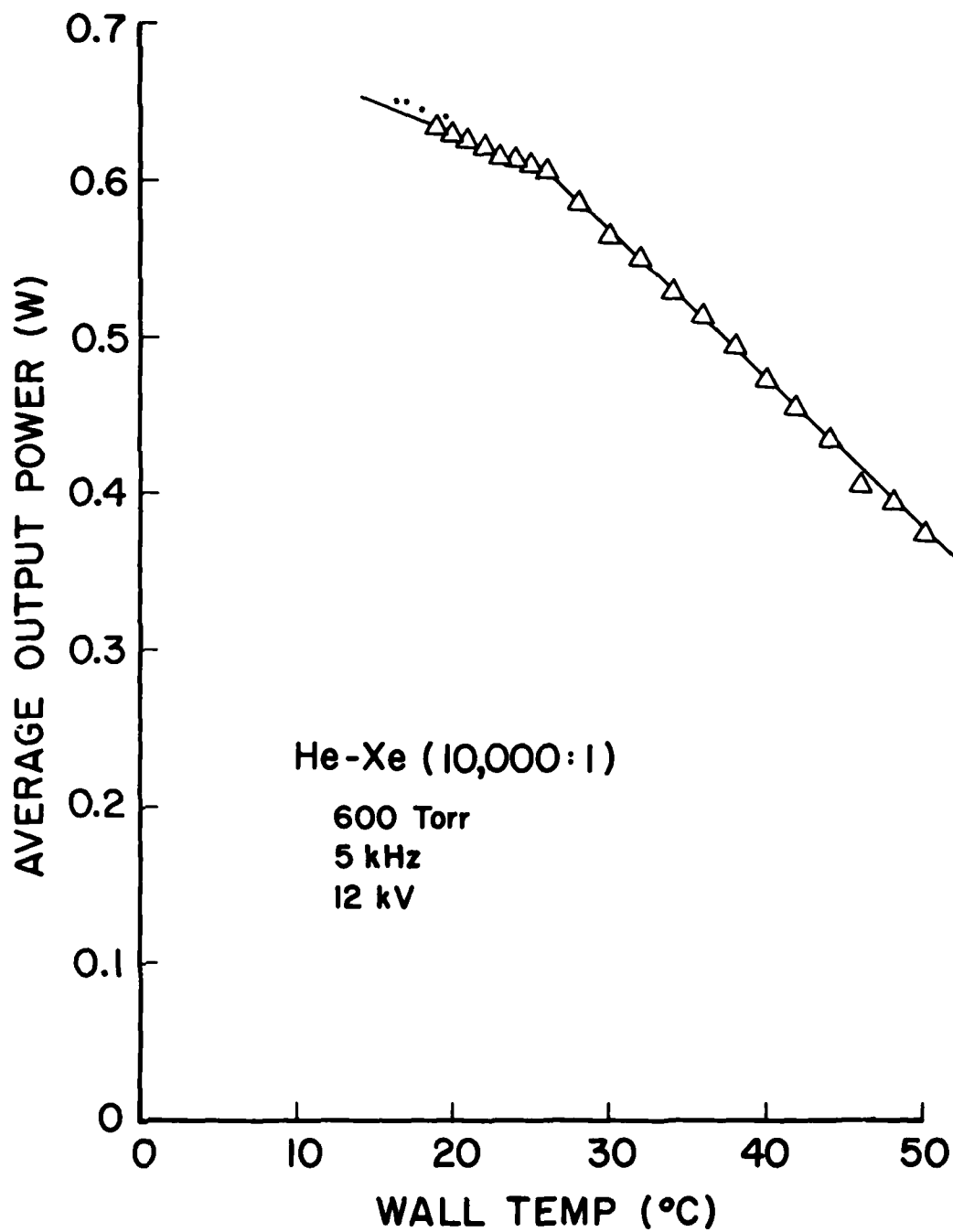
Figure 27. Dependence of average laser output power upon wall
temperature.

68

temperature variations of up to 8°C, with varying discharge loading conditions. An internal copper heat exchanger will be required to achieve a more constant laser output.

The laser output pulses from the various He-Xe mixtures at pressures from 200 to 1000 Torr are shown in Figs. 28-33. These data were obtained at a PRF of 5 kHz and a capacitor charging voltage of 12 kV and were processed by the pulse-digitizer system described in Section 4.3. At the appropriate pressures and He-Xe mixture ratios, lasing is simultaneous on the 5d-6p (2.03 and 2.65 μ), 7p-7s (3.05, 3.43, 3.65, and 4.02 μ), 5d'-6p' (3.87 μ), and 4f-6d (5.13 and 5.44 μ) transitions. The 5.44-μ pulse has not been observed previously and is tentatively identified as the $4f[9/2]_4 - 6d[7/2]_3^o$ transition. Figures 28-33 provide a comparison of the temporal responses of the laser pulses (but not of the pulse heights because the wavelength response of the grating and detector is uncalibrated).

The dependence of the peak laser output at each wavelength upon charging voltage is shown in Fig. 34 for a 500:1 He-Xe mixture at a pressure of 400 Torr and a repetition rate of 5 kHz. The domination of the 2.03- and 3.43-μ pulses is even greater than that which is apparent in the figure because the grating and detector responses degrade with wavelengths less than 5 and 10 μ, respectively. The curves indicate a maximum charging voltage of ~ 9 kV beyond which peak-laser-output efficiency decreases rapidly.

The dependence of the peak laser output at each wavelength upon total pressure is shown in Figs. 35-40 for He-Xe mixtures with ratios from 200:1 to 10,000:1. These data were obtained at a charging voltage of

He-Xe (200:1)
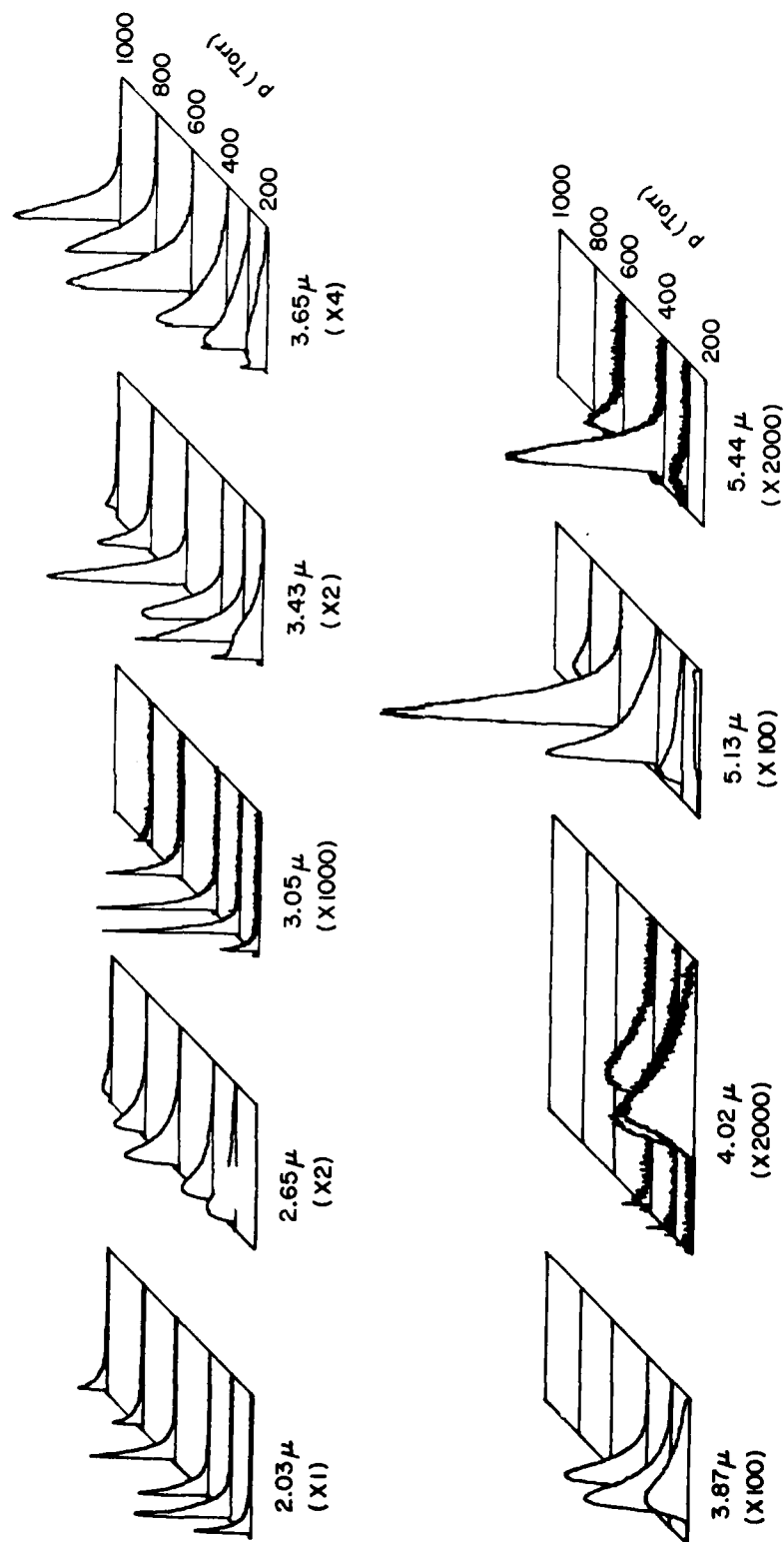
Figure 28. Laser pulses obtained for a 200:1 He-Xe mixture at pressures from 200 to 1000 Torr. Abscissa is 0-11 μs except for 4.02 μ which is 0-22 μs.

He-Xe (500:1)
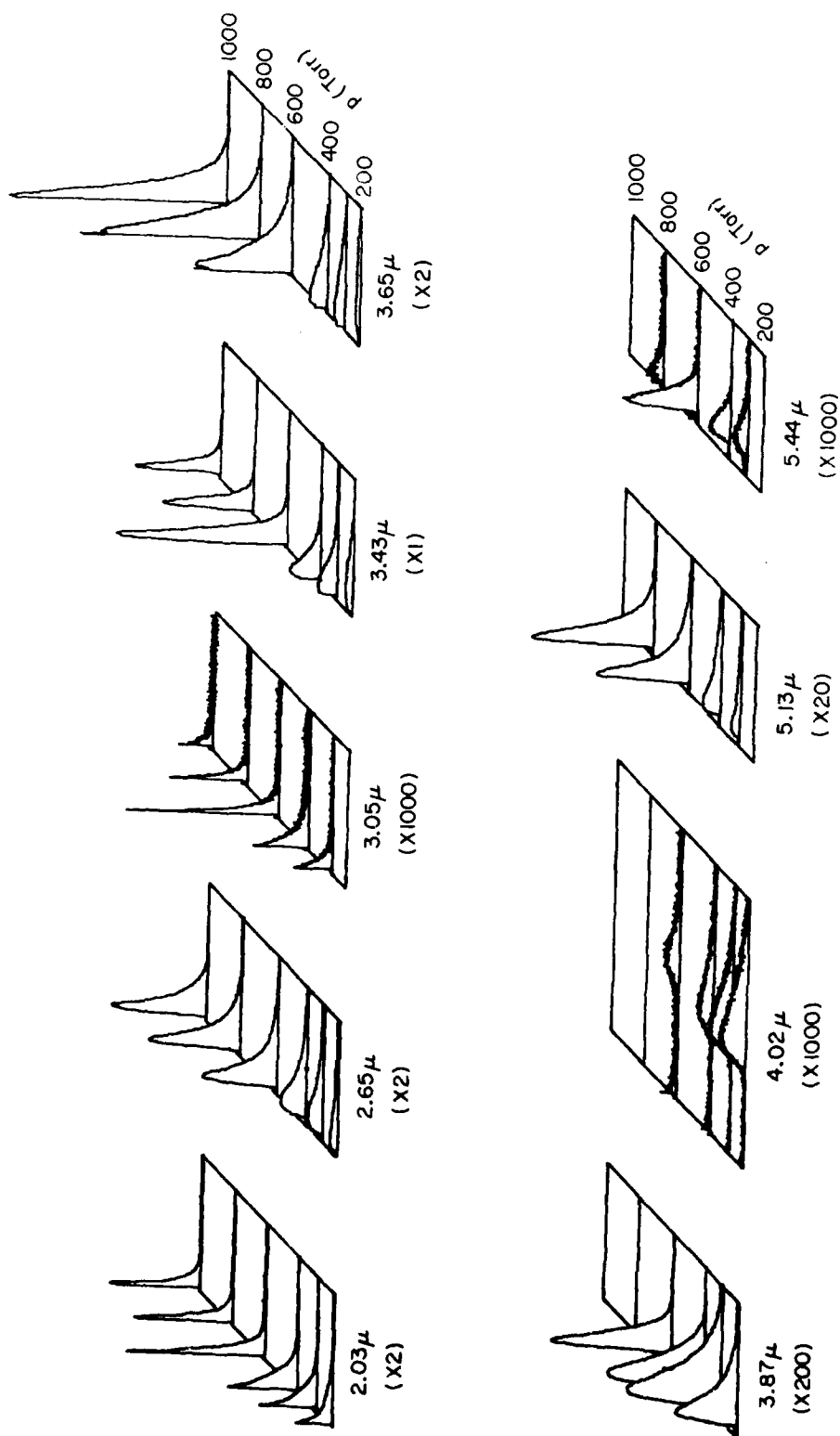
Figure 29. Laser pulses obtained for a 500:1 He-Xe mixture at pressures from 200 to 1000 Torr. Abscissa is 0–11 μs except for 4.02 μ which is 0–22 μs.

He-Xe (1000:1)
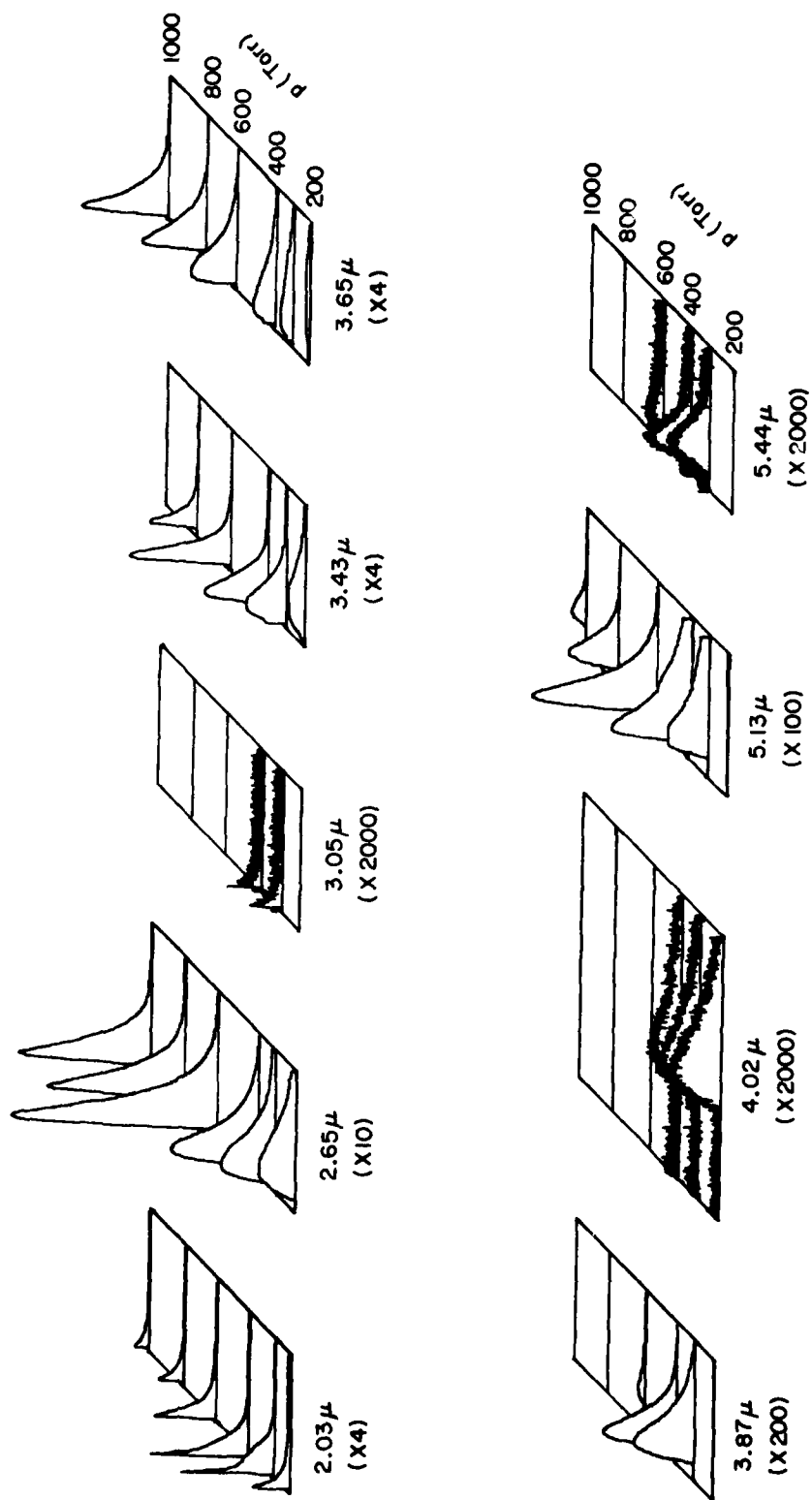
Figure 30. Laser pulses obtained for a 1000:1 He-Xe mixture at pressures from 200 to 1000 Torr. Abscissa is 0-11 μs except for 4.02 μ which is 0-22 μs.

He-Xe (2000:1)

2.03μ
(X10)

2.65μ
(X4)

3.43μ
(X4)

3.65μ
(X4)

3.87μ
(X400)

p (Torr)
200 400 600 800 1000

4.02μ
(X2000)

5.13μ
(X40)

5.44μ
(X2000)

p (Torr)
200 400 600 800 1000
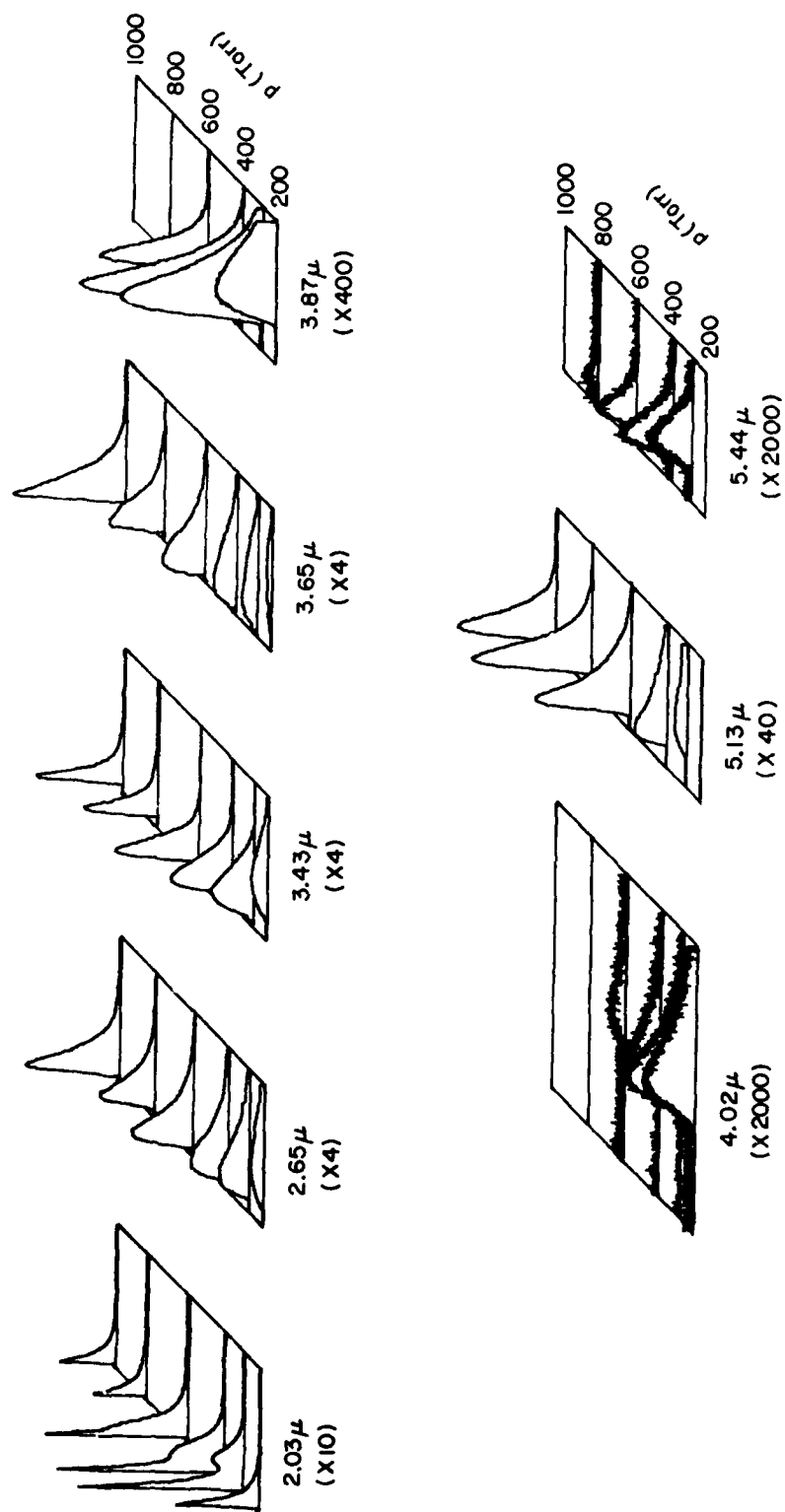
Figure 31. Laser pulses obtained for a 2000:1 He-Xe mixture at pressures from 200 to 1000 Torr. Abscissa is 0-11 μs except for 4.02 μ which is 0-22 μs.

73
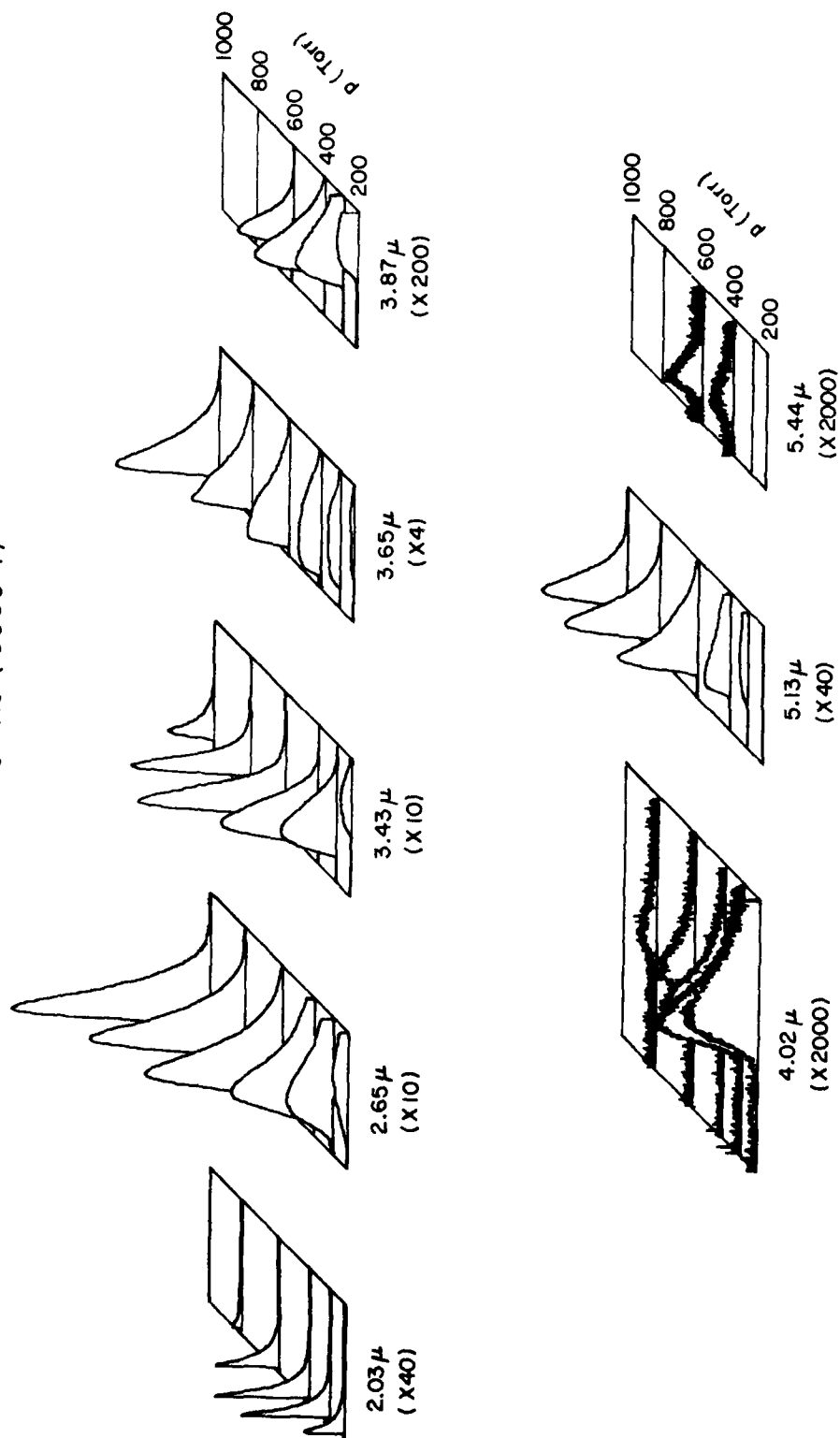
Figure 32. Laser pulses obtained for a 5000:1 He-Xe mixture at pressures from 200 to 1000 Torr. Abscissa is 0-11 μs except for 4.02 μ which is 0-22 μs.

He-Xe (10,000:1)
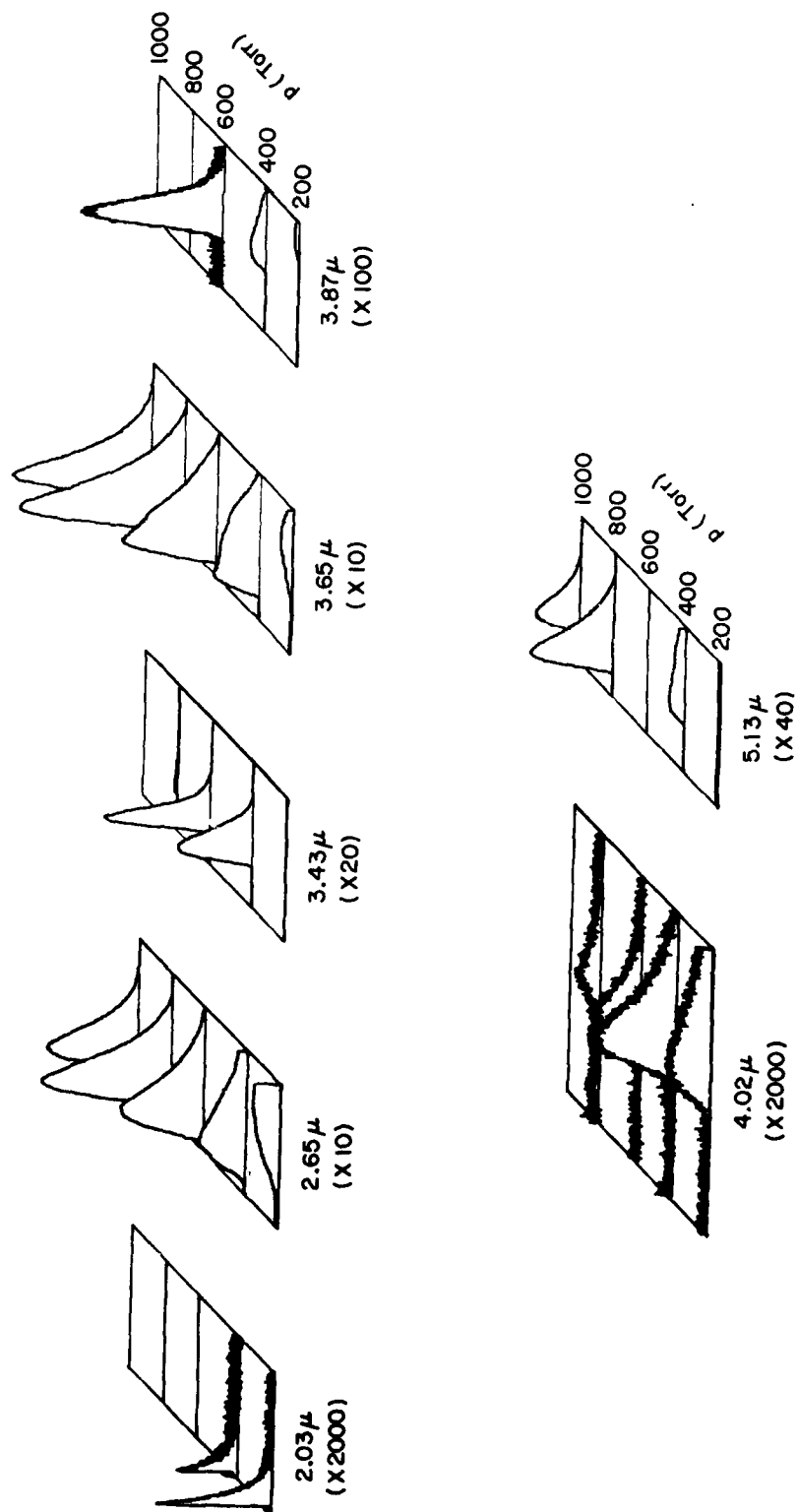
Figure 33. Laser pulses obtained for a 10,000:1 He-Xe mixture at pressures from 200 to 1000 Torr. Abscissa is 0-11 μs except for 4.02 μ which is 0-22 μs.

75
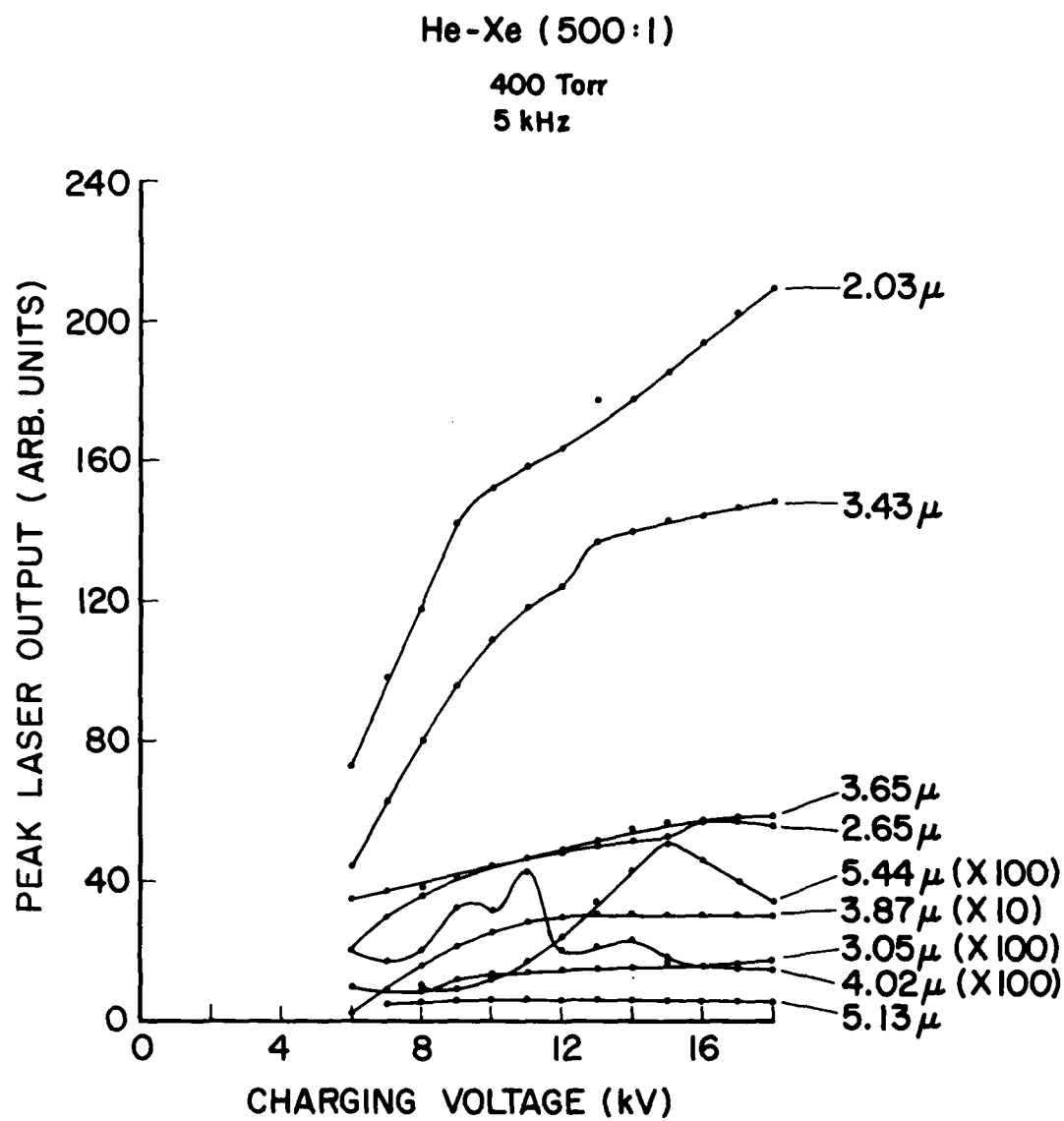
Figure 34. Dependence of peak laser output at various
wavelengths upon charging voltage.
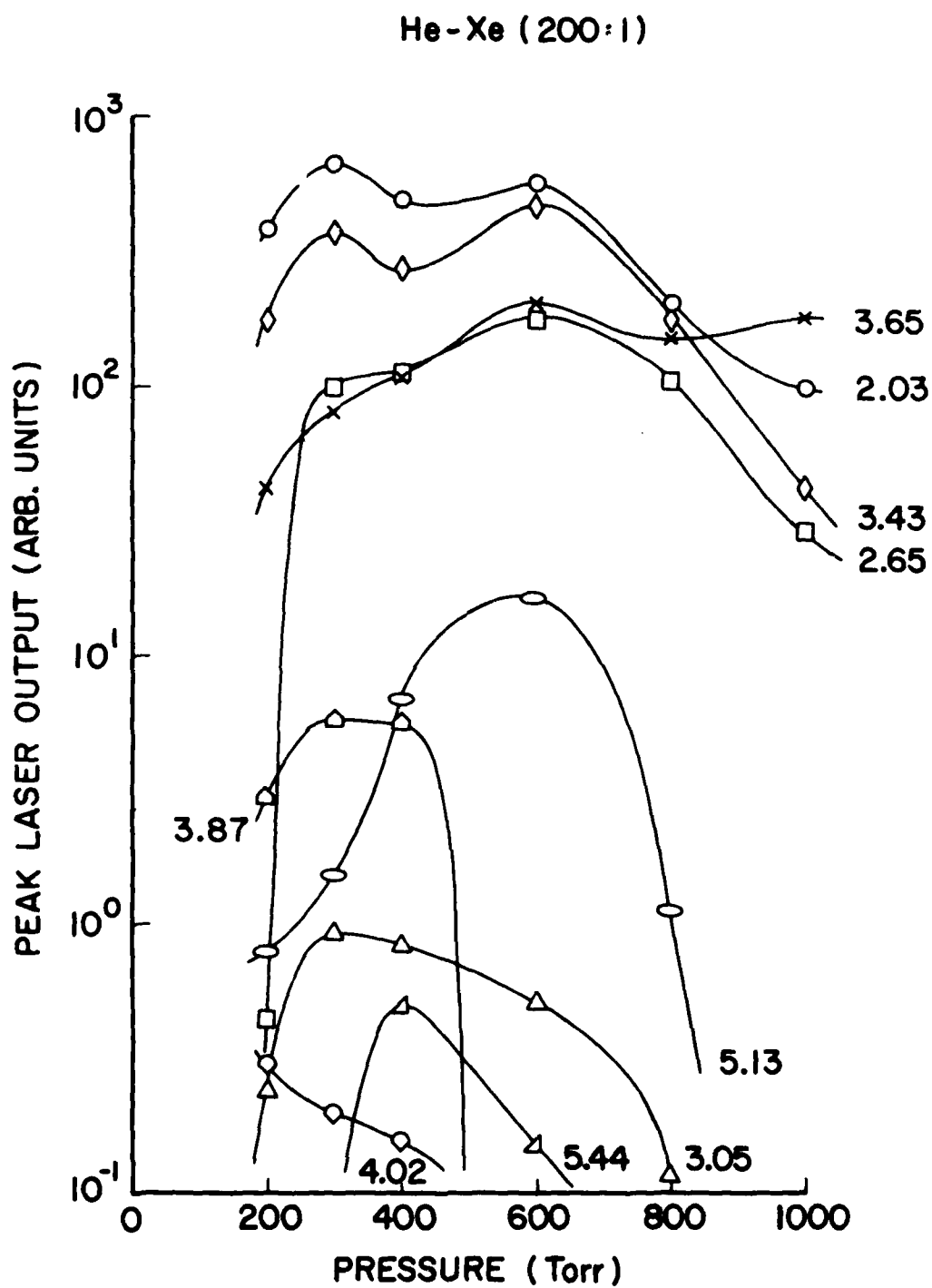
Figure 35.   Pressure dependence of peak output of laser pulses
from a 200:1 He-Xe mixture.
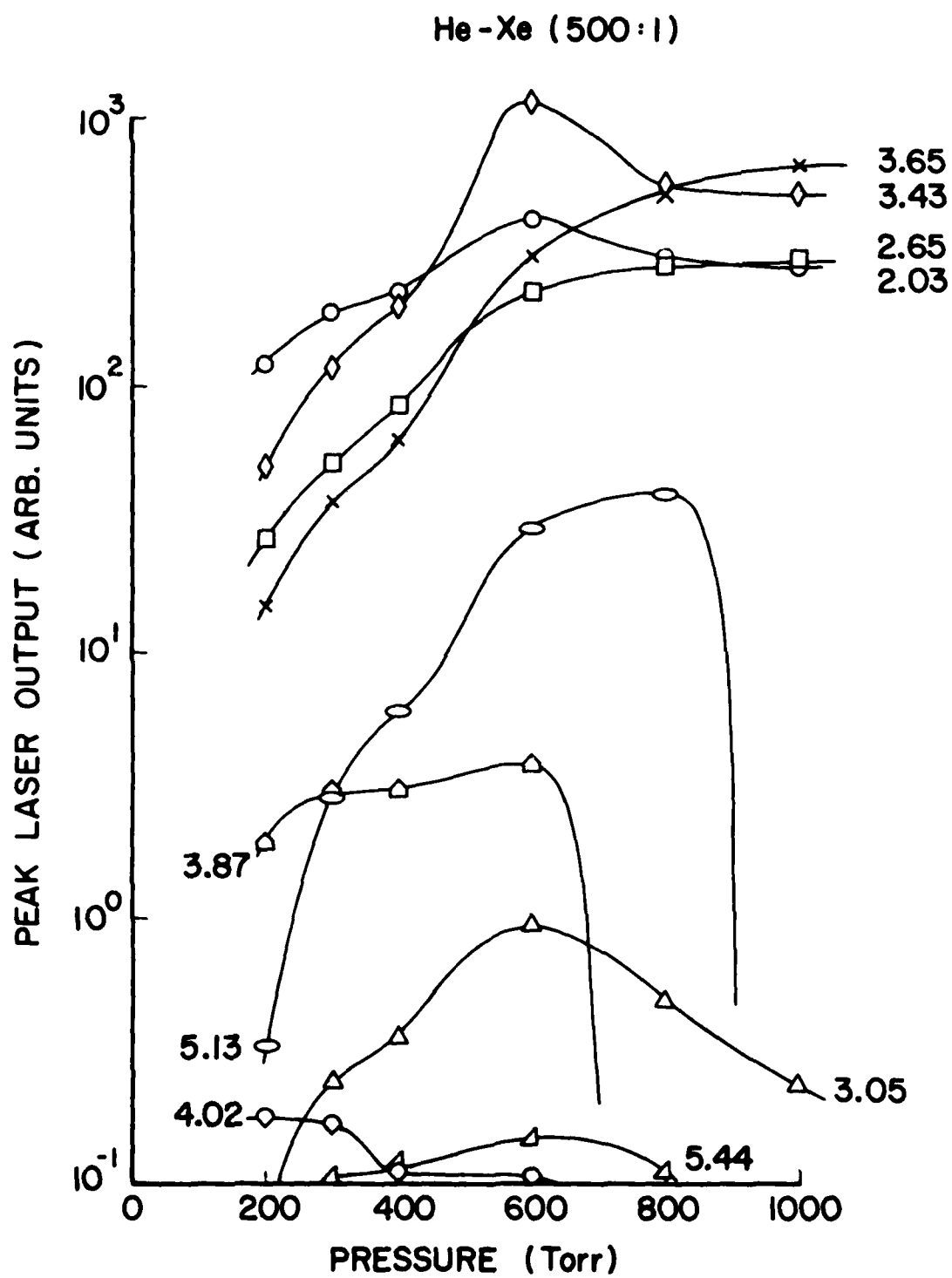
Figure 36. Pressure dependence of peak output of laser pulses from a 500:1 He-Xe mixture.
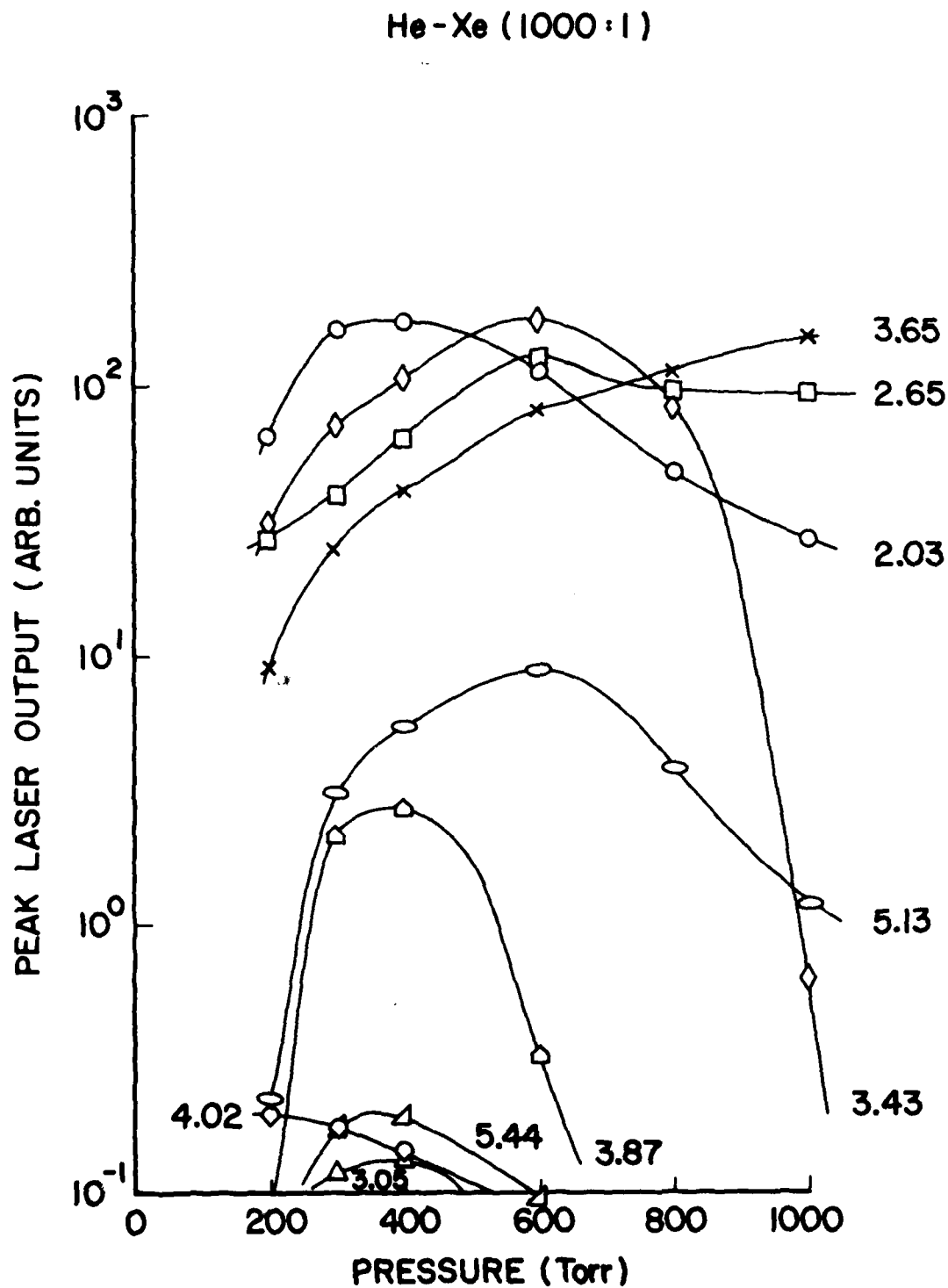
Figure 37. Pressure dependence of peak output of laser
pulses from a 1000:1 He-Xe mixture.
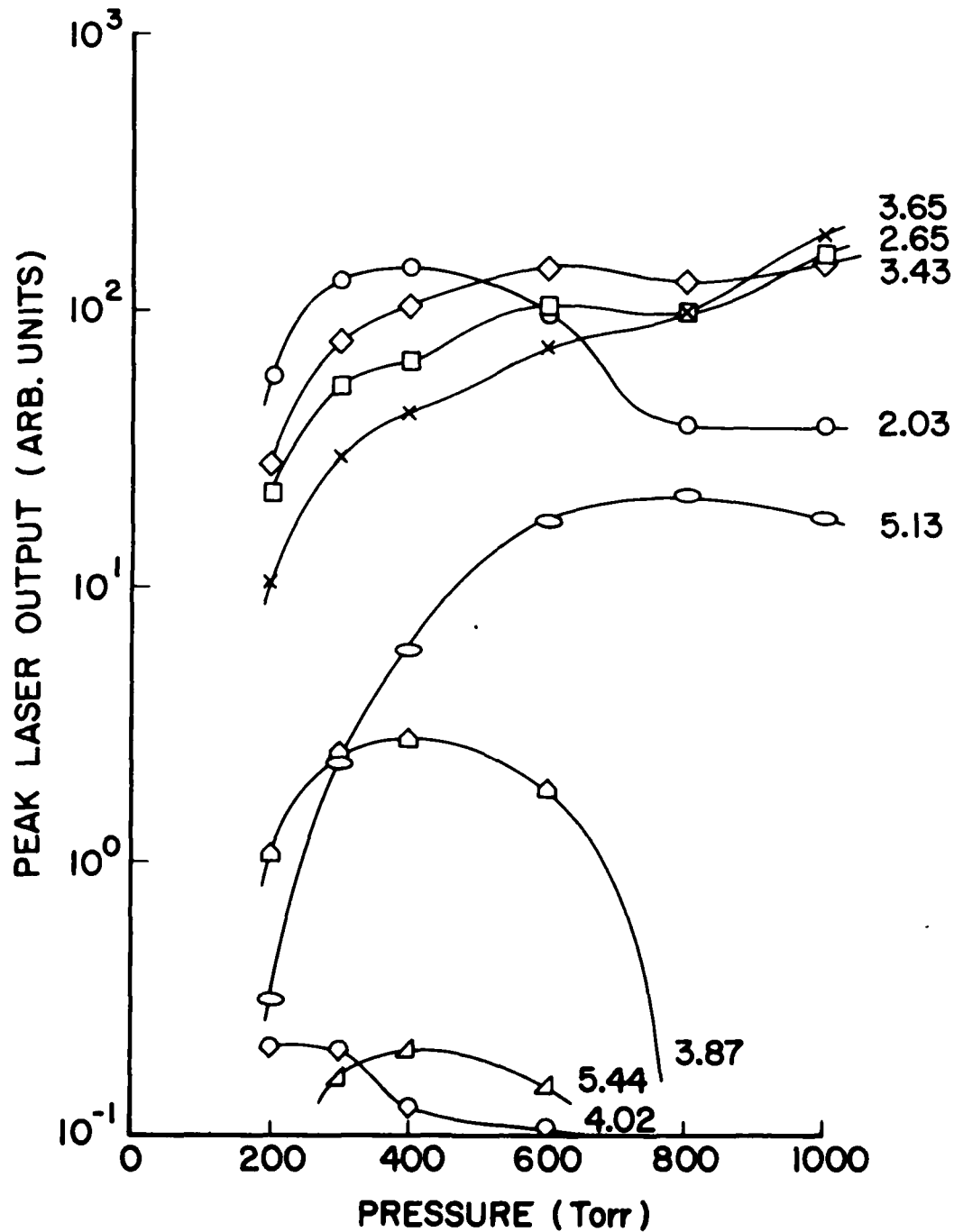
Figure 38.   Pressure dependence of peak output of laser pulses from a 2000:1 He-Xe mixture.

He - Xe (5000:1)
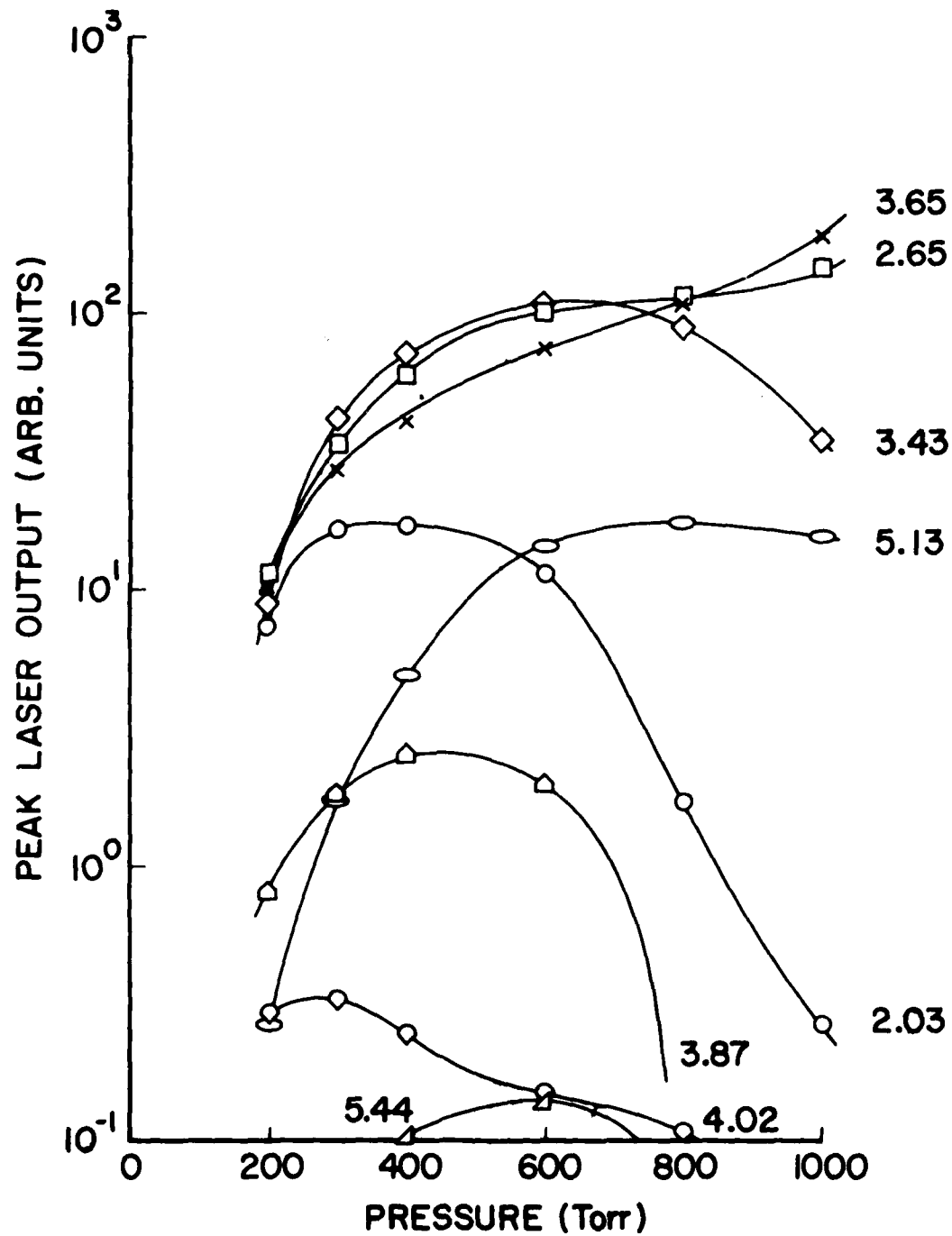
Figure 39. Pressure dependence of peak output of laser pulses from a 5000:1 He-Xe mixture.

81
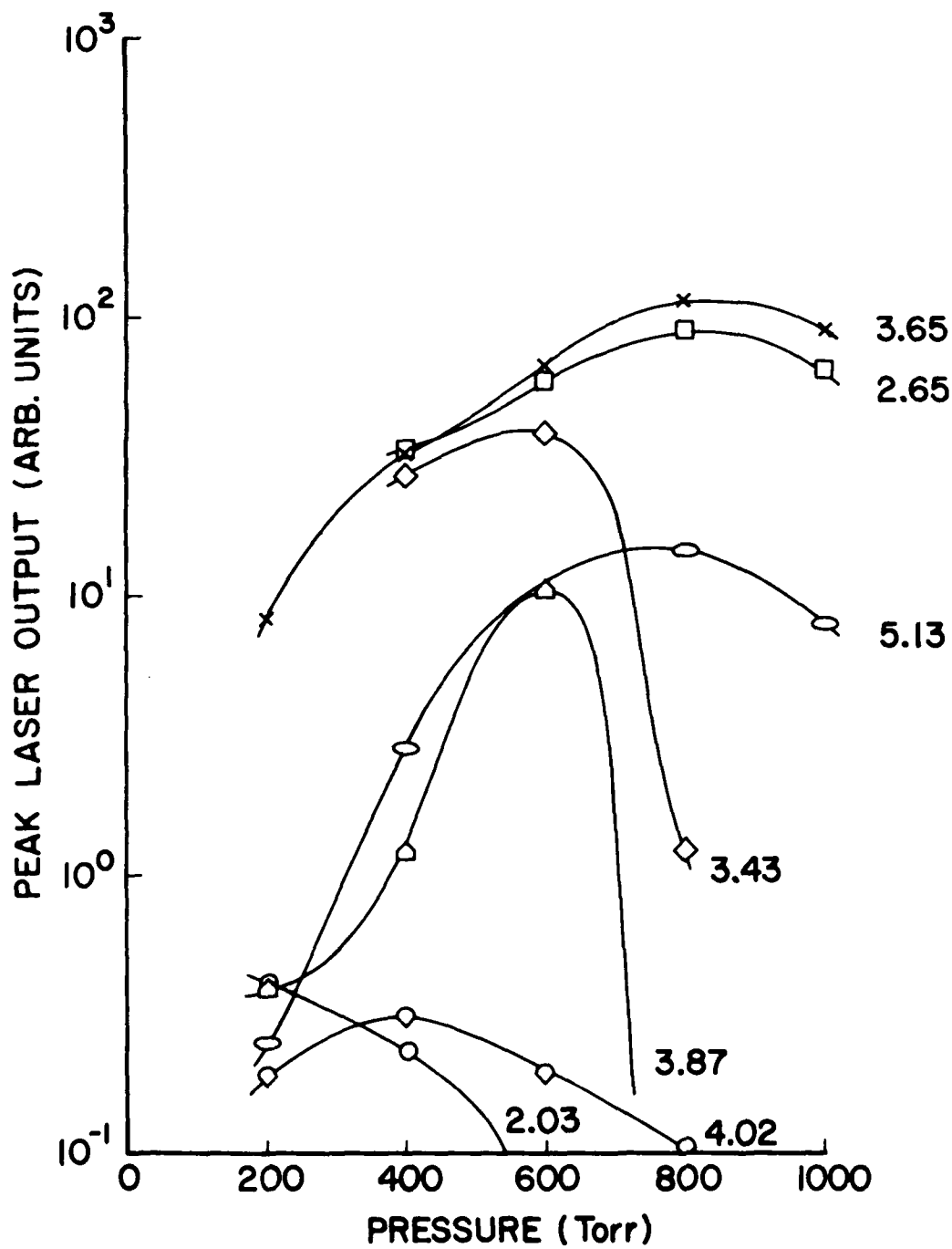
Figure 40. Pressure dependence of peak output of laser pulses from a 10,000:1 He-Xe mixture.

12 kV and a repetition rate of 5 kHz. There is considerable difference in the conditions which are favorable for the generation of the various wavelengths. For example, 2.03 and 3.43 μ tend to dominate the output at low total pressure and high Xe concentration, whereas 2.65 and 3.65 μ are the strongest pulses at high total pressure and low Xe concentration.

The dependence of the average laser output power upon charging voltage at pressures from 200 to 1000 Torr is shown in Figs. 41-46 for He-Xe mixtures with ratios from 200:1 to 10,000:1. These data were obtained at a repetition rate of 5 kHz. These data indicate that the maximum average power occurs at a mixture ratio of 500:1, a pressure of 600 Torr, and a charging voltage of 17 kV or above.

Plots of average laser output power as a function of repetition rate at pressures from 200 to 1000 Torr are shown in Figs. 47-52 for He-Xe mixtures with ratios from 200:1 to 10,000:1. These data were obtained at a charging voltage of 12 kV. Ideally, these plots should be straight lines, indicating a constant energy per pulse as the repetition rate is increased. As can be seen from the figures, none of the curves is linear over the 1-12 kHz region. The output power appears to be depressed at low repetition rates (< 6 kHz). This depression is greatest at high pressure and low Xe concentration. A clue as to the reason for this behavior can be obtained from Figs. 53 and 54 in which average laser output power is plotted as a function of fan speed. The parametric-evaluation data already presented were obtained at a fan speed of 7 on these scales. The data of Fig. 53 show that at 5 kHz, a substantial decrease in output power
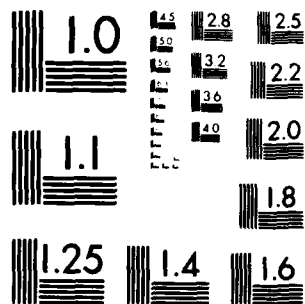
MICROCOPY RESOLUTION TEST CHART
NATIONAL BUREAU OF STANDARDS 1963 A
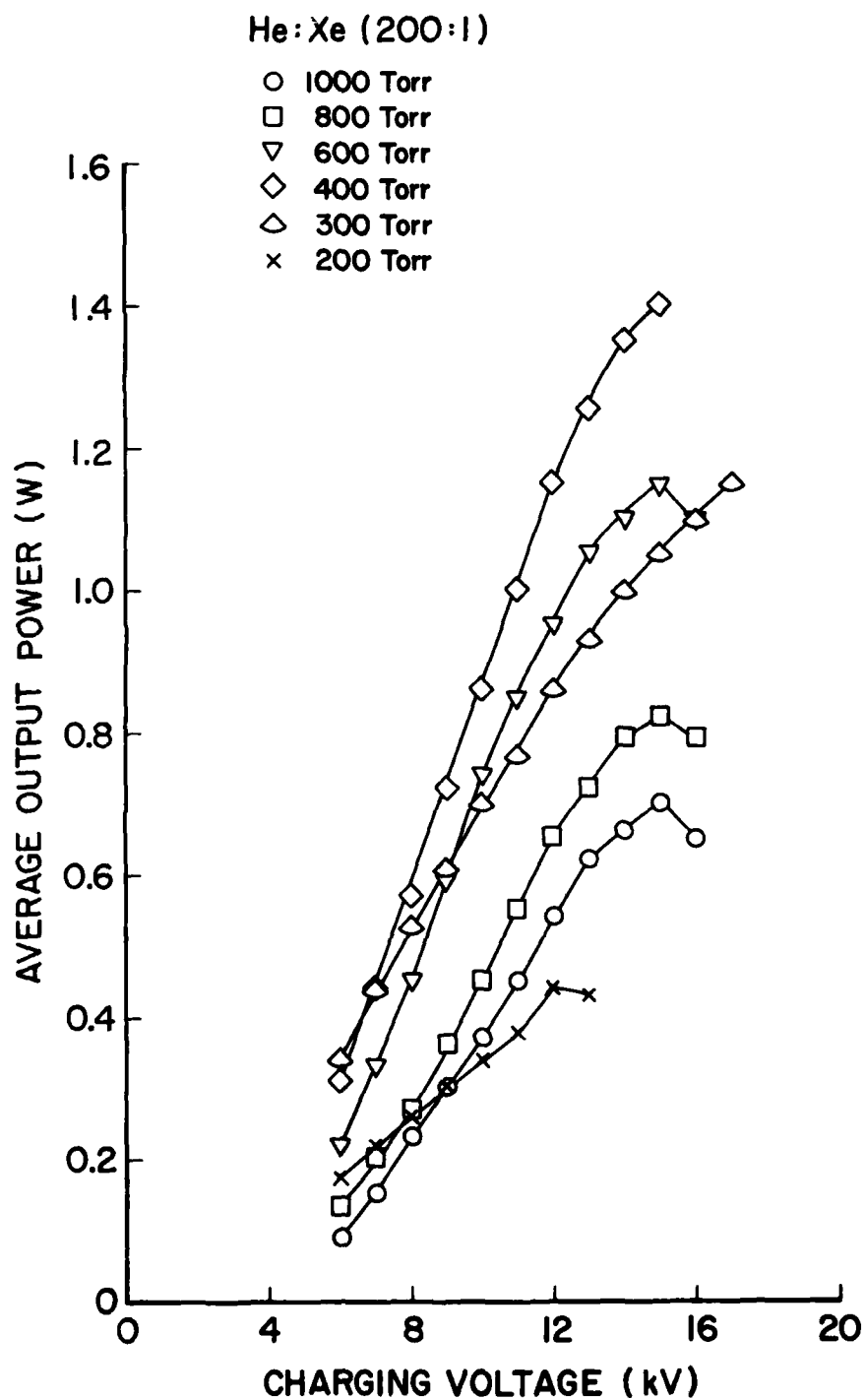
Figure 41. Dependence of average laser output power upon charging voltage for a 200:1 He-Xe mixture at pressures from 200 to 1000 Torr.
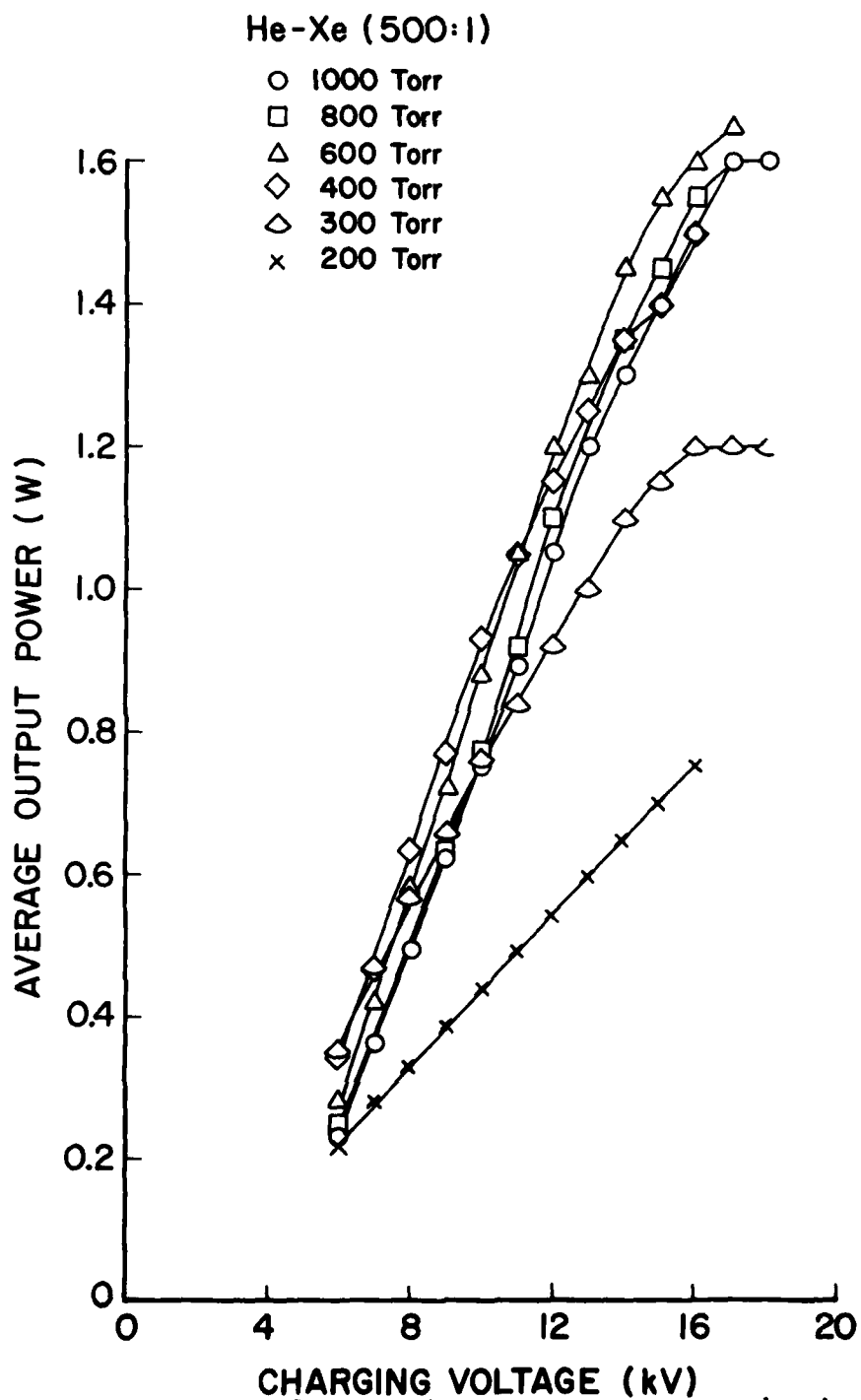
Figure 42. Dependence of average laser output power upon charging voltage for a 500:1 He-Xe mixture at pressures from 200 to 1000 Torr.

He-Xe (1000:1)

○ 1000 Torr
□ 800 Torr
◇ 600 Torr
△ 400 Torr
✕ 300 Torr
⬡ 200 Torr

Figure 43. Dependence of average laser output power upon charging
voltage for a 1000:1 He-Xe mixture at pressures from
200 to 1000 Torr.

86
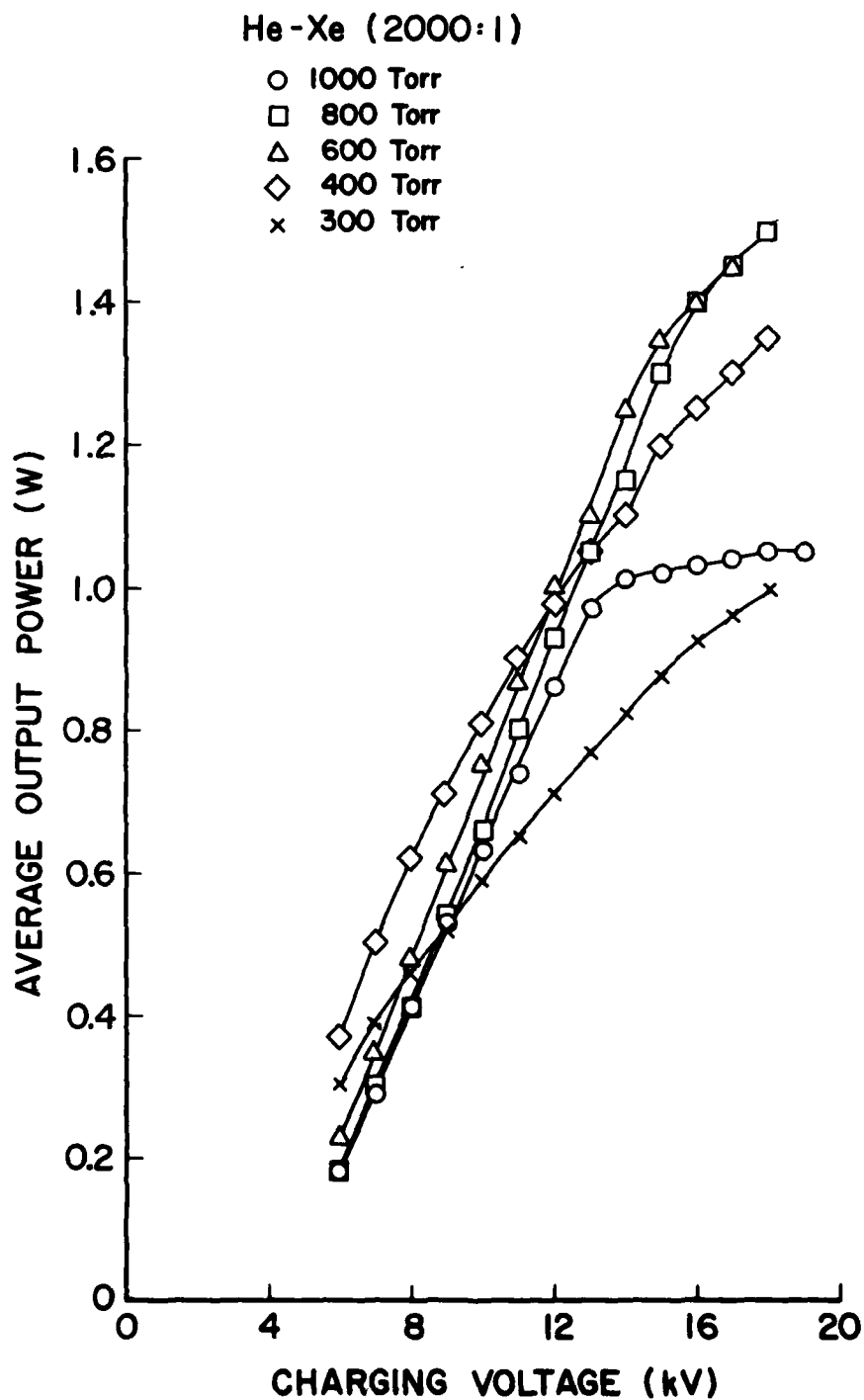
Figure 44. Dependence of average laser output power upon charging voltage for a 2000:1 He-Xe mixture at pressures from 200 to 1000 Torr.
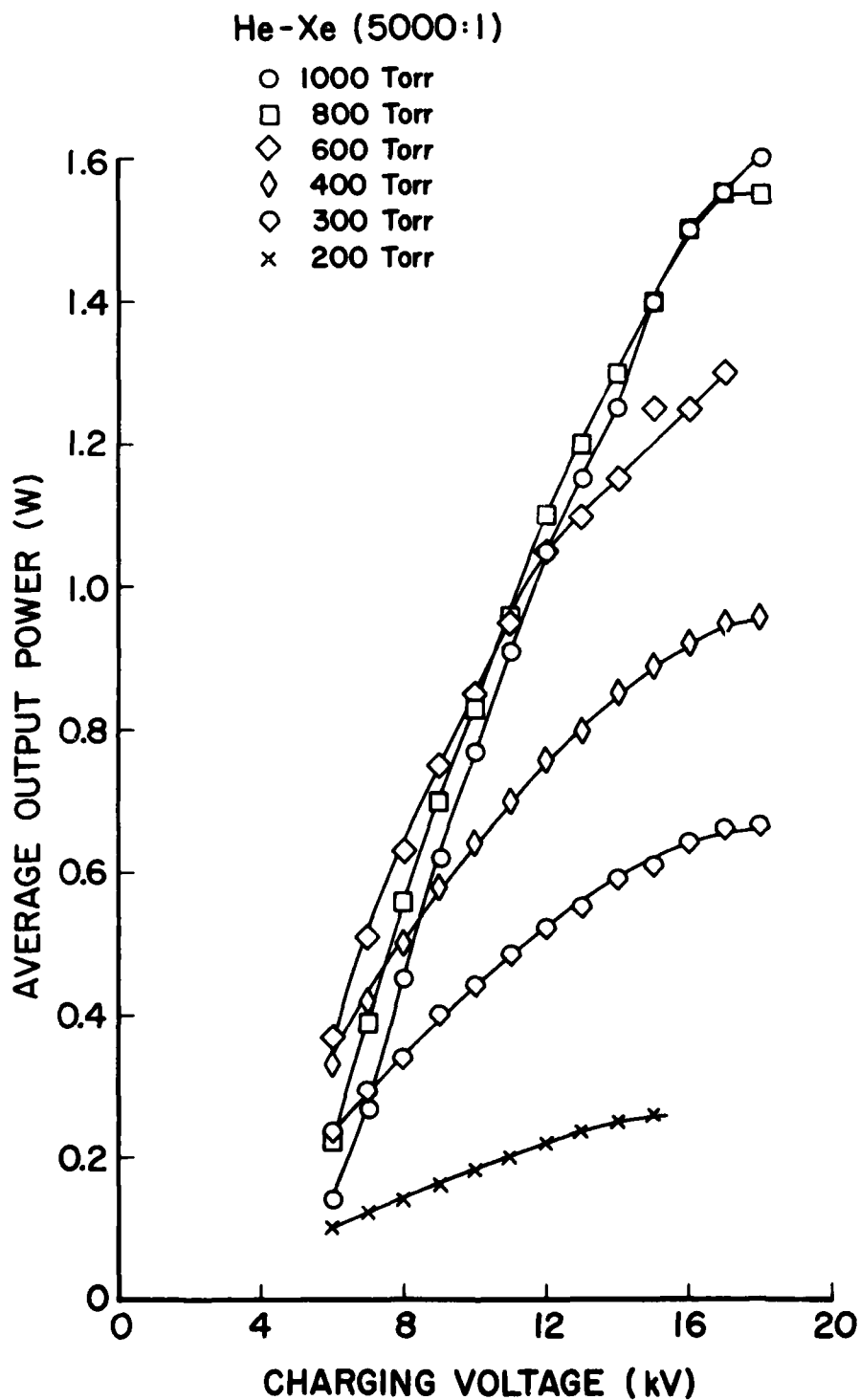
Figure 45. Dependence of average laser output power upon charging voltage for a 5000:1 He-Xe mixture at pressures from 200 to 1000 Torr.
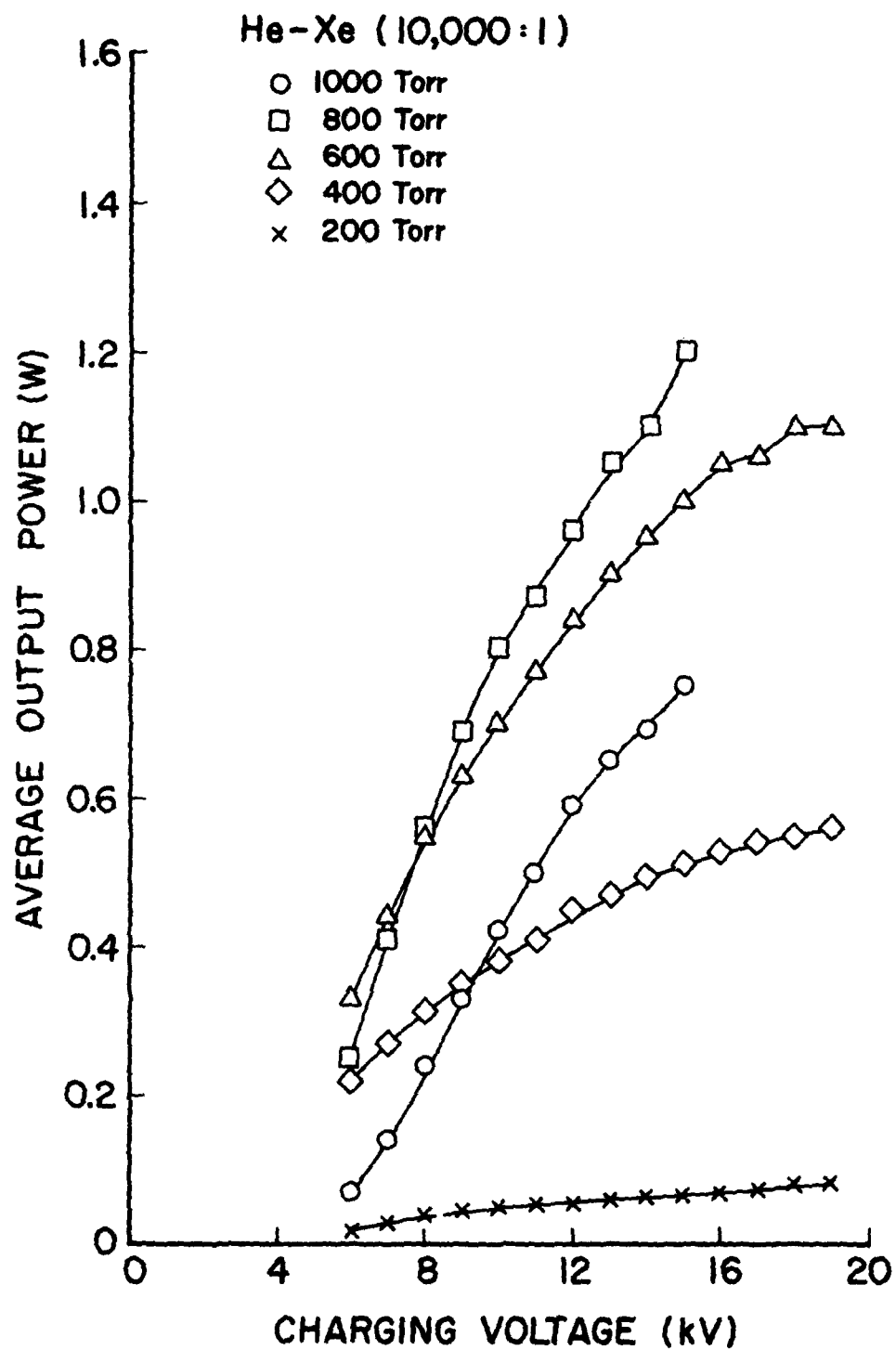
Figure 46. Dependence of average laser output power upon charging
voltage for a 10,000:1 He-Xe mixture at pressures from
200 to 1000 Torr.

89
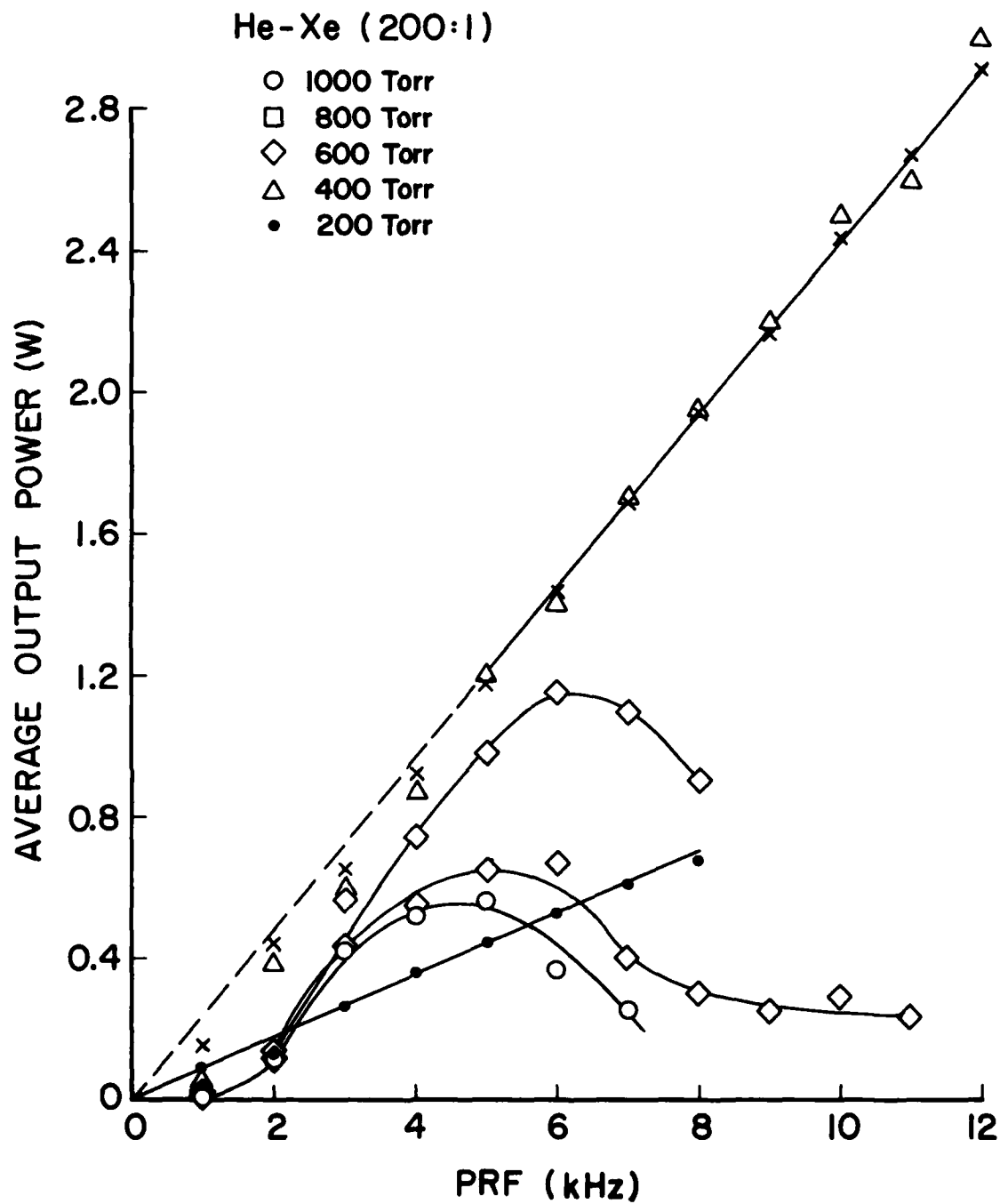
Figure 47. Dependence of average laser output power upon PRF for a 200:1 He-Xe mixture at pressures from 200 to 1000 Torr.

90
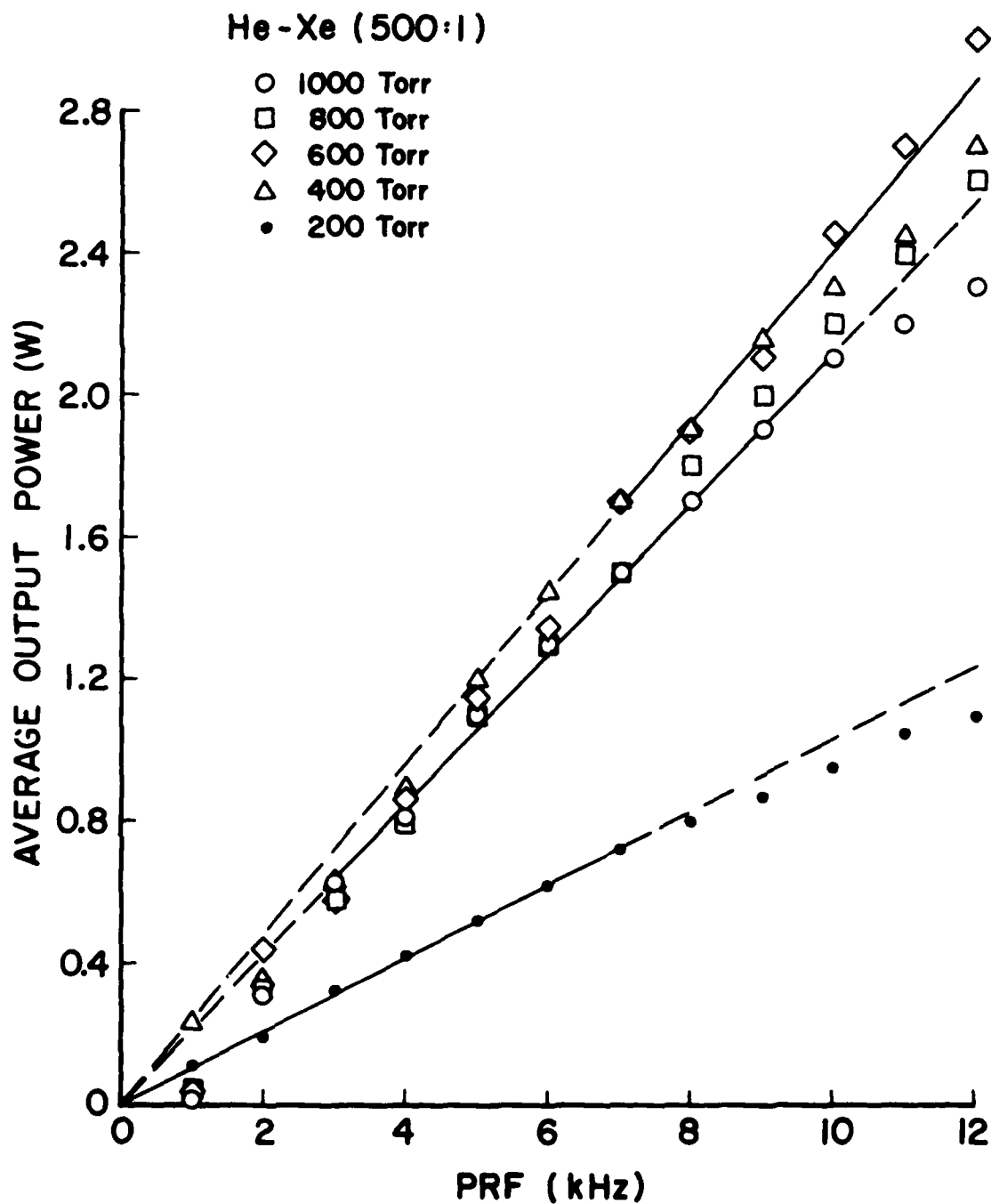
Figure 48. Dependence of average laser output power upon PRF for a 500:1 He-Xe mixture at pressures from 200 to 1000 Torr.
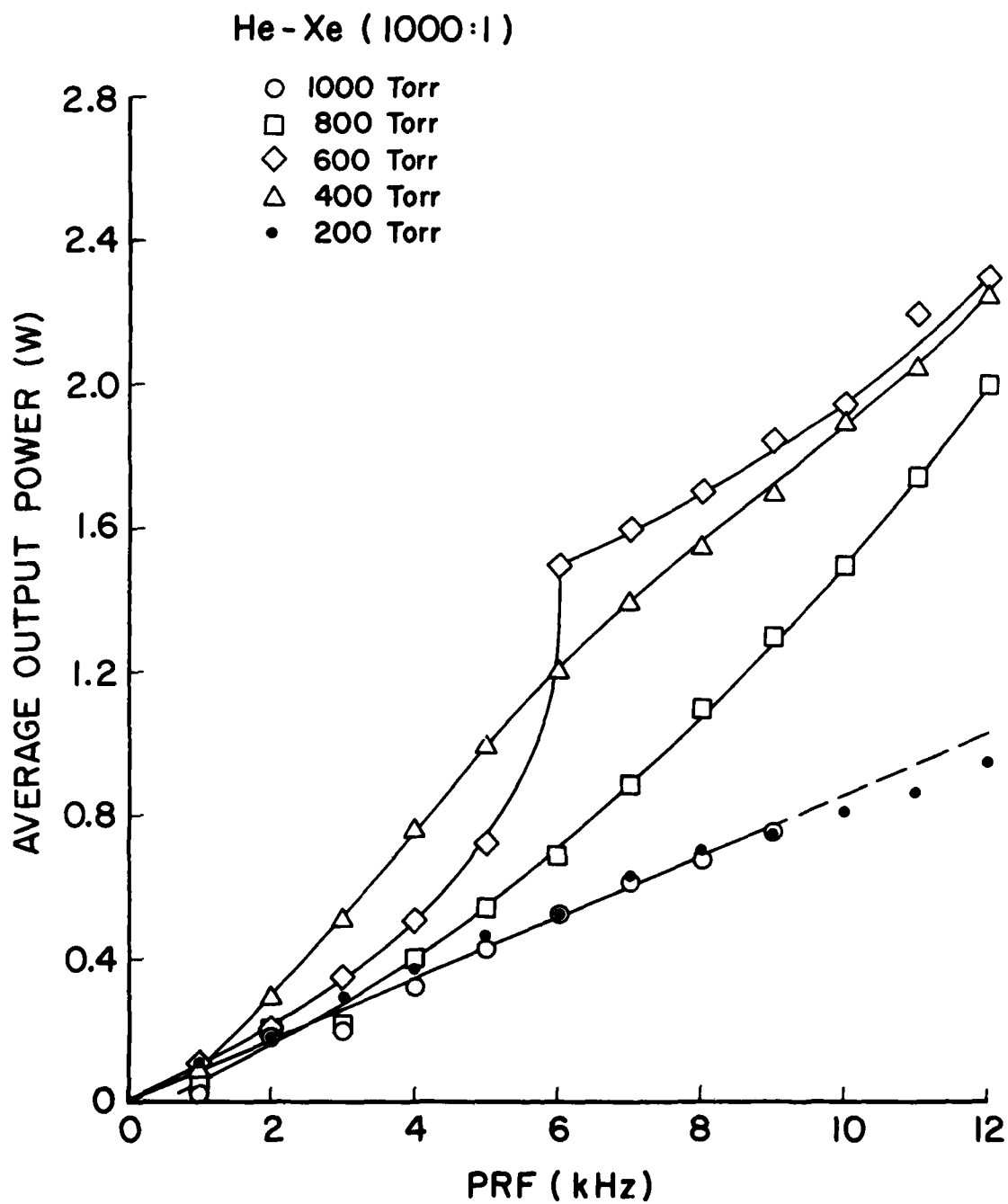
Figure 49. Dependence of average laser output power upon PRF for a 1000:1 He-Xe mixture at pressures from 200 to 1000 Torr.
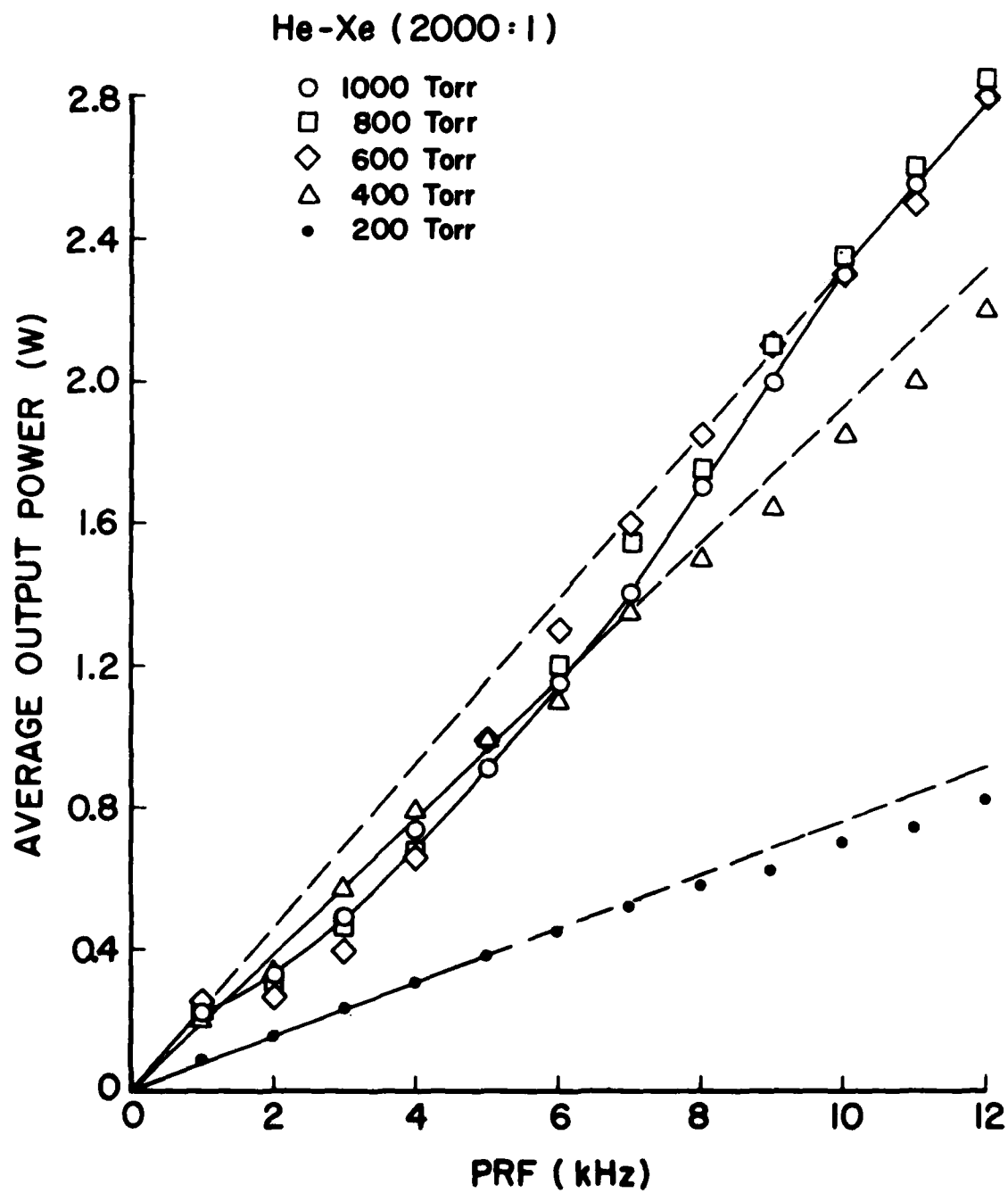
Figure 50. Dependence of average laser output power upon PRF for a
2000:1 He-Xe mixture at pressures from 200 to 1000 Torr.
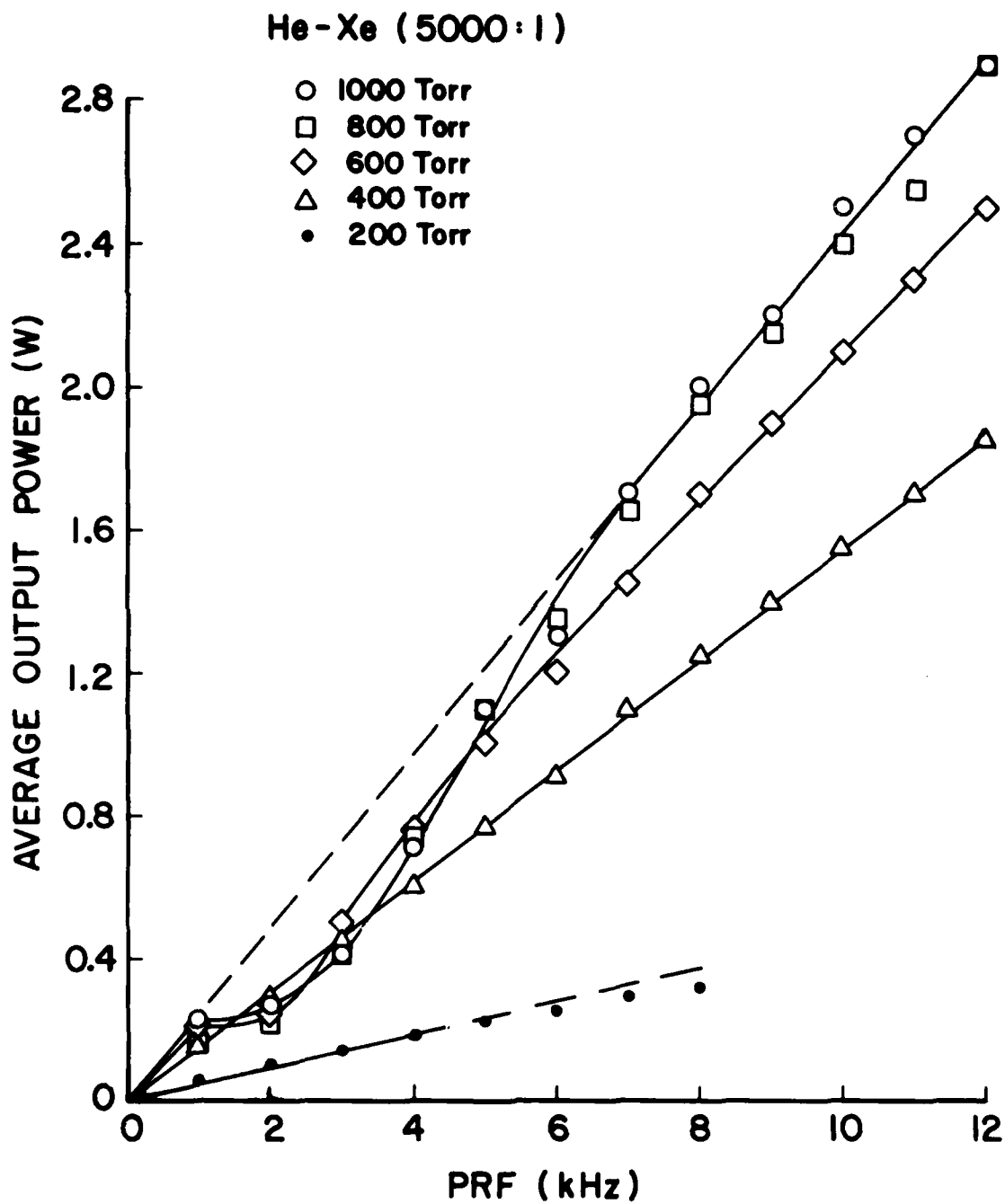
Figure 51. Dependence of average laser output power upon PRF for a 5000:1 He-Xe mixture at pressures from 200 to 1000 Torr.

He-Xe (10,000:1)

○ 1000 Torr
□ 800 Torr
◇ 600 Torr
△ 400 Torr
• 200 Torr
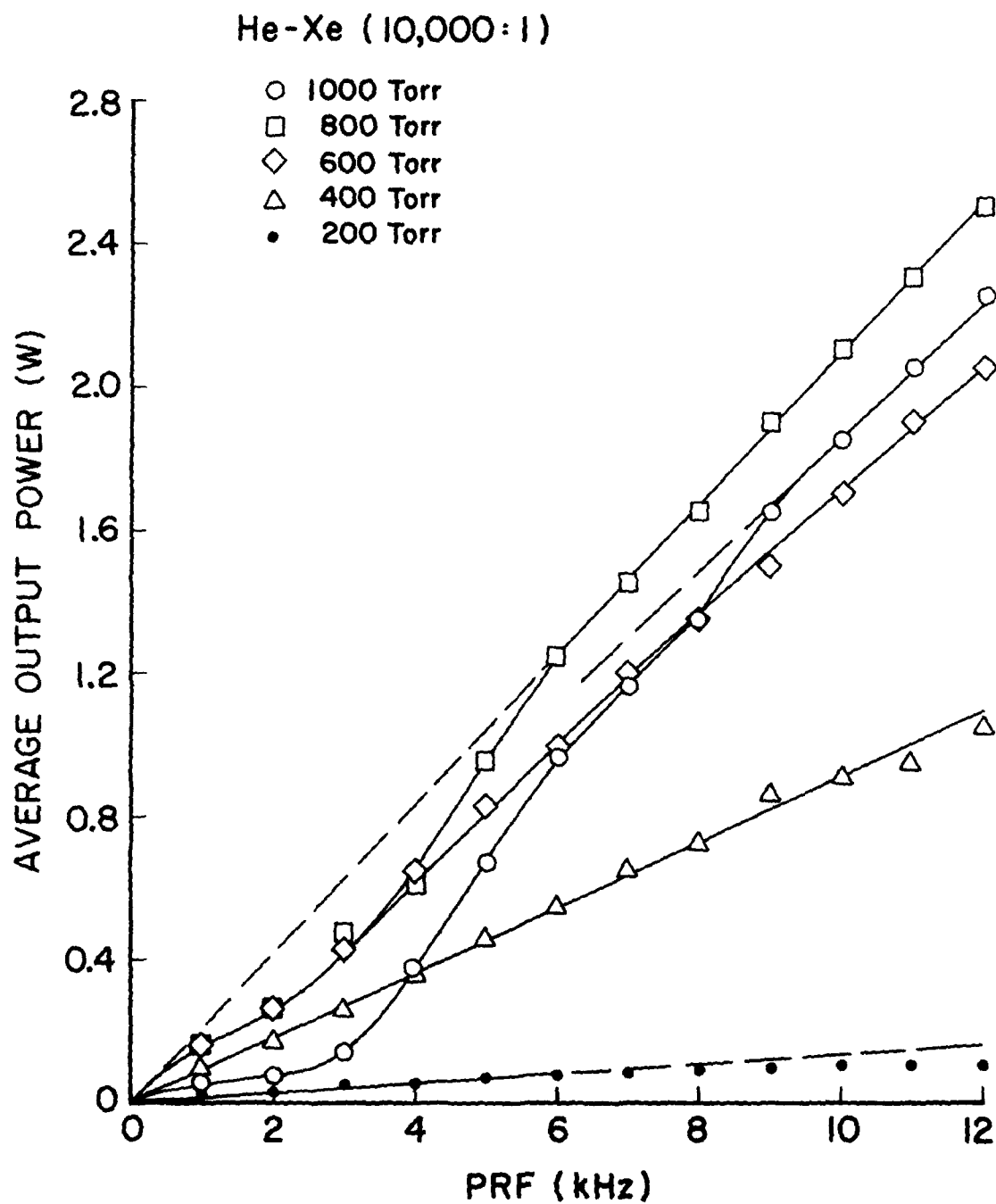
Figure 52. Dependence of average laser output power upon PRF for a 10,000:1 He-Xe mixture at pressures from 200 to 1000 Torr.

95

He - Xe (10,000:1)
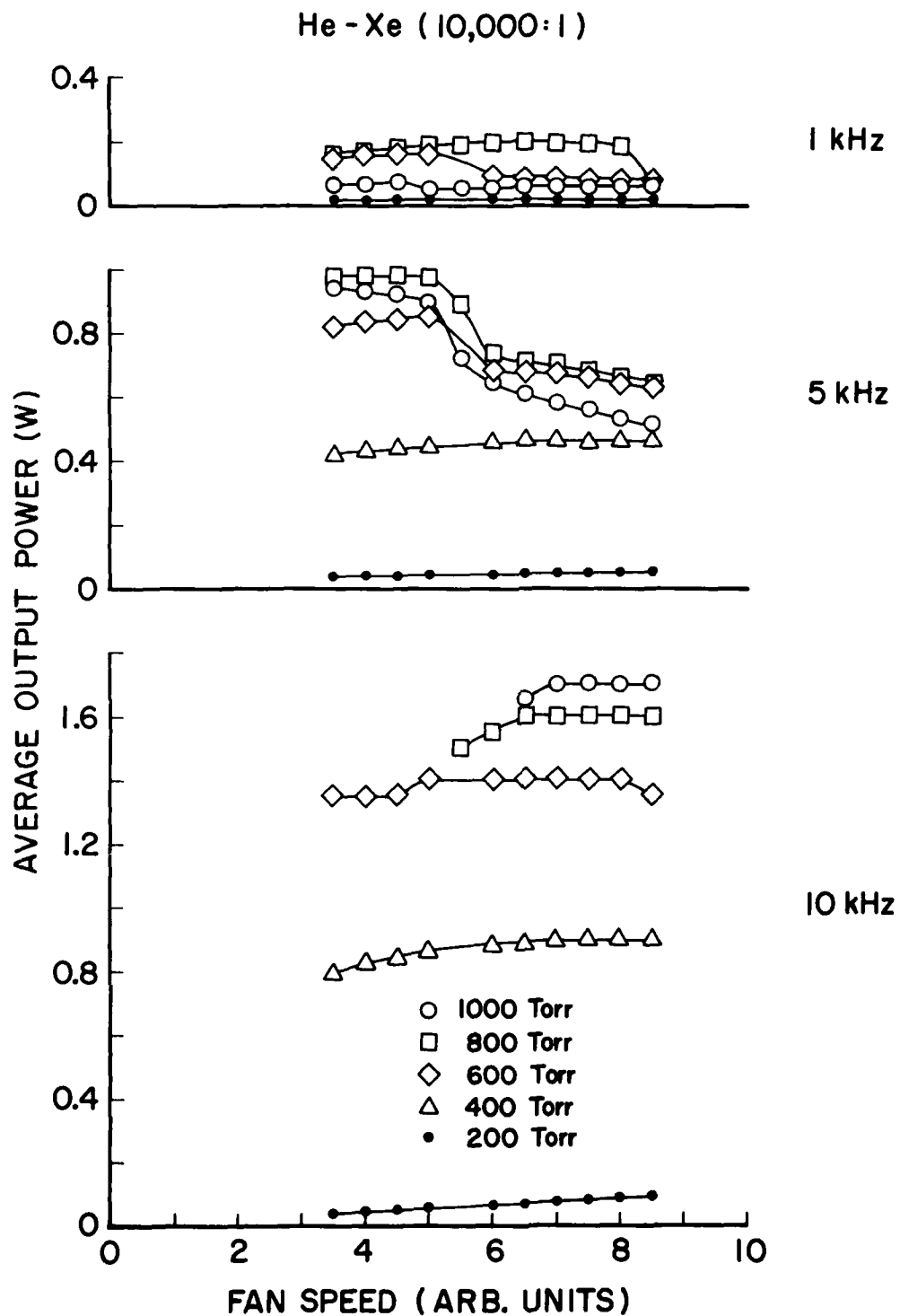
Figure 53. Dependence of average laser output power upon fan speed
for a 10,000:1 He-Xe mixture at pressures from 200 to
1000 Torr and PRF's from 1 to 10 kHz.

96
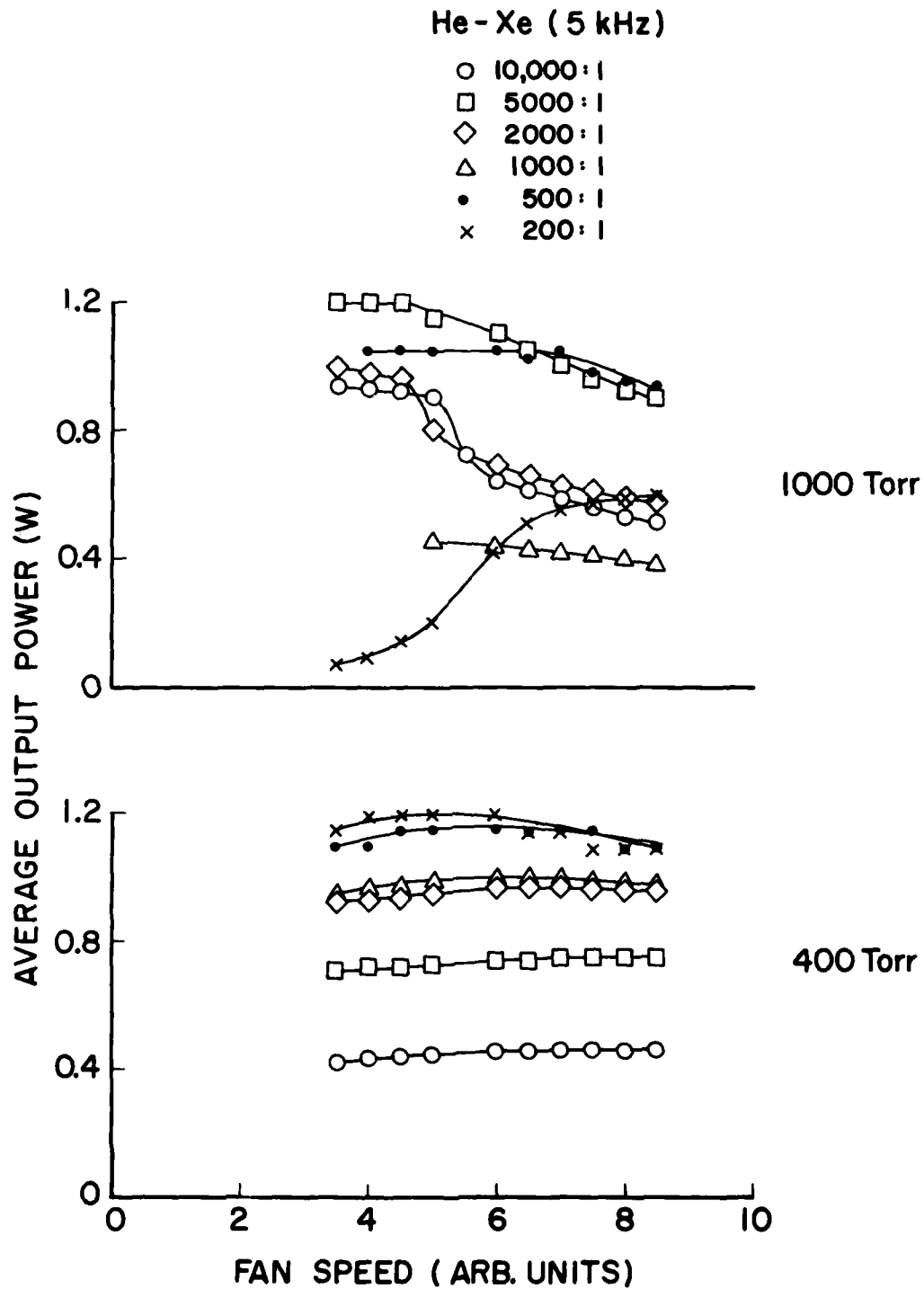
Figure 54. Dependence of average laser output power upon fan speed
for He-Xe mixtures from 200:1 to 10,000:1 at pressures
of 400 and 1000 Torr and a PRF of 5 kHz.

97

occurs--at 600-1000 Torr--as fan speed is increased beyond 5 (7300 rpm).
Similar behavior is obvious in Fig. 54 for mixture ratios greater than
1000:1 at a pressure of 1000 Torr and a repetition rate of 5 kHz. The
data of Figs. 53 and 54 demonstrate a severe depression of output power
under conditions of high pressure, low Xe concentration, high flow speed,
and low repetition rate. This behavior could indicate that a uniform
discharge is dependent upon sufficient preionization from the residual
ionization of the previous discharge pulse and that this occurs only
under certain conditions of total pressure, Xe concentration, flow
speed, and repetition rate.

The pressure dependence of the average laser output power is shown
in Fig. 55. The optimum pressure for maximum output power is in the
region 400-500 Torr. The shift to higher pressure of the output-power
maximum for the 5000:1 and 10,000:1 curves probably reflects the higher
pressure required to attain a given number of Xe atoms at the reduced
Xe concentration.

The long-lifetime performance of the laser is demonstrated by the
data of Fig. 56. The laser was operated continuously for 8 hr. at 5 kHz
$(1.4 \times 10^8$ pulses) under sealed-off conditions with no addition of make-
up gas. During this time there was no degradation of the 1-W laser out-
put power.

Following the parameter study, the laser was opened to atmosphere,
whereupon it was found that the discharge cathode had dropped about 1 mm
from its mounting plate, resulting in an interelectrode gap of 0.9 cm.
Upon disassembly of the laser, it was found that the Macor screws holding
the cathode to the Pyrex plate had fractured. One of the screws was
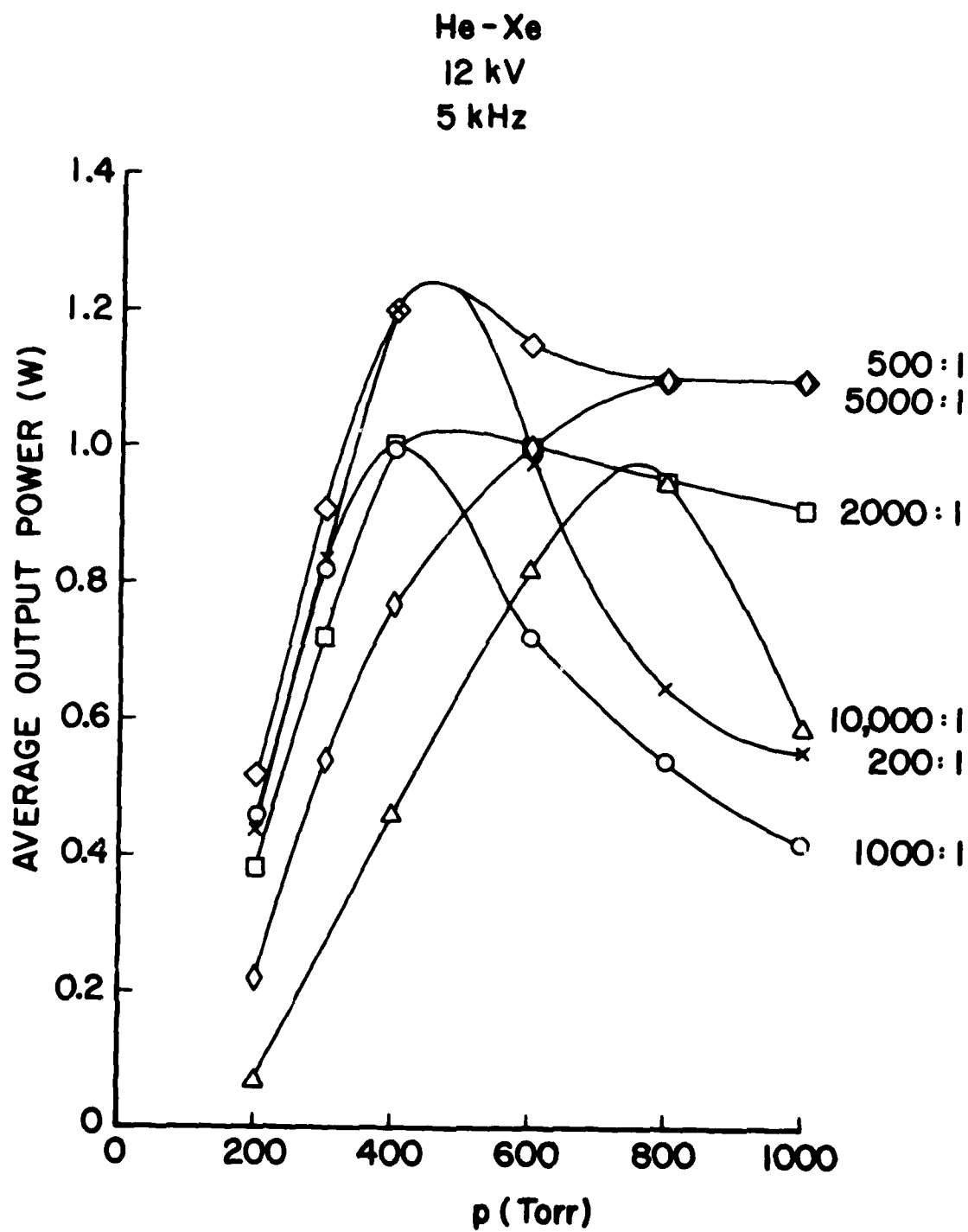
He - Xe
12 kV
5 kHz

Figure 55. Pressure dependence of average laser output power for
He-Xe mixtures from 200:1 to 10,000:1.

99
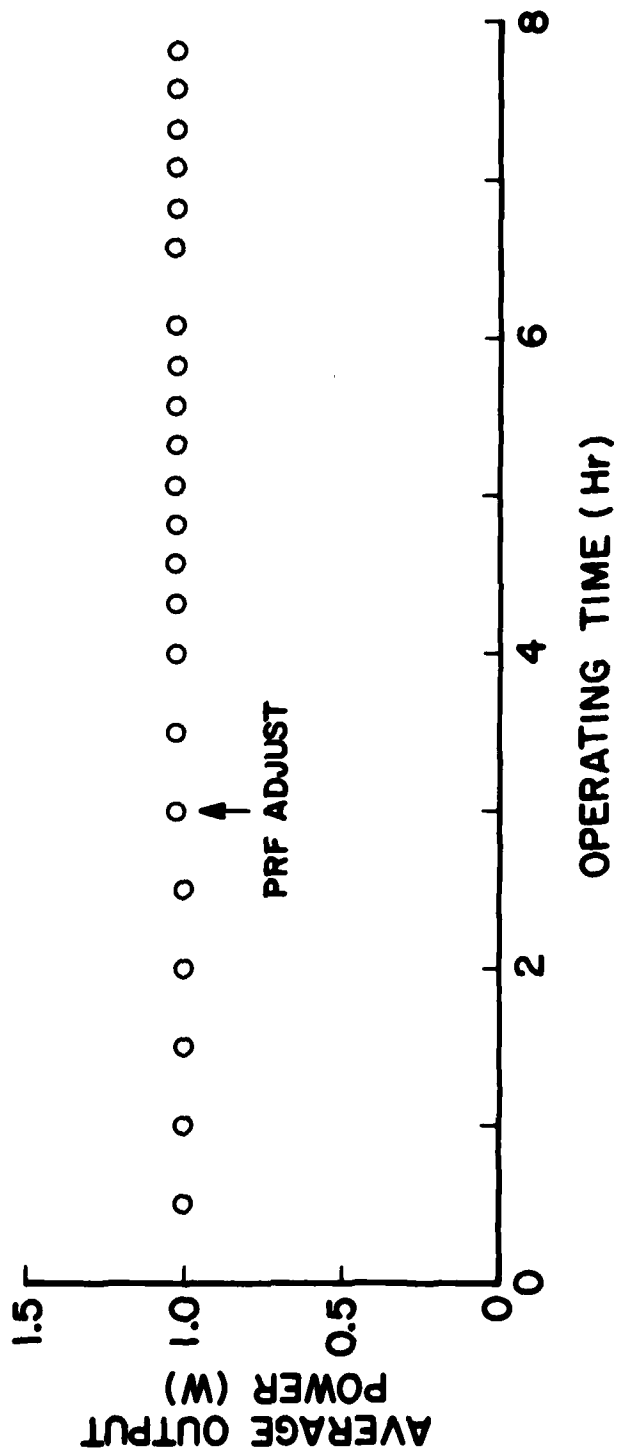
Figure 56. Dependence of average laser output power upon continuous operating time.

100

partially melted and showed other evidence of intense arcing through the vent hole in its center. Only the 200:1 He-Xe data appear to have been affected by the drop of the cathode, and these data should be viewed as inaccurate.

When the internal mirrors were removed from the laser, the reflective coatings appeared to be clouded. The transmittance of the partially transmitting flat was measured from 1600 to 5600 nm by C. DeJoseph (AFWAL/APL) using a Fourier Transform Spectrometer. The measurements are compared below with data supplied by the vendor.

λ (μ)	%T (Meas.)	%T (Vendor)
2.03	36	38
2.65	13.6	17.5
3.05	21.4	22.2
3.43	11.4	13.7
3.65	19.5	15.5
3.87	0.6	1
4.02	0.3	0.4
5.13	2.2	0.3

The change in transmittance characteristics may be the result of irradiation of the mirror by UV from the discharge.

4.5 OPERATION WITH HY-5312 THYRATRON

In order to reduce inductance in the pulser circuit and decrease voltage and current risetimes, the HY-5 thyratron was replaced by an

HY-5312 thyratron. This tube has a water-cooled anode to facilitate high-rep-rate operation and an auxiliary grid which can be used to trigger commutation. Higher di/dt is achieved when the auxiliary grid rather than the control grid is triggered. The tube also has a tightly coupled current return to minimize inductance. The thyratron enclosure was pressurized with SF_6 to ~ 5 psig to provide sufficient voltage hold-off between the thyratron and the current return. Figure 57 is a photograph of the annular-return laser with the HY-5312 in place.

Since the HY-5312 requires a gradual increase of cathode and reservoir temperature during turn-on and DC bias on both grids during operation, a heater control and bias system was constructed; a schematic of this system is shown in Fig. 58. Heater and bias potentials are controlled with variable transformers. Panel meters provide voltage and current readouts. Power to all circuits is routed through a latching relay which is tripped in the event of a thermal overload of the thyratron. The entire thyratron heater and bias system operates from a 115-V, 400-Hz input. The bias circuits are designed to provide a positive bias of up to 300 V on the auxiliary grid (grid closest to cathode) in order to maintain a distributed low-level discharge near the cathode and to provide a negative potential of up to 150 V on the control grid in order to hold off commutation. A positive-going pulse of ~ 1500 V is applied to the control grid when switch-on is desired.

The command-charging pulse-control circuitry was modified and expanded. A frequency counter and peak-reading digital panel meter were added in order that repetition rate and energy-storage-capacitor charging voltage could be displayed on the front panel of the newly

102
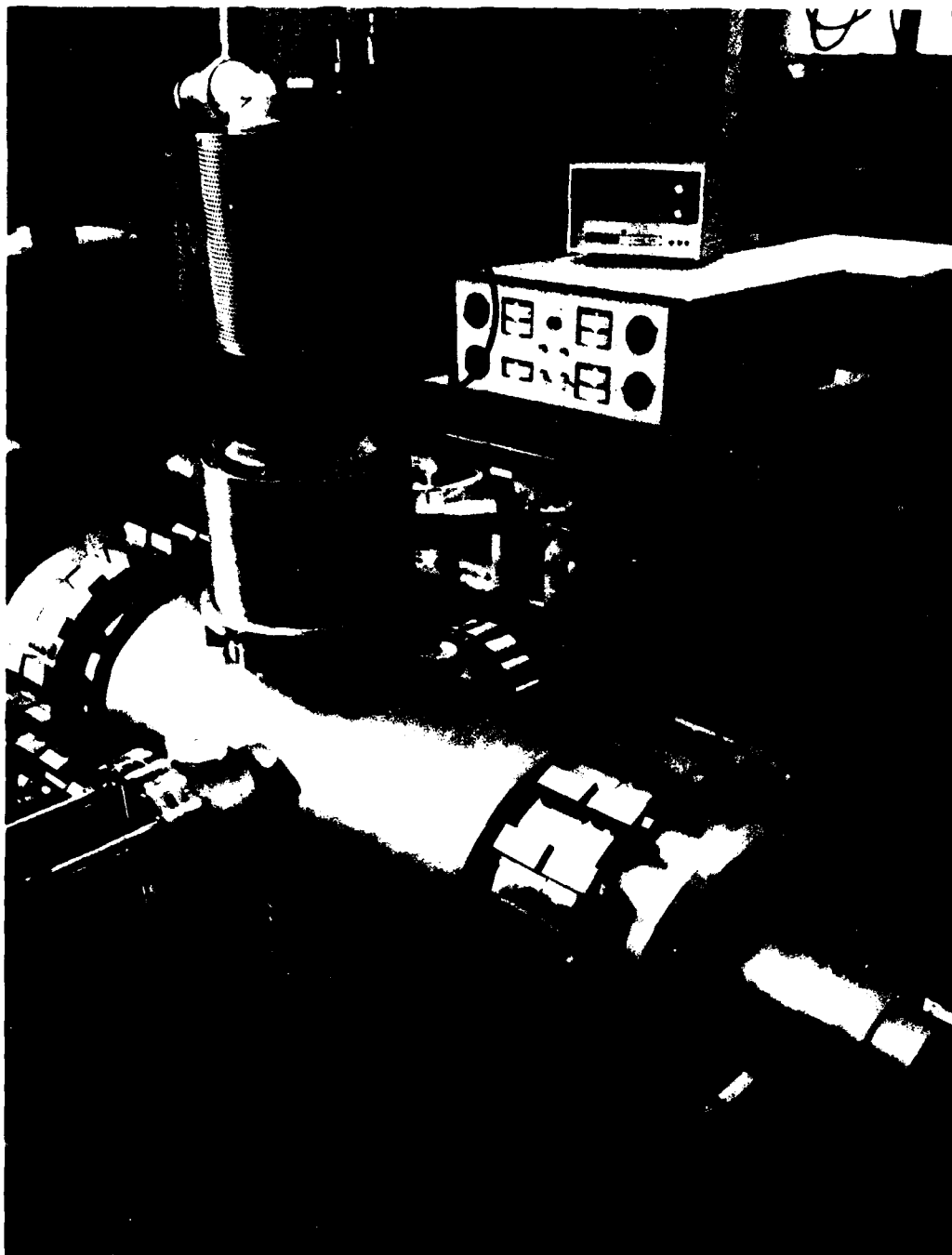
Figure 57. Photograph of closed-cycle annular-flow-return
laser.

Figure 58. Schematic diagram of HY-5312 thyratron control circuit.

104

constructed control box. Figure 59 is a schematic of the modified charge-pulse train.

Figures 60 and 61 are schematic diagrams of the f-counter and the panel meter. The resolution of the f-counter is 10 Hz, but a constant zero has been added to the readout for a display in Hertz. The digital-panel-meter integrated circuit monitors the output of a sample-and-hold module which samples the potential of the laser energy-storage capacitor for ~ 6 μsec prior to thyratron closure.

A comparison of the current and voltage pulses obtained using the HY-5 and HY-5312 is shown in Fig. 62 for a 600-Torr, 500:1 He-Xe mixture at a charging voltage of 12 kV. Although there is little difference in risetime or pulsewidth, the peak values of current and voltage achieved with the HY-5312 were greater than those achieved with the HY-5 by 8% and 35%, respectively. Average laser output power data from 1 to 12 kHz was in good agreement with data obtained previously when an HY-5 rather than an HY-5312 thyratron was used. A comparison of these data is shown in Fig. 63.

Although the presence of impurities in a He-Xe laser discharge has been assumed to be detrimental to laser performance, experimental confirmation of this assumption was lacking. In order to investigate the effect of impurities upon He-Xe laser output, 1 Torr of H_2 was added to 600 Torr of He-Xe (500:1). This increased the laser output from 0.39 to 0.4 W at a repetition rate of 2 kHz and a charging voltage of 12 kV. The addition of 5 Torr of H_2 initially increased the laser output to 0.42 W, but then the output decreased with time as shown in Fig. 64. About two hours after these data were taken, the laser was restarted, and
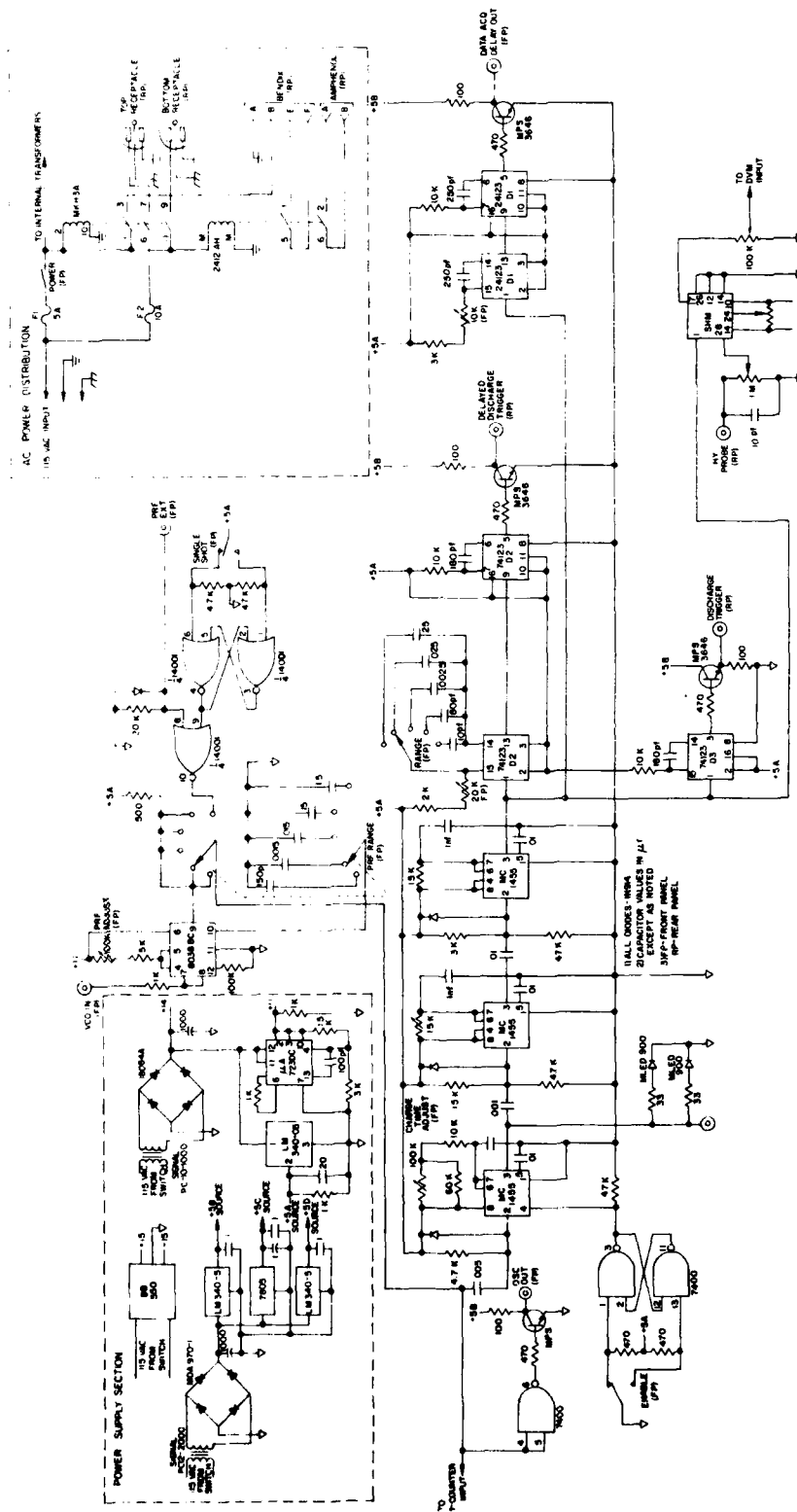
Figure 59. Schematic diagram of command-charging control circuit.
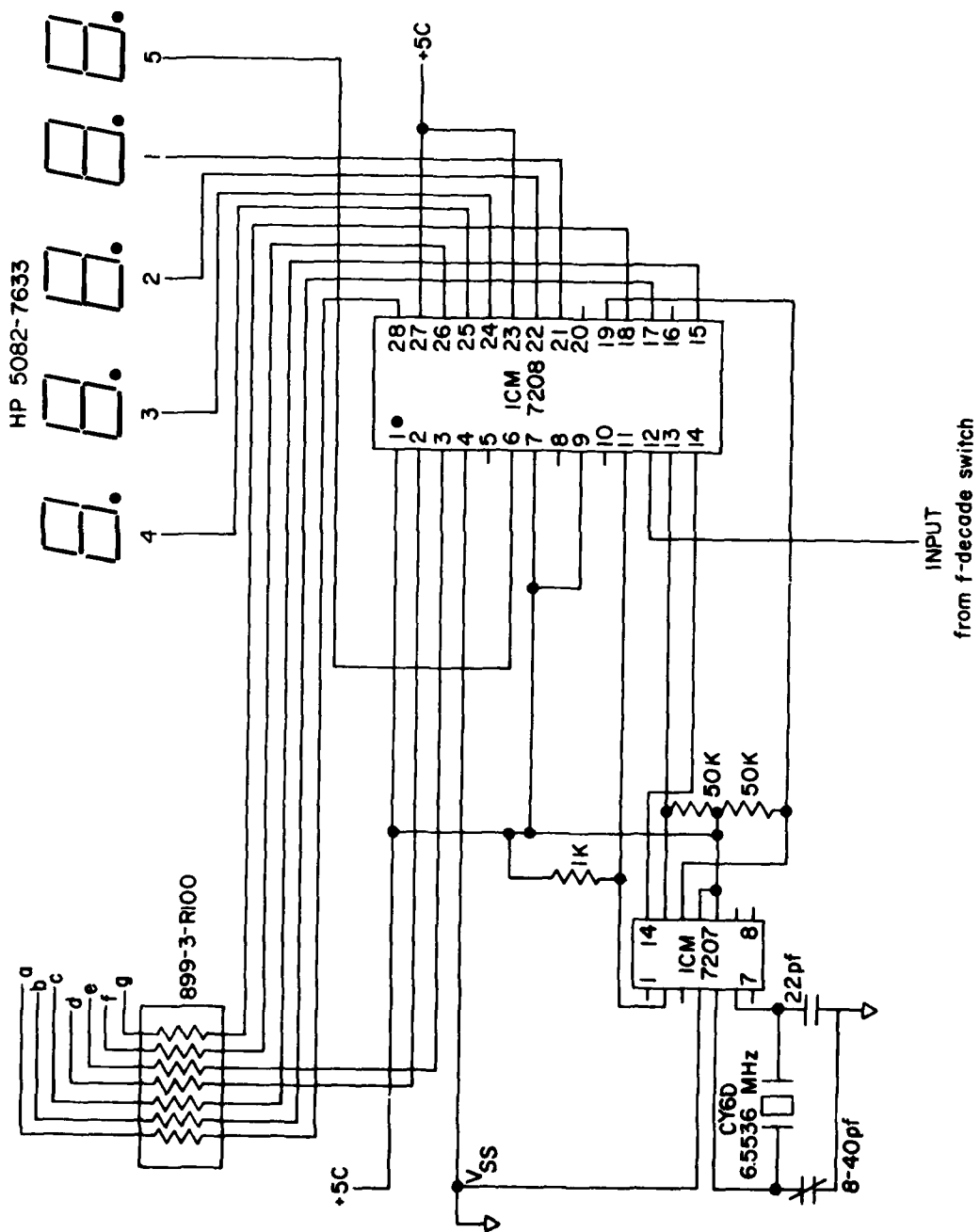
Figure 60. Schematic diagram of frequency counter.

Figure 61. Schematic diagram of peak-reading digital panel meter.

600 TORR, 500 : I He-Xe
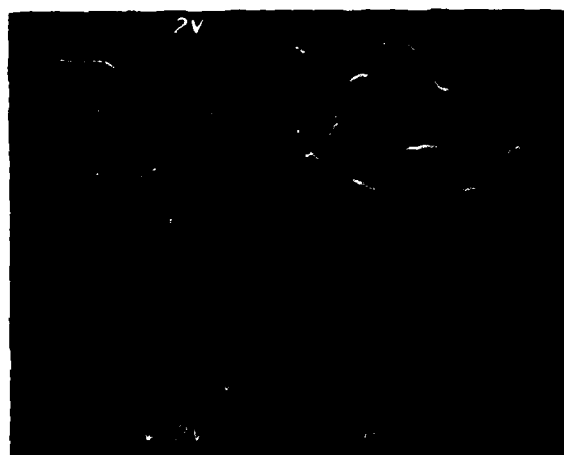
VOLTAGE (2 kV/ DIV)

CURRENT (400 A/DIV)

(a)
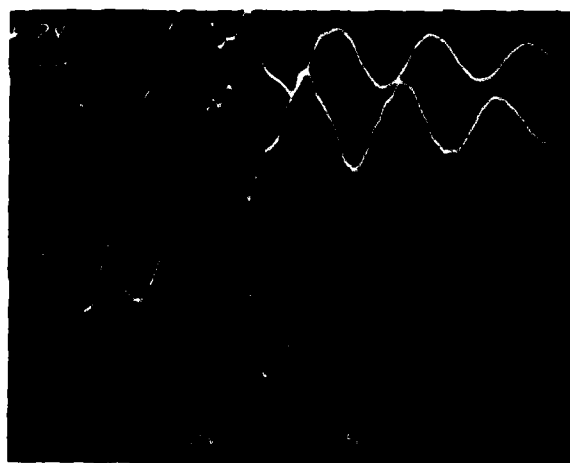
CURRENT (400 A/DIV)

VOLTAGE (2 kV/DIV)

(b)

Figure 62. Oscillograms of discharge current and voltage pulses
using (a) HY-5 and (b) HY-5312 thyratrons.
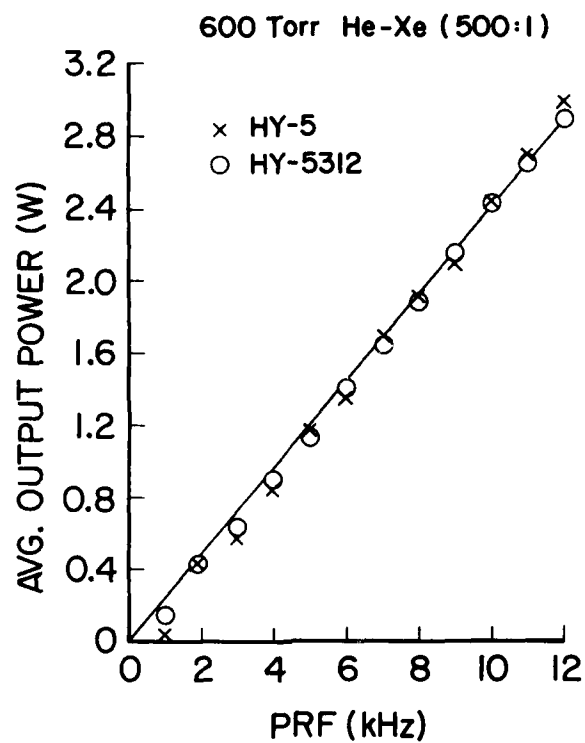
600 Torr He-Xe (500:1)

Figure 63.   Comparison of He-Xe laser outputs obtained
using HY-5 and HY-5312 thyratrons.
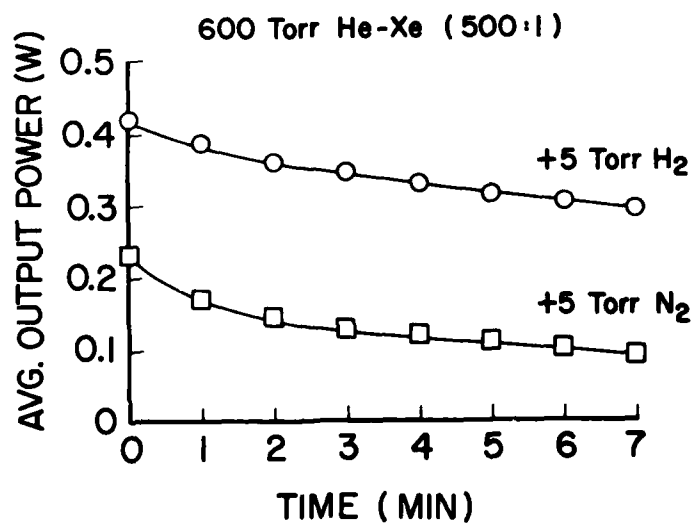
600 Torr He-Xe (500:1)

Figure 64.   Effect of H_2 and N_2 additives upon He-Xe laser
output power.

the laser output power was 0.06 W. The addition of 1 Torr of N_2 to 600 Torr He-Xe (500:1) did not change the 0.43-W output. The addition of 5 Torr of N_2, however, immediately reduced the output to 0.23 W, which decreased further with time as seen in Fig. 64. A more thorough study is required to determine quantitatively the effect of various impurities upon laser output.

High-pressure pulsed laser action in the rare gases has been reported by Wood, et al.,[51] and Chapovsky, et al.,[52] for single-shot or low-repetition-rate (3-Hz) operation. This motivated a brief investigation of the high-repetition-rate laser performance of various rare-gas mixtures in the AFRL. Lasing was achieved in He-Ar mixtures at 1.79, 2.2, and 2.4 μ and in He-Kr mixtures at 1.78, 2.19, 2.52, and 3.06 μ. Plots of the average laser output power as a function of the amount of Ar or Kr added to 1000 Torr of He are shown in Fig. 65. The data were obtained at a repetition rate of 10 kHz and a charging voltage of 12 kV for He-Ar and 10 kV for He-Kr. Higher output power is to be expected at higher voltage and total pressure. For example, in Ref. 52 a peak power of 200 kW was achieved at 1.79 μ for a 5-atm. He-Ar mixture and a charging voltage of 35 kV.

Uniform glow discharges in high-pressure Ar-Xe mixtures were achieved over a limited range of pressure, repetition rate, and charging voltage using a 5-nF capacitor switched by the HY-5312 thyratron. This indicates improved pulser performance with the use of the HY-5312 rather than an HY-5 thyratron, since uniform discharges could not be attained with an HY-5 switched 5-nF capacitor. Lasing was achieved in Ar-Xe mixtures at 1.73, 2.03, 2.63,

1000 Torr He
PRF = 10 kHz
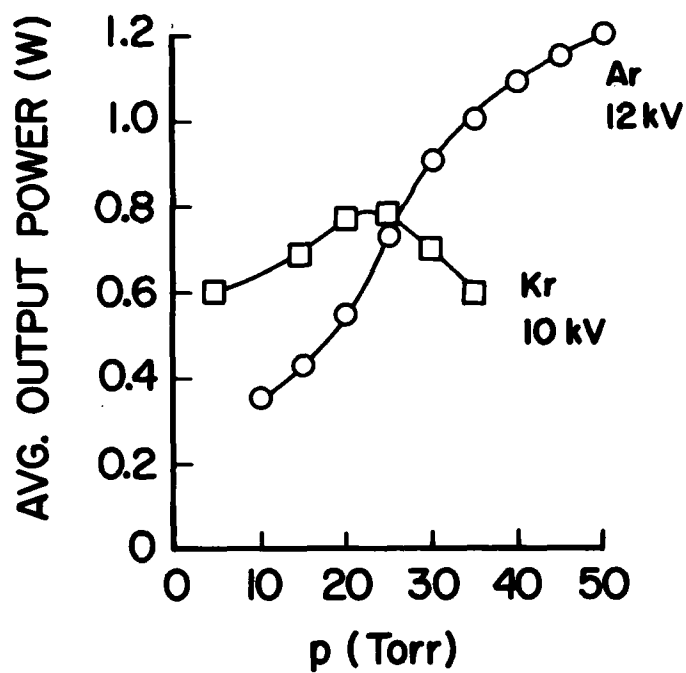
Figure 65. Dependence of laser output power upon amount
of Ar and Kr added to 1000-Torr He.

2.65, 3.11, 3.37, and 5.57 μ. The dependence of average laser output power upon charging voltage is shown in Fig. 66. Discharge arcing limited the charging voltage to a maximum of 6 kV. Obviously, operation at higher total pressure is desirable, but discharge arcing becomes more probable as pressure is increased. The dependence of average laser output power upon repetition rate is shown in Fig. 67. Discharge arcing prevented operation above 6 kHz. Decreasing the pulser inductance and risetime should enable operation at higher pressure, charging voltage, and repetition rate which would increase the laser output significantly.

Lasing was achieved in Ne-Xe mixtures at 2.03, 2.63, 2.65, 3.51, 3.65, and 5.57 μ. The dependence of average laser output power upon repetition rate for a 1000-Torr, 170:1 Ne-Xe mixture and a charging voltage of 2.5 kV is shown in Fig. 68. Laser output decreased for charging voltages above 3 kV. Since the supply of Ne was quite small, no other mixtures could be evaluated.

After obtaining the Ne-Xe data, the laser was partially evacuated and refilled with He and Xe to give a 1000 Torr He-Ne-Xe (500:500:4.4) mixture. A plot of the repetition-rate dependence of the average laser output power for this mix is shown in Fig. 69. The highest average power generated by the AFRL to that date was 3.99 W at 13 kHz. The lasing wavelengths were 2.03, 2.65, and 3.65 μ; the 2.03-μ line was strongest.

In order to investigate rare-gas-laser performance at pressures higher than 1000 Torr, the 1000-Torr capacitance-manometer head was replaced with a 10,000-Torr head. The maximum operating pressure was then dictated by the 2-atm. pressure limitation on the ferrofluidic seal.

113
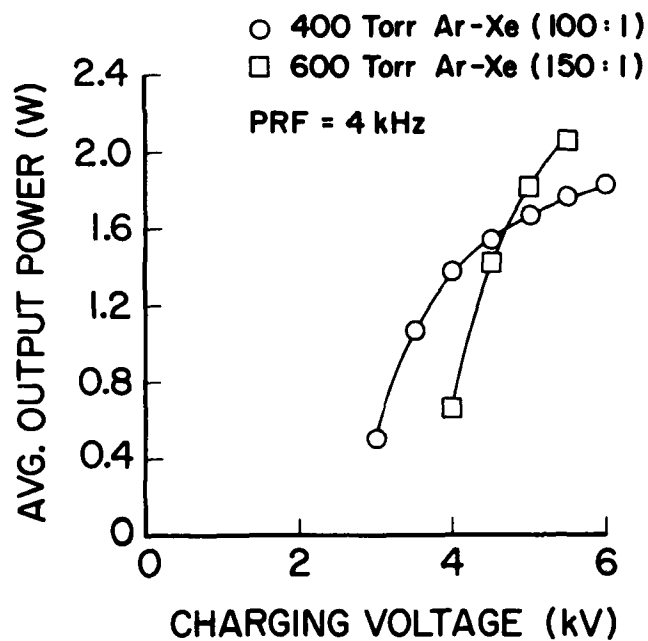
Figure 66. Dependence of Ar-Xe laser output power upon charging voltage.
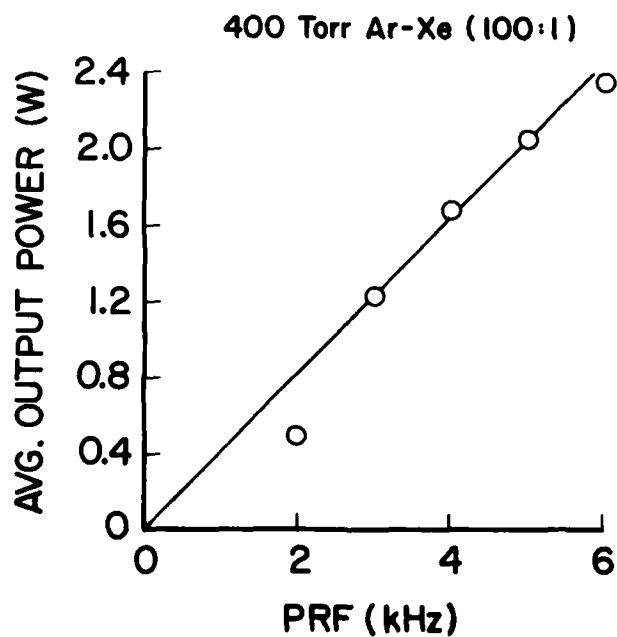
Figure 67. Dependence of Ar-Xe laser output power upon PRF.
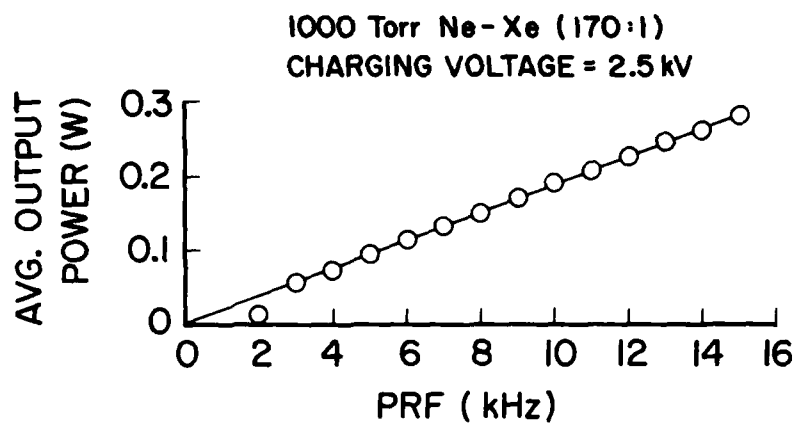
Figure 68. Dependence of Ne-Xe laser output power upon PRF.
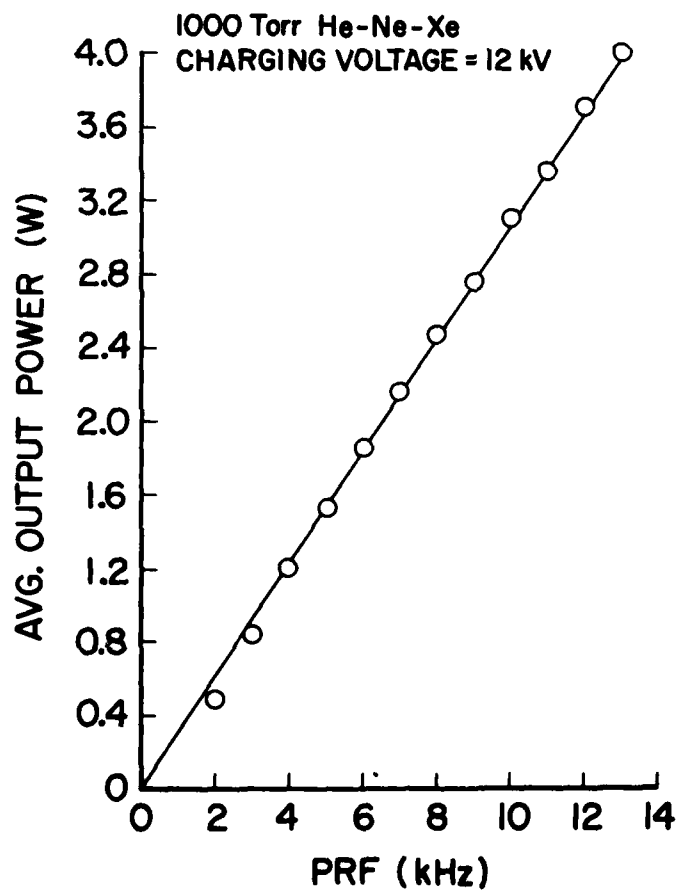
Figure 69. Dependence of He-Ne-Xe laser output power upon PRF.

The pressure dependence of the average laser output power for a 100:1 He-Xe mixture is shown in Fig. 70 for charging voltages of 5, 10, and 15 kV. As the charging voltage is increased, the output power increases and the maximum output power shifts to higher pressures. These data indicate that operation of the He-Xe laser at high voltage and pressure is required to achieve maximum output power.

Although the He-Xe laser output power increases with increasing pressure and voltage, the peak laser efficiency decreases. This is illustrated by the plots of efficiency as a function of charging voltage at various pressures shown in Fig. 71. The peak laser efficiency decreases in magnitude and shifts to higher voltage as the pressure is increased. At the highest voltages, however, the efficiency increases with increasing pressure; therefore, at the "usual" operating voltage for the AFRL of 12 kV, efficiency increases up to 1400 Torr and above.

In order to determine the AFRL system limitations during operation at high average power levels, the repetition rate was increased to a maximum at the highest charging voltage (16 kV) possible with the present power-conditioning setup. The repetition-rate dependence of the average laser output power from a 1200-Torr He-Xe (100:1) mixture is shown in Fig. 72. The 5.1 W of laser output at 9.5 kHz is the highest output generated by the AFRL to date. Discharge arcing prevented operation at 9.5 kHz for more than a few seconds. Sustained operation above 6 kHz was not possible because the water which cools the thyratron anode was boiling. An increased cooling-water flow rate will be required to avoid this boiling and permit continuous operation at high average
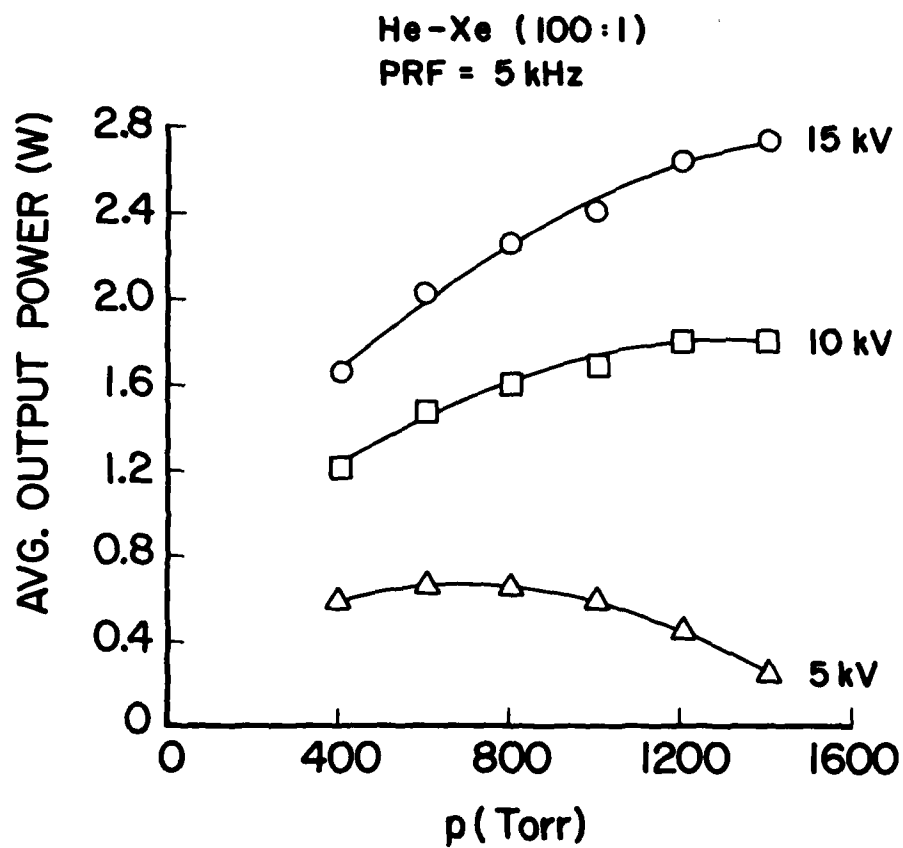
Figure 70. Dependence of He-Xe (100:1) laser output power upon total pressure at various charging voltages.

117

He-Xe (100 : 1)

PRF = 5 kHz
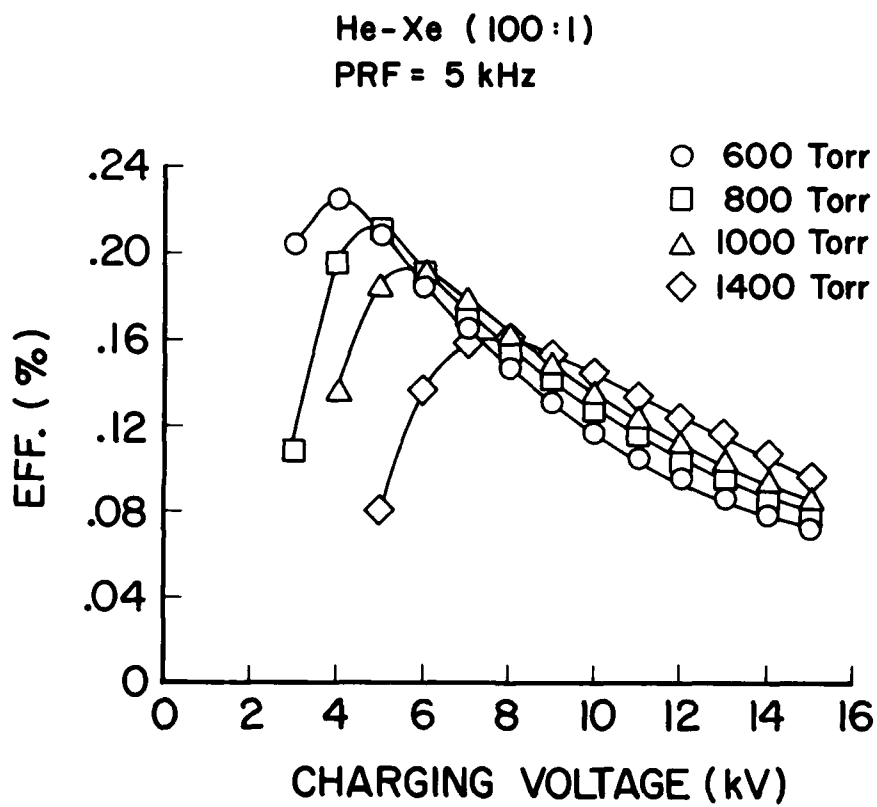
Figure 71.   Dependence of He-Xe (100:1) laser efficiency upon
charging voltage at various pressures.
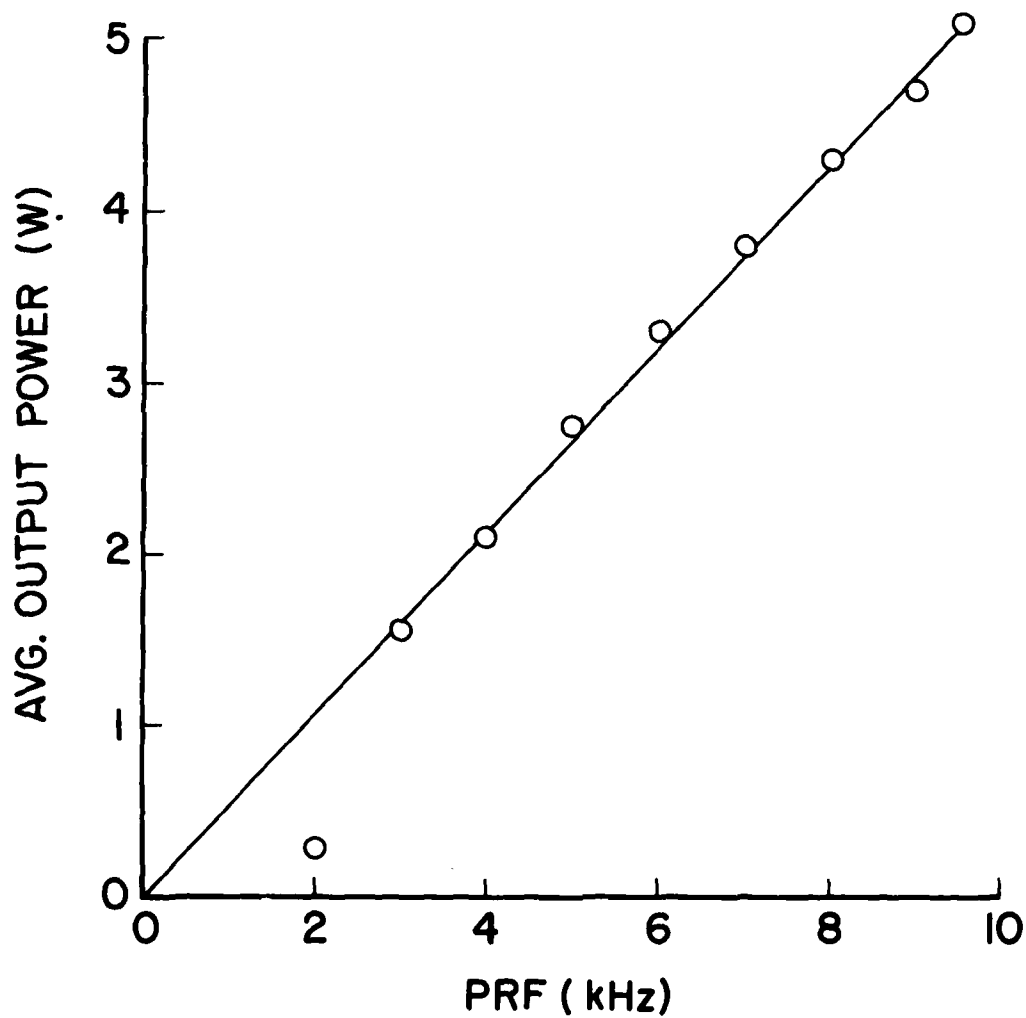
Figure 72. Dependence of He-Xe (100:1) laser output power upon PRF.

power levels. Also, a heat exchanger will be required to remove the 6 kW (at 9.5 kHz) of average power generated by the energy-storage capacitor.

Under the conditions given in Fig. 72, only the 2.03-, 2.65-, and 3.65-μ lines were lasing. Under the assumption of 1-μs laser pulse length, a total peak laser output power of ~ 500 W results. The 2.03-μ line is strongest with ~ 400-W peak power.

SECTION V

CLOSED-CYCLE XeCl LASER

During the last four years, rare-gas-halide (RGH) lasers have been developed to the point where they show promise of yielding energy densi-- ties and efficiencies comparable to those of high-power CO_2 lasers. Perhaps the most important shortcoming of RGH lasers is a rapid degradation of output power with operating time due to discharge-induced formation of contaminant species. This severely limits the usefulness of RGH lasers, particularly under the closed-cycle, fast-transverse-flow conditions required for high-rep-rate (high-average-power) operation.

The best RGH laser lifetime performance reported to date is for the XeCl laser.[38] This potential for long-life operation coupled with demonstrated efficient lasing and the relatively benign character of the halogen donor and discharge reaction products prompted the choice of XeCl for closed-cycle operation in the recirculating loop. The loop will be modified by adding flow transitions to accommodate a 50-cm discharge length as shown in Fig. 73. The inlet, discharge, and diffuser channels have been fabricated from 304-L stainless steel. The inlet and diffuser are 2-ft. long; the discharge section is 1-ft. wide and accommodates 50-cm-long electrodes mounted to demountable insulating plates. The discharge will be excited by pulse-charged cables which are thyratron-switched across a profiled cathode opposing a screened anode illuminated by UV from a spark array.

A Chang-profile cathode will be employed for the XeCl laser discharge. A set of programs was developed for an HP 2116C minicomputer to calculate
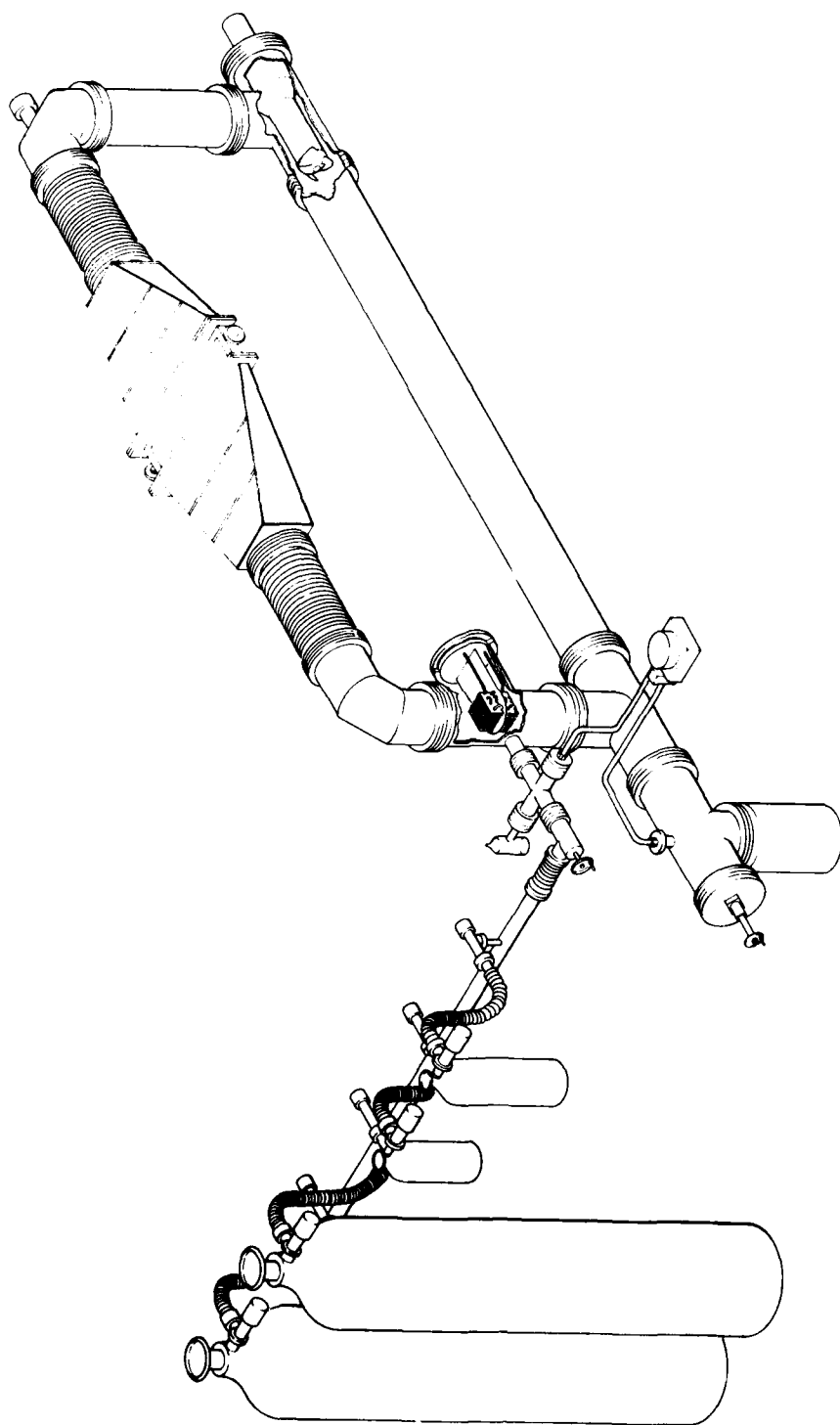
Figure 73. Isometric drawing of closed-cycle XeCl laser.

the coordinates of a uniform-field electrode based upon the conformal transformation of Chang.[53] An electrode designed to provide a uniform field (< 1.5% maximum deviation) over a 1×25 cm^2 area for a 1-cm spacing from an infinite plane was fabricated on a numerically controlled milling machine. Instructions for the machining operation using a ball-end mill were transferred to the machine by means of punched paper tape.

The Chang profile is superior to the Rogowski profile[54] in smoothness, compactness, and field uniformity. The Rogowski profile is actually made up of three unsmoothly joined segments taken from an infinitely wide analytic profile, whereas Chang's expression is a continuous function considering an electrode of finite width. The Chang profile is also superior to the Bruce and Harrison profiles, and the electric-field expression approximates that of Felici to the first order.[53] Due to the relative simplicity of the Chang equations, three-dimensional UFE profiles can be calculated, although this feature was not incorporated into the routines. The end points of the fabricated electrode have the same profile as the sides. A refinement in end-point calculations could be made, although it would complicate and lengthen the machining operation.

Preionization of the discharge volume will be accomplished via UV photoionization. The source will be bare spark gaps located ~ 0.5 cm behind the transparent anode, in the laser-gas environment, and will be electrically isolated from the discharge. This electrical isolation will permit a variable time delay between preionization and main-discharge energy deposition. It is expected that the optimum timing will vary, depending upon the type of chlorine donor, concentrations of the various gas constituents, levels of energy deposition, pulse repetition rate,

and possibly the number of previous pulses. The physical location of the spark sources dictates that the ionizing-gas constituents be fairly transparent to UV radiation. Initially, modified spark plugs will be used as the spark source, but the system mechanical design is sufficiently flexible to permit future installation of a more optimal configuration.

The choice of a chlorine donor involves consideration of three main factors: (1) adequate Cl concentration, (2) interference of the donor molecule or its fragments with laser action, and (3) ease of use in a practical system. The relative success of numerous donors[55] indicates that the Cl number density is generally not a limiting factor; therefore, the first requirement appears to be easily satisfied.

The second factor is difficult to predict. The Cl_2 molecule not only absorbs at the XeCl laser wavelength (~ 308 nm) but also promotes discharge instabilities. Candidate compounds of CCl_4, HCl, and BCl_3 do not absorb at 308 nm and do not appear to adversely affect the discharge.[55,56] The effect of fragments, however, is another matter. Good short-term success of a $Xe:BCl_3$ mixture has been reported[56] in a fast discharge, but lifetime data are not available.

Sze and Scott suggest a potentially long lifetime using an HCl donor.[57] In this case, it is postulated that Cl_2 molecules formed by HCl fragments are photodissociated by the 308-nm laser wavelength to form free Cl which, upon collision with an H_2 molecule, forms HCl*. In essence, the HCl donor and fragments form a recycling loop. Burnham[58] shows a 25% drop in output power over the first 20 pulses but less than a 1% change over the next 1000. However, the results of Burlamacchi and Salimbeni[55] indicate that this reaction is not entirely closed. They

124

report about 15,000 shots to half-power using HCl and various hydrocarbons. Burlamacchi, et al.,[59] report 180,000 shots to half-power accomplished with a Xe:CCl$_4$ mixture circulating in the presence of 3-Å molecular seive. The best XeCl laser lifetime performance has been reported by Miller, et al.,[38] who achieved a laser output of greater than 11 W at 250 Hz for 2.5 hr (2.25 × 10^6 shots) using a He:Xe:HCl mixture.

In summary, chlorine-donor fragments appear to affect the lifetime of a XeCl electric-discharge excimer laser adversely. Accurate gas-analysis data, however, are lacking. The reported decay of output power could be greatly affected by the presence of impurities. The closed-cycle XeCl laser shown in Fig. 73 will provide a low background impurity level. By analyzing the gas as a function of the number of discharge pulses, more insight can be gained into the conditions required for long-lifetime laser operation.

On the basis of reported results, the best Cl donor candidates for the proposed system are CCl$_4$, HCl, and BCl$_3$. Arc-free excitation in the presence of BCl$_3$ appears to require a very fast risetime discharge (~ 20 ns), whereas slower risetimes are tolerable with CCl$_4$ and HCl, both of which can be handled without resorting to exotic plumbing schemes, although the HCl is reactive in the presence of water. Therefore, CCl$_4$ will be used initially, with HCl being the second choice. The fill gas will be exhausted to the atmosphere through a chemical pump and scrubber.

At present, the gas-recirculation fan is externally driven through a ferrofluidic rotary vacuum seal. The possibility of seal damage by corrosive gases led to the search for a completely sealed drive mechanism. Torque could be magnetically coupled into the gas-recirculation loop by

means of external rotating magnets driving internal magnets connected to the impeller. An alternative to this would be a "canned motor" which is basically a polyphase induction motor with the stator windings located external to the gas loop. In both cases, the magnetic field would be coupled through a thin stainless-steel shell, alleviating the need for a rotary mechanical seal. In order to preserve high-vacuum integrity, however, the internal magnets or windings must exhibit low outgassing and be bakeable. This constraint is not insurmountable if the bakeout temperature can be limited to ~ 150°C.

The bearings which support the impeller shaft must also be high-vacuum compatible. Ideally, airfoil or magnetic bearings should be used. Airfoils impose limitations on the allowable gas-density range, which would restrict the system flexibility. Magnetic-bearing systems are more practical, but use of commercially available units would result in exposure of the gas flow to varnished copper coils and bare iron. One manufacturer has given an informal estimate of the cost of a specially designed vacuum-compatible motor and magnetic bearing system; but at this time, the cost is prohibitively high.

SECTION VI

UV PREIONIZATION

6.1 PHOTOABSORPTION AND PHOTOIONIZATION OF LASER SEEDING AGENTS

The possibility arose of systematic error in our previous measurements[40] of photoabsorption cross sections and photoionization efficiencies. At the low ionization-chamber pressures (0.02 - 0.3 Torr) employed, the electron mean free path may have been sufficiently large to permit electrons to gain enough energy to cause additional ionization. This Townsend amplification could have resulted in ion-chamber currents larger than those due to photoionization alone. Plots of ion-chamber current as a function of retarding potential were repeated, verifying that there was not a well-defined plateau region.

Two sets of measurements of ionization efficiency and absorption cross section were repeated for tri-n-propylamine, one set made at the original retarding potential and the other at 18% of the original. If Townsend amplification had been significant, measurements at the lower electric field would have yielded decreased ionization-efficiency values. Moreover, the deviation would have been much more pronounced at lower wavelengths due to the higher initial photoelectron energy. The results shown in Fig. 74 led to the conclusion that Townsend amplification was negligible for the previously reported measurements of photoionization efficiency and photoabsorption cross sections. The slight shift in the new data is within experimental error and could be attributed to chemical changes over the thirteen-month storage period.

127
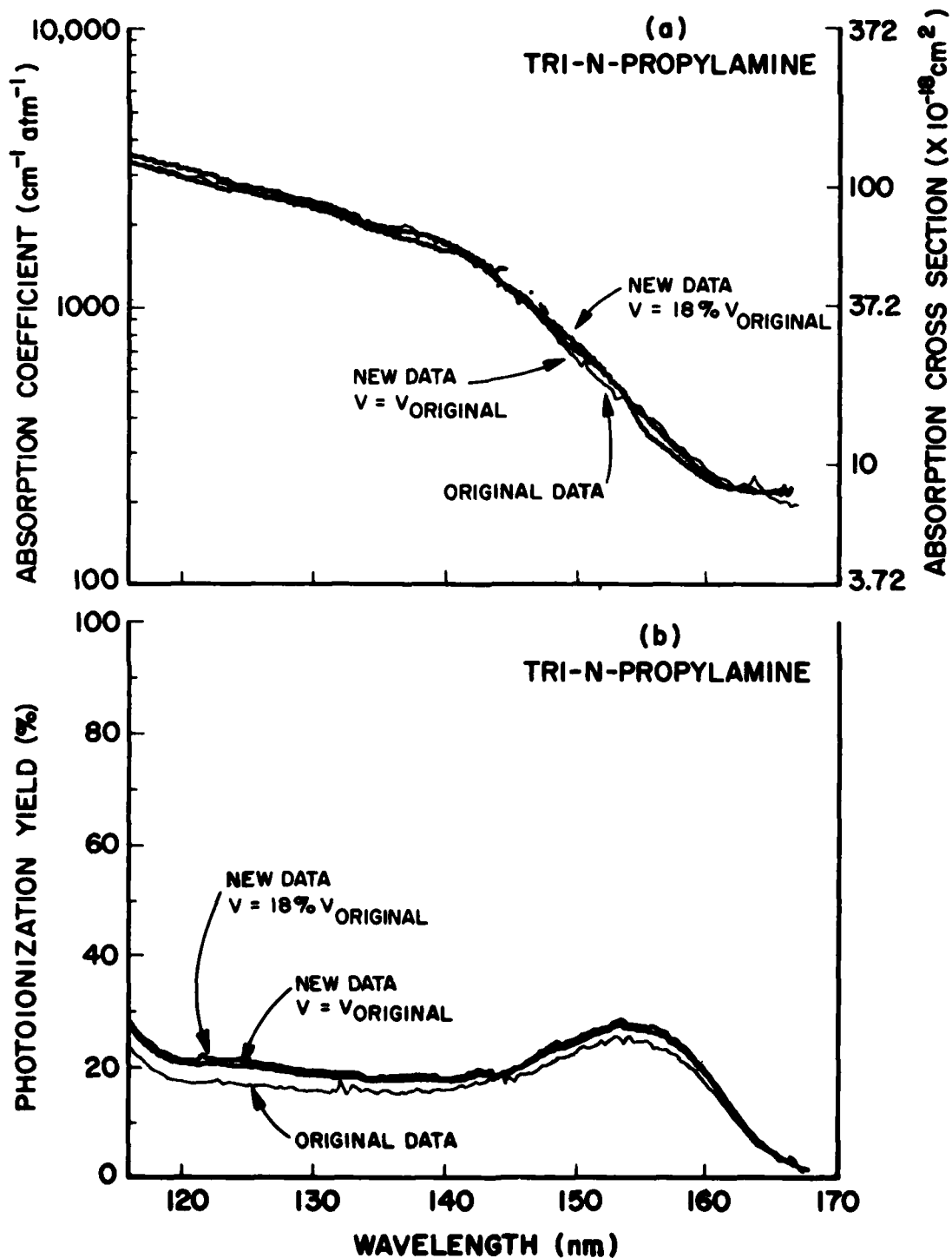
Figure 74. Comparison of original data and verification data on
(a) photoabsorption cross sections and (b) photoioni-
zation yield of tri-n-propylamine.

6.2 ABSOLUTE MEASUREMENT OF UV EMISSION FROM CO SPARK SOURCE

The main limitation of the laser seed compounds investigated and subsequently reported in the literature[60] is their low vapor pressure at low temperature which precludes their use in a static or slow-flow CO laser system. A more practical seed compound for use at lower temperatures is ethylene, which has an ionization potential (IP) of 10.5 eV[61] (118 nm). This relatively high IP (for comparison, N-N-dimethylaniline has an IP of 7.14 eV[62]) when coupled with the UV absorption of CO, restricts the usable radiation to a window of ~ 70 nm to ~ 118 nm. For modeling purposes it is important to know the amount of UV which can be expected during preionization of a CO laser.

Measurement of the emission and transmission of vacuum UV radiation generated by a sparker board in the 70 - 120 nm wavelength range should yield useful data for modeling. Since it was necessary to know the photon flux in absolute units of photons sec^{-1} sr^{-1} from a spark gap of a typical preionization sparker array, the vacuum UV scanning monochromator system was calibrated.

Figure 75 shows the experimental setup used for calibration. The output of a microwave-excited Kr resonance lamp was attenuated by water vapor prior to entering the monochromator. By recording the monochromator output (as measured by an NBS-calibrated photodiode) at the Kr resonance lines for various H_2O pressures, the absorption coefficients (K) at 116.49 and 123.58 nm were calculated from Beer's Law. Although some values for K are given in the literature for H_2O, this measurement was necessary in order to account for impurities which may have existed in the sample. The monochromator output with the absorption chamber evacuated was also

129
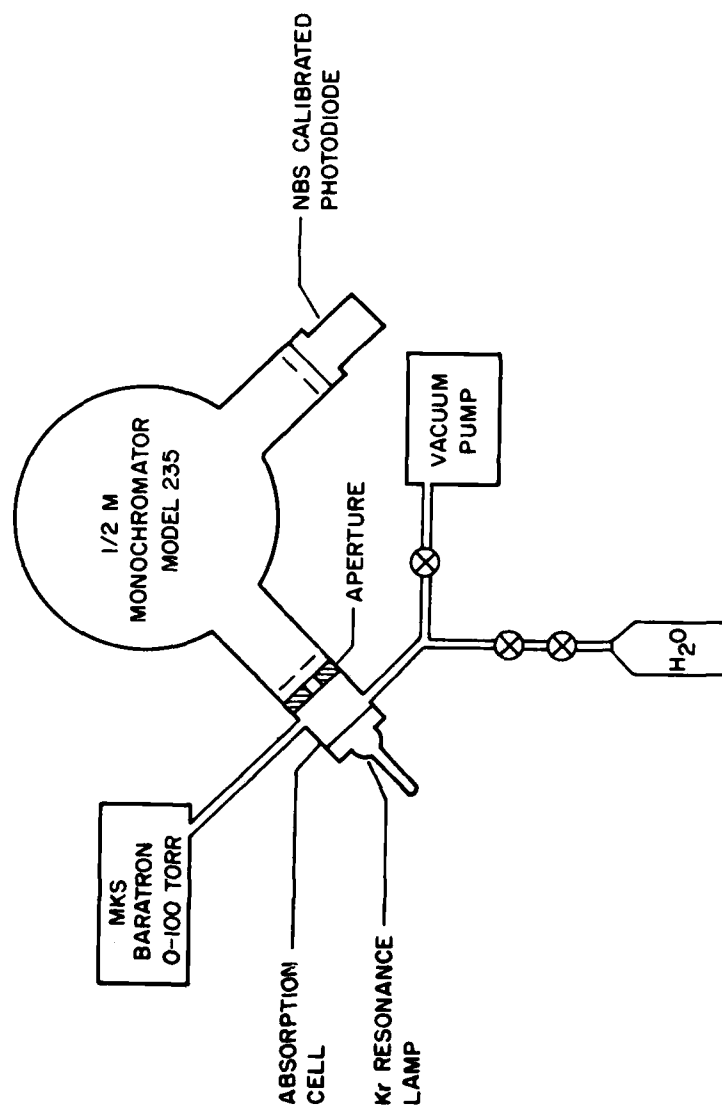
Figure 75. Schematic diagram of monochromator-calibration setup.

measured and recorded. The entire effective wavelength range of the photodiode was scanned in order to verify that only the two resonance lines produced a significant output from the photodiode.

The monochromator was then removed from the system and the lamp, absorption cell, aperture, and photodiode joined together. The output current (i) of the photodiode was recorded as a function of the water-vapor pressure (P). This arrangement is shown in Fig. 76. The effective f number (focal length/aperture diameter) of the light source/aperture combination was 12:4; the f number of the monochromator was specified as 24. This means that if the monochromator were used in place of the diode, only 12.4/24 of the energy measured by the diode would reach the detector. However, the monochromator includes a second aperture--the narrow entrance slit--which further reduces intensity. Considering this optical aperture, the optical throughput of the monochromator can be expressed as

$$I_{exit \; slit} = \frac{f_{lamp}}{f_{monochromator}} \times \frac{A_{slit}}{A_{aperture}} \times I_{diode}$$

where I is the intensity in photons/sec.

The intensities of each of the two Kr resonance lines were determined by assuming that the total energy seen by the photodiode is the sum of the energies from the two Kr resonance lines only. The measured diode current (i) is related to the resonance-line intensities by

$$i = q\gamma_1 I_1 + q\gamma_2 I_2 \tag{11}$$
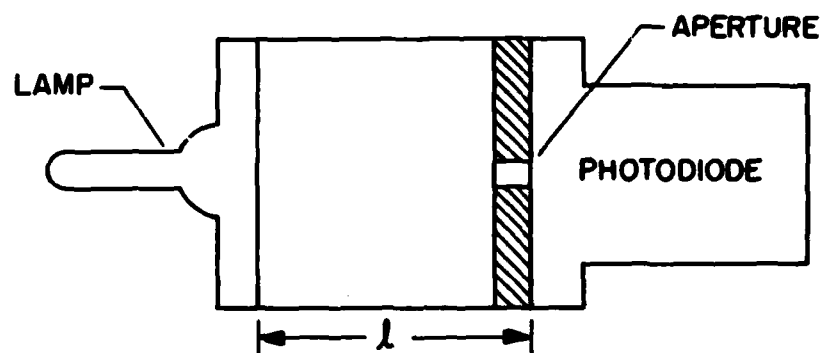
Figure 76. Experimental arrangement for lamp-output
measurement.

where q is the electronic charge, γ is the diode photo-conversion effi-
ciency (in electrons/photon), and subscripts 1 and 2 refer to the 116.49
and 123.58 nm lines, respectively. The energy detected by the photodiode
is dependent upon lamp emission attenuated by a Beer's-Law absorption.
In terms of lamp-emission intensity (I'), the above equation can be
written as

$$i = I_1'X + I_2'Y$$
$$X = q\gamma_1 e^{-K_1\ell} \qquad\qquad (12)$$
$$Y = q\gamma_2 e^{-K_2\ell}$$

where ℓ is the absorption pathlength between the lamp and the diode and
K is the absorption coefficient at the actual pressure and temperature.
Since I_1' and I_2' are constant and X and Y can be calculated using pre-
viously measured values of K along with measured values of pressure
(assuming constant room temperature), the recorded data resulted in
a series of linear equations. A linear regression was then performed
in order to arrive at a least-squares value for the lamp-emission inten-
sity of each of the two resonance lines.

A high degree of accuracy was not achieved with this method since
the lamp appeared to drift during measurement; the absorption properties
of the H_2O also created some problems. A refinement of the experimental
technique would be required in order to determine accurately the relative
intensities of the two resonance lines. This information could then be
used to measure the difference in monochromator-grating efficiency at

133

the two wavelengths. At the time, however, an average value was used

for lamp emission, and this value correlated with an average value of

the intensity (previously measured) at the monochromator exit slit

in order to arrive at an average monochromator efficiency of

0.48% (50-μm wide entrance and exit slits). A check was made to determine

the change in intensity when 10-μm input/output slits were used instead

of the 50-μm slits used for the initial calibration. The intensity ratio

was found to be 66.7; that is, average monochromator efficiency for the

10-μm-wide slits is 0.0072%.

Since the photodiode/amplifier response was relatively slow, a

sodium-salicylate/photomultiplier combination was calibrated against

the diode response. Although the sodium-salicylate fluorescence effi-

ciency is somewhat dependent upon wavelength,[40,63] a fairly constant

response can be assumed over the relatively narrow wavelength region

of interest.

To simulate the CO laser preionization sparker-board array, a

spark gap provided by Westinghouse Corp. was installed at the mono-

chromator entrance. The mounting structure of this gap was reversible

and, therefore, two different pathlengths (ℓ) were available. Calcula-

tions of monochromator field of view for the two pathlengths were made in

order to arrive at a final system-calibration value; this yielded emission

intensities of the spark for each pathlength in terms of photons sec^{-1}

sr^{-1} per μA of photomultiplier response. Figure 77 is a schematic repre-

sentation of the setup.

Our previous attempts to measure the UV emission of a CO spark

discharge in the wavelength region below the window limit (~ 116 nm)
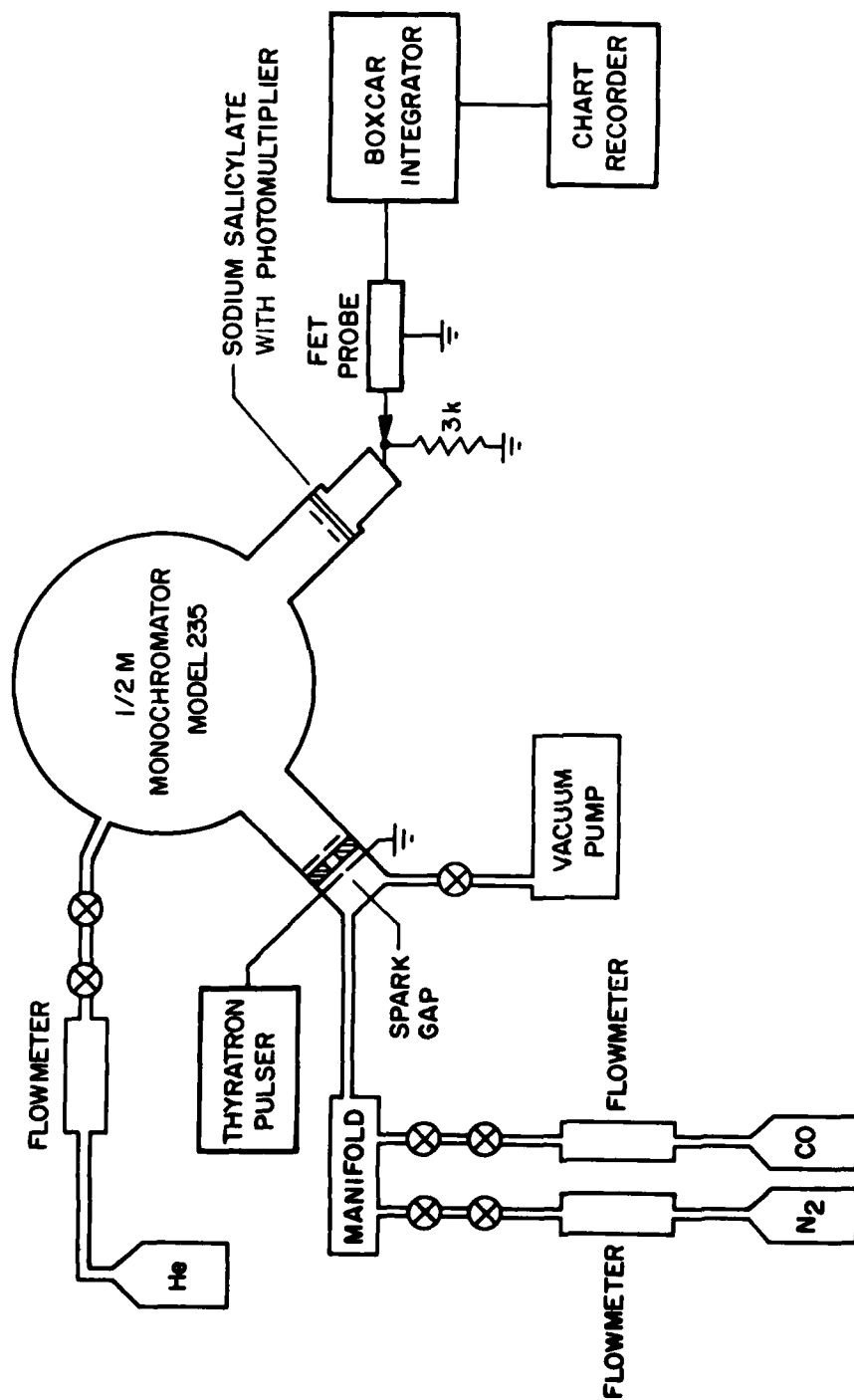
Figure 77. Schematic diagram of experimental apparatus for spark-emission measurements.

resulted in the destruction of the monochromator grating.[40] This was due

to the fact that the small amount of CO which entered the monochromator

chamber through the windowless entrance slit was photodissociated by the

UV, causing a carbon film to form on the grating surface. In order to alle-

viate this problem, the monochromator body was filled with He at a pressure

which was higher than the total pressure in the discharge chamber; this allowed

the He to flow through the entrance slit at a velocity sufficient to pre-

vent the migration of CO into the grating area (see Fig. 77). As long

as the pressure in the monochromator remained below atmospheric pressure, the

flow rate of He into the spark chamber was known. This flow rate was then

correlated with that of N_2 and CO into the spark chamber, with the

total pressure being monitored by a capacitance manometer. This per-

mitted determination of the gas composition at the spark gap. He was

used as the monochromator purge gas since significant absorption was

not expected to occur within the wavelength region of interest (70 - 130

nm). Multi-step absorption was assumed to be insignificant due to the low

probability of this process occurring as well as the short penetration length

of high-energy radiation (below 600 nm) through the high-pressure He.

Using this method, the spark-gap radiation intensity transmitted

through a known distance of the $CO:N_2:He$ mixture was measured as a func-

tion of wavelength with the UV scanning monochromator. The mixture

pathlength was then changed, and the monochromator scan was repeated.

This procedure was used to measure both the emission and the absorption

of a typical preionization source for two typical CO laser mixtures.

Figures 78 and 79 show the results for 1:3:9 and 1:3:36 mixtures of

$CO:N_2:He$. These spectra represent the average amplitude over the first

136
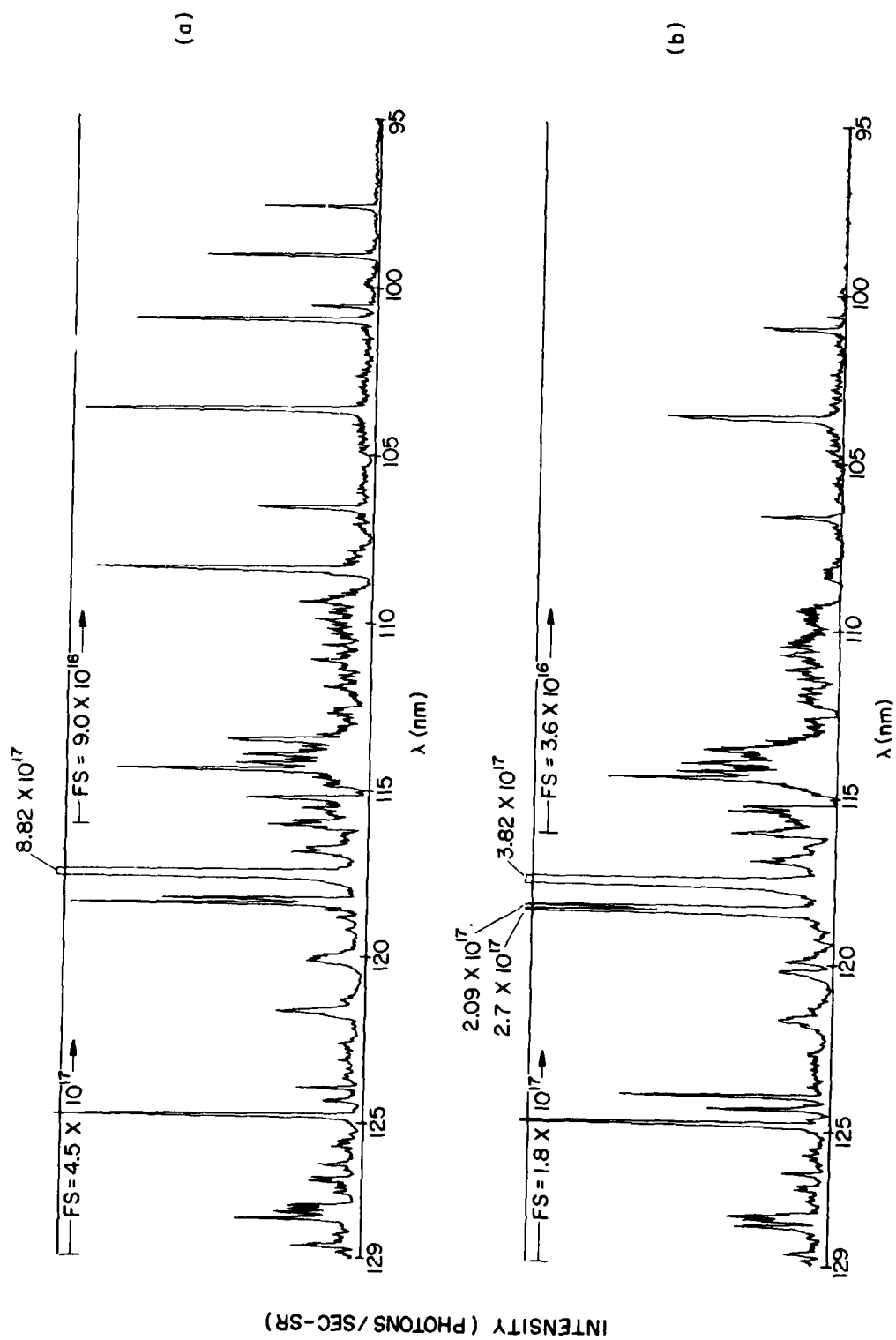
Figure 78. Spark spectra in CO:N$_2$:He mixture of 1:3:9 for pathlengths of (a) 3.81 cm and (b) 5.08 cm. Total pressure = 600 Torr.

137
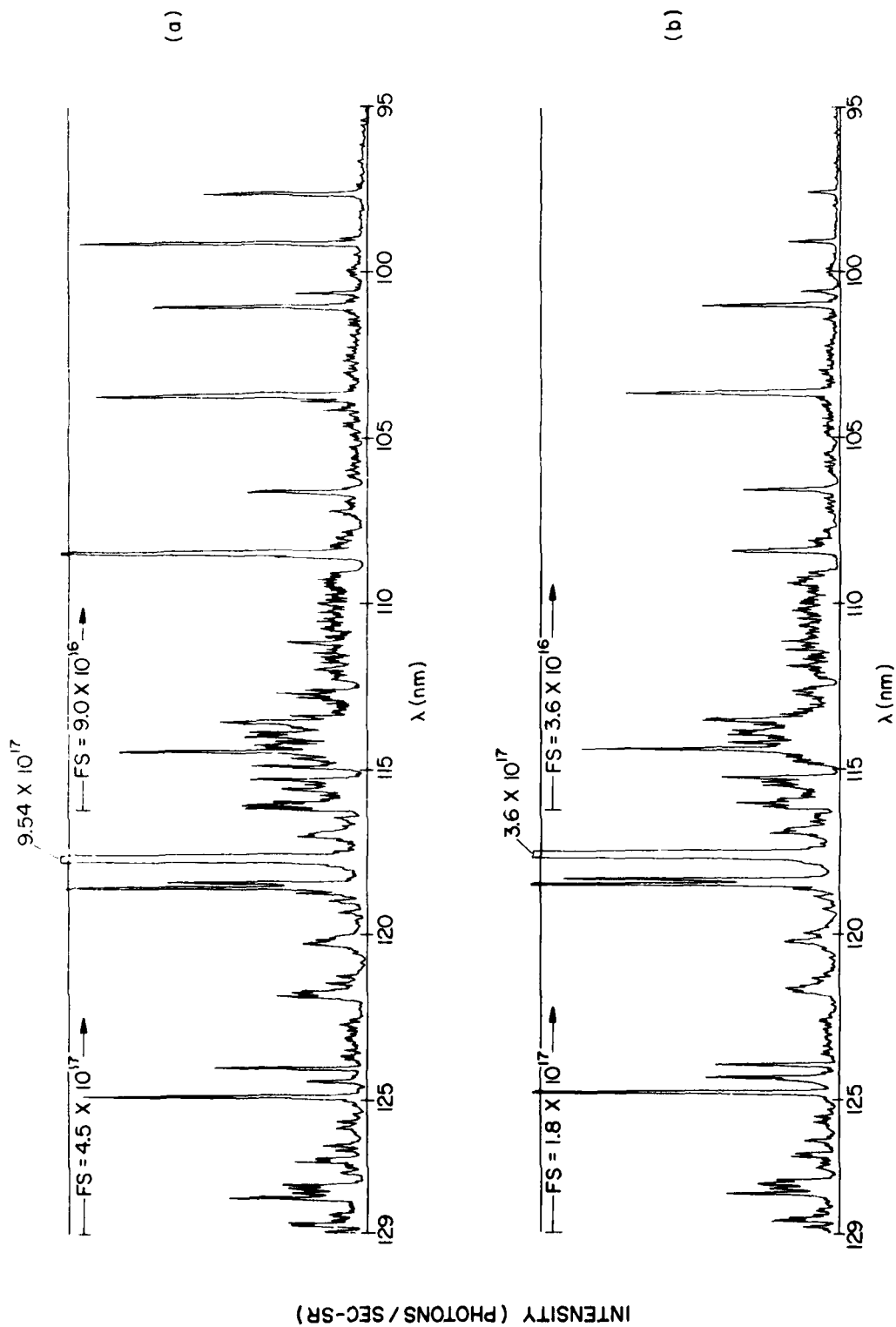
Figure 79. Spark spectra in CO:N₂:He mixture of 1:3:36 for pathlengths of (a) 3.81 cm and (b) 5.08 cm. Total pressure = 600 Torr.

138

600 nsec of the lifetime of the spark. Since the vertical values are in terms of photon rates, the spark pulse width must be considered in determining the total photon flux available for preionization. Taking into account the problems encountered in arriving at a monochromator-efficiency value—as well as in determining the monochromator cone and detected solid angle—the final calibration values are accurate only to within one order of magnitude.

The preceding discussion concerns the instrument calibration of the radiation falling within the instrument slit function, with frequency composition being neglected. The problem of limited resolution remains—that is, a collection of several narrow lines lying within a 1.6-$\overset{\circ}{A}$ spread could be recorded only as a single wide line whose amplitude depends not only upon the individual line amplitudes but also upon the line positions. Due to the resolution limitations of the present instrument, it is not possible to determine the actual composition of the recorded lines accurately. Therefore, in order to estimate the true spectral content, a list of probable lines along with their relative intensities was compiled from the NBS UV atlas. The spectrum was found to be composed, almost exclusively, of atomic N and C.

A trinagular monochromator transfer function of 0.8 $\overset{\circ}{A}$ FWHM was then used for deconvolution of the recorded spectrum. By regrouping lines of the deconvoluted spectrum according to the locations of the intensity peaks of the recorded spectrum, a corrected peak intensity was determined. The new peak values represented the total flux available in the vicinity of the measured wavelength. Effectively, a line spectrum (zero linewidth) was created to simulate the actual

139

emission spectrum. Since ethylene exhibits no discrete absorption in this spectral region, the results can be used to predict the extent of photoionization in an ethylene-seeded $CO:N_2:He$ mixture. Table 5 is a summary of the simulated spectra and calculated absorption coefficients of a 1:3:9 $CO:N_2:He$ mix.

The value for the source intensity (I at path length $\ell = 0$) was calculated by extrapolating the data at the two pathlengths back to the position of spark. Care should be taken when using this figure since the relative scale values have an uncertainty of 20 to 30%, depending upon sensitivity range and noise level. As the absorption approaches zero, the ratio of intensities for the two pathlengths approaches unity, resulting in an error range of several orders of magnitude for K. This could lead to an error as great as one order of magnitude for the calculated intensity at $\ell = 0$. Of course, as the ratio becomes larger, this error sensitivity is quickly diminished.

6.3 UV EMISSION FROM $CO_2:N_2:He$ DISCHARGE

UV radiation can be generated in IR gas-discharge lasers by both the preionization source and the main discharge. If significant amounts of UV radiation should reach the laser windows, degradation of the IR transmitting properties could occur. The interest in laser-window development generated by the USAF CO_2 laser program prompted the measurement of vacuum UV radiation generated by CO_2 laser discharges. UV radiation from a capillary discharge of a 1:1:8 $CO_2:N_2:He$ mixture was measured using the calibrated vacuum UV monochromator system. A large amount of UV resulting from the CO fourth-positive system between ~ 150 and 200 nm

140

TABLE 5

SIMULATED SPECTRA AND ABSORPTION COEFFICIENT GENERATED
FROM RECORDED EMISSION LINES OF A SPARK DISCHARGE IN
A $CO:N_2:He$ MIXTURE OF 1:3:9 (see Fig. 78)

Wavelength (nm)	Intensity ($\times 10^{16}$ Photons/sec-sr)			K (1/cm-atm)
	$\ell = 0$	$\ell = 3.81$ cm	$\ell = 5.08$ cm	(Assuming CO)
97.702	*	3.90	<0.2	*
99.158	*	5.33	<0.2	*
100.602	1200	1.98	0.234	25.6
101.022	3600	9.43	1.30	23.8
103.702	969	14.0	3.41	16.9
106.589	184	3.93	1.09	15.4
108.458	*	10.8	<0.5	*
109.273	302	3.00	0.645	18.4
110.036	129	5.19	1.78	12.8
110.793	7.80	1.46	0.835	6.70
111.026	38.6	1.80	0.648	12.2
111.446	42.7	0.810	0.216	15.8
111.772	50.8	1.91	0.640	13.1
112.914	18.2	1.17	0.469	11.0
113.441	123	6.88	2.63	11.5
113.933	62.6	7.61	3.77	8.42
114.163	30.2	4.00	2.04	8.07
114.365	113	7.86	3.20	10.7
115.215	175	3.96	1.12	15.1
115.639	113	2.79	0.812	14.8
116.100	58.4	3.15	1.19	11.7
116.400	23.8	5.36	3.26	5.96
116.845	158	14.1	6.30	9.66
116.906	100	21.4	12.8	6.16
117.571	2290	186	80.5	10.0
118.303	96.0	30.6	20.9	4.57
118.454	192	44.1	27.0	5.88
118.801	304	5.49	1.44	16.0
119.303	86.3	8.28	3.79	9.37
120.022	155	12.7	5.52	9.99

*The intensity data recorded at $\ell = 5.08$ are not sufficient for the
calculation of either the intensity at $\ell = 0$ or the absorption
coefficient (K).

was observed. Also, N_2 second-positive emission was clearly present above ~ 195 nm. No significant amount of UV was detected below 150 nm.

The capillary-discharge has an E/N comparable to that existing during the fast-avalanche pulse of a self-sustained discharge. However, since the lamp was operated cw, the gas composition may differ from that existing in an operational pulsed laser system. Of prime interest for high-power laser-window design is the UV emission of an e-beam-sustained laser system. In this case, values of E/P (P = pressure at room temperature) are typically ~ 2.5 V cm^{-1} $Torr^{-1}$, whereas in the capillary discharge, E/P > 20 V cm^{-1} $Torr^{-1}$.

For these reasons, a cylindrical discharge tube was mounted on the monochromator system and positioned in such a way that the UV emission of the positive column could be measured. Figure 80 shows typical spectra resulting from 1:1:8 and 1:3:18 CO_2:N_2:He discharges. The higher intensity of the 1:3:18 spectrum is due to the increased transmission of the laser mix resulting from a lower concentration of CO_2 and, consequently, lower concentrations of CO, O_2, and nitrous oxides.

The amount of damaging UV radiation which reaches the laser window depends primarily upon the energy deposited in the discharge, the transmission characteristics of the gas mixture (cross section, pressure), and the optical pathlength. The results of Fig. 80, then, are intended to show the spectral distribution rather than absolute intensity.

The possibility of employing an aerodynamic window--utilizing a compressed air source--for filtering out the potentially damaging UV radiation was considered. The absorption characteristics of O_2 and O_3 are favorable
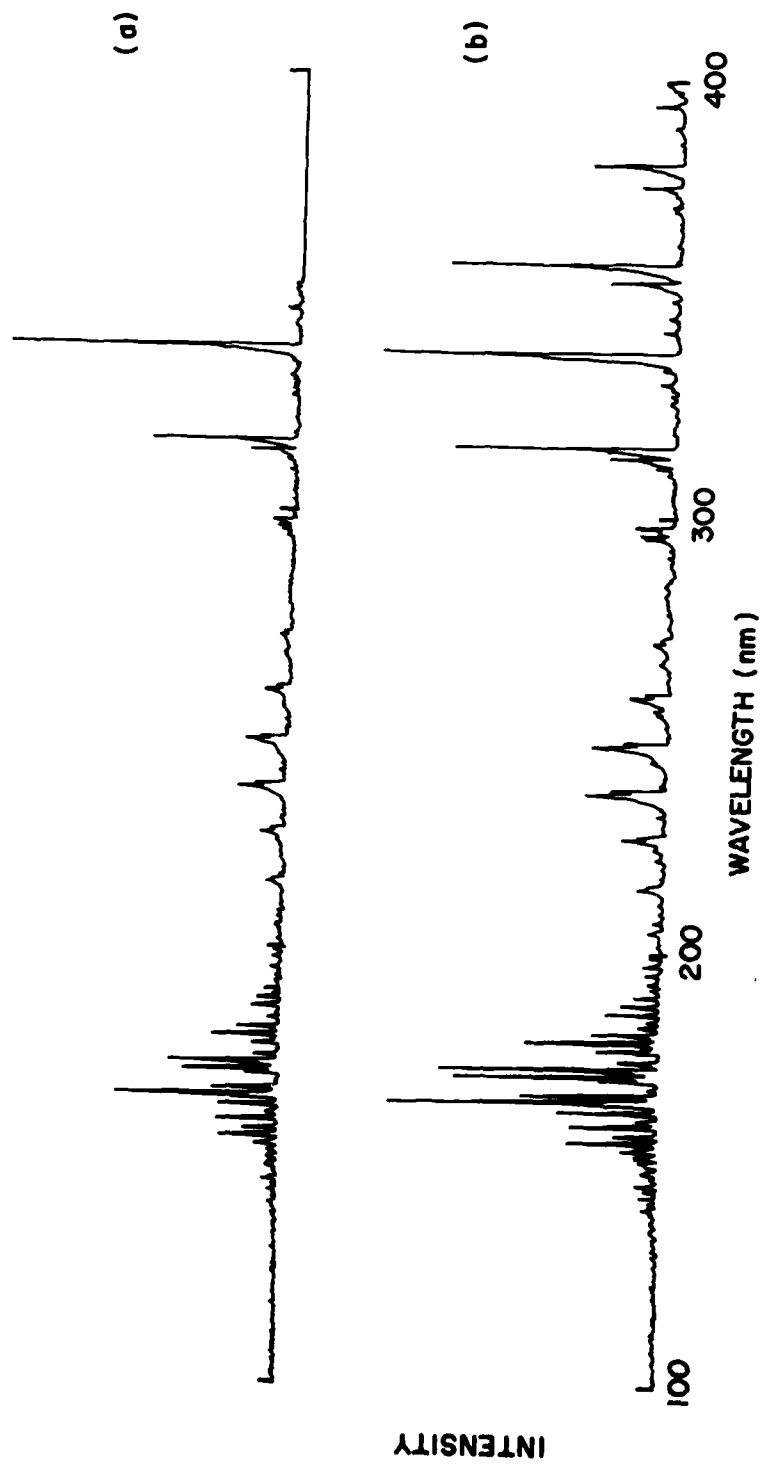
Figure 80. Positive-column emission of $CO_2:N_2:He$ discharge in proportions of (a) 1:1:8 and (b) 1:3:18.

143

for elimination of most of the damaging radiation. Since it was not practical to simulate an air window in the laboratory, the filtering effect of air was calculated using dry-air-composition data from Ref. 65. The results are shown in Fig. 81.

The measured emission of a 1:3:18 mix was used as a base, and transmission spectra were calculated for static atmospheric-pressure air and for moving air. A path length of 5 cm was chosen. The O_2 content for the static situation was taken to be 21% of the total air density; but since the high-energy UV could cause O_3 formation, the ozone partial pressure was assumed to be 10% of the O_2 present. In the moving-air case, the ozone concentration was assumed to be small since any O_3 formed would be quickly flushed out of the radiation path. This last case would be typical of an aerodynamic window.

Figure 81 demonstrates that oxygen—with an absorption continuum peaking at ~ 142 nm—can eliminate much of the high-energy UV below ~ 220 nm. The ozone continuum absorption spectrum peaks at ~ 255 nm and can be an effective absorber up to ~ 300 nm. The N_2 emission lines above 300 nm are not significantly affected by the air.

6.4   SLIDING SPARK AND DIELECTRIC-COUPLED DISCHARGE

The selection of an optimum method of discharge preionization included the consideration of sliding-spark arrays and dielectrically coupled discharges. The sliding spark, similar to those used on some UV preionized CO_2 lasers,[66] was investigated as an alternative to the auxiliary-wire-discharge technique. A coaxial spark array was fabricated by bonding short lengths of stainless-steel tubing to an alumina
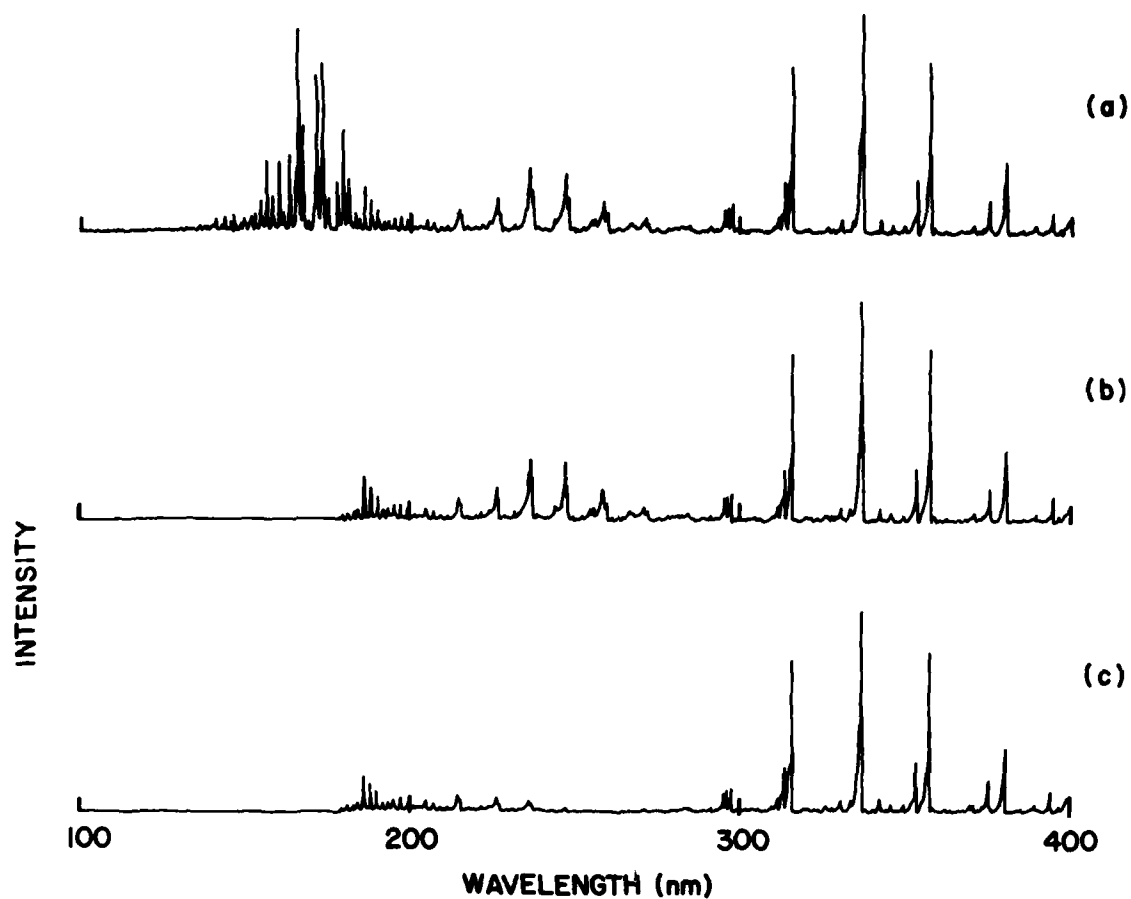
Figure 81. Comparison of transmission spectra of 1:3:18 CO_2:N_2:He discharge through 5 cm of air at 760 Torr. (a) Spectrum with no attenuation, (b) transmission spectrum through fast-moving air, and (c) transmission spectrum through static air.

tube surrounding a ground wire. Molybdenum-wire electrodes were spot welded to the stainless-steel tubes to provide a series of 46 raised sparks having ~ 1-mm gaps. The array was fed from one end by a 5-nF capacitor switched by an 8354 thyratron. Figure 82 is an oscillogram of the current and voltage pulses obtained for atmospheric-air operation at 15 kV and 10 Hz. The array operates in cascade, and the figure shows that it takes ~ 460 ns for the entire array to break down. This figure also shows the good impedance match of the pulser to the spark array in air. After a few minutes of operation, a sputtered metal film developed on the alumina which shorted out the spark capacitors, and sparking ceased. Although the energy loading was much greater than would be required for the laser, even at lower energy, sputtering would be a major problem for high-rep-rate long-time operation.

It is difficult to obtain spatial uniformity with a sliding spark since it is essentially an array of point sources. The dielectric-coupled discharge[67] exhibits a much higher degree of uniformity, but little is known about its operating parameters. A small test chamber was constructed in order to study some of the characteristics of this method of preionization and to determine its suitability for use at high repetition rates in a closed-cycle rare-gas laser. Figure 83 is a schematic of the experimental arrangement. Several electrical circuits were used, but the one shown in Fig. 83(b) generated the most intense discharge. As the capacitor—which consists of the two parallel plates separated by the dielectric and the adjustable gap—is charged to a high voltage, a uniformly distributed space charge forms in the gap. The sudden collapse of the field resulting from

146

CURRENT (200 A/DIV)

VOLTAGE (5 kV/DIV)
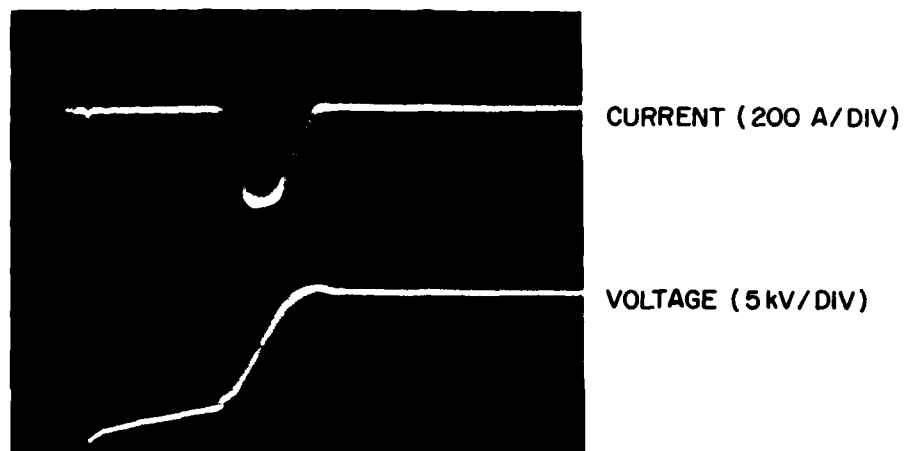
Figure 82.   Oscillogram of current and voltage pulses
for spark array in atmospheric air.
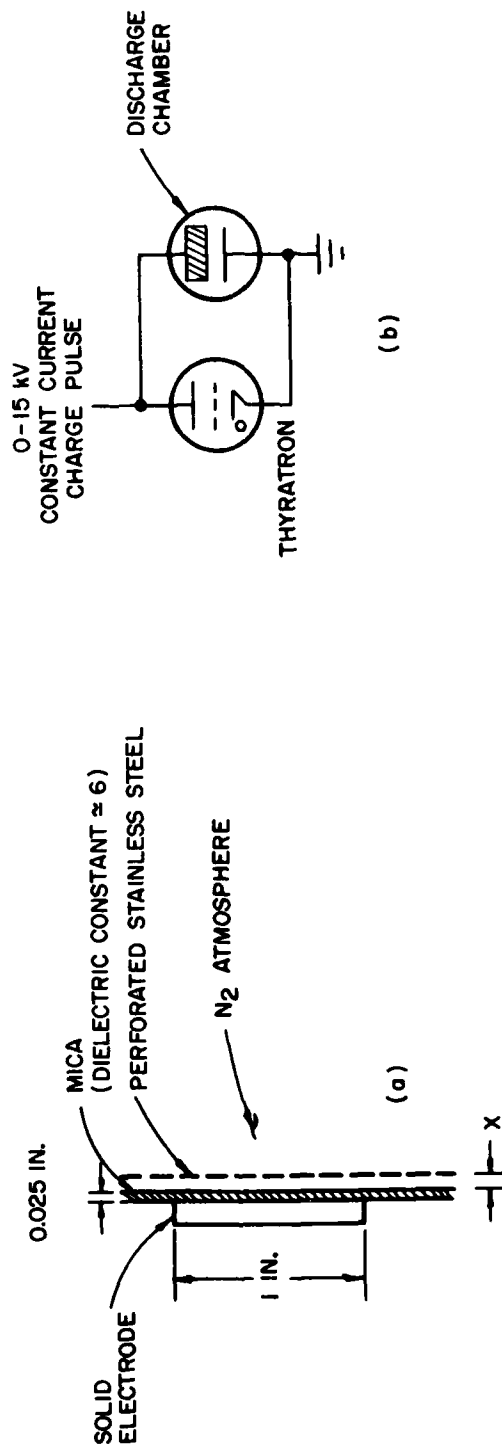
Figure 83. Schematic of dielectric-coupled discharge. (a) Physical arrangement, (b) electrical circuit.

148

thyratron commutation generates a current spike and, consequently, gas breakdown. This discharge may serve as a source of electrons (which drift through the perforated electrode) or, more likely, as a source of ionizing UV radiation.

The test chamber was mounted on the vacuum UV monochromator in such a way that the UV transmitted through the perforated electrode could be measured. In an atmosphere of ~ 10 Torr N_2, a very uniform low-intensity discharge was visually observed, but no UV could be detected. The detection threshold of the monochromator/detector system was ~ 10^{12} photons sec^{-1} sr^{-1}. At 600 Torr N_2, a diffuse discharge was observed as the gap was varied from ~ 0 to above 0.025 in. When the gap reached ~ 0.040 in., small, bright, moving anode spots were seen. The number of spots increased as the gap was increased. However, the UV detection threshold of the system was never reached.

When this preionization source was compared with a previously studied spark discharge,[40] the energy deposited per irradiated unit area was found to be about the same; but the emission from equivalent discharge areas detected by the monochromator was about two orders of magnitude less for the dielectric-discharge source. Considering that in the previous measurements numerous lines were observed in the 10^{15} photons sec^{-1} range, several lines should have been detectable from the dielectric source for comparable intensities per irradiated unit area.

The small test chamber was subsequently removed from the UV mono-chromator, and an independent electrode was installed opposite the trans-parent electrode. A drift field was then applied in an attempt to

measure the presence of electrons. After some physical problems were encountered with the Mica dielectric,it was replaced with 0.25-in.-thick barium titanate. This material has an extremely high dielectric constant (1000 - 6000), although its dielectric strength is relatively low. No systematic evaluation was performed with this setup because the barium titanate could not withstand operation at repetition rates of 500 - 1000 Hz. The use of this material at the high rep rates typical of the closed-cycle laser, therefore, is not practical.

Lack of time prevented the continuation of studies on the dielectric discharge. Considering the above factors—inadequate understanding of operating characteristics, low UV emission, and possibly limited repetition rate—this method of discharge preionization was ruled out as an alternative for the high-repetition-rate, closed-cycle, rare-gas laser systems. It should not, however, be considered unacceptable for future discharge systems. Recently, good success with a similar method has been reported in a rare-gas halide environment using PVC as the dielectric.[68]

SECTION VII

PHOTOEXCITATION OF MERCURY HALIDES

Although the spectroscopic features of the mercury-monohalide $B^2\Sigma^+_{1_2} \rightarrow X^2\Sigma^+_{1_2}$ transition have been known for some time,[69] the first report of laser action was made by Parks[70] in 1977. Since that demonstration of gain on the 558-nm HgCl line by e-beam pumping of Hg and CCl_4 in Xe plus Ar, lasing has been reported in e-beam-pumped and e-beam-sustained/discharge-pumped HgCl and HgBr and in photodissociated and discharge-pumped $HgCl_2$, $HgBr_2$, and HgI_2. The mechanism for creation of the upper laser level--$HgX(B^2\Sigma^+_{1_2}$ state) where X = Cl, Br, or I-- is generally attributed to ion-ion recombination in the case of e-beam and discharge pumping and to direct photoexcitation of the $HgBr_2$ salt to a dissociating state in the case of UV pumping.

The successful photolytic-pumped mercury-halide lasers reported to date utilize e-beam-pumped rare-gas excimer radiation or discharge-pumped rare-gas-halide laser output as the pump source.[72-74] If more efficient pump sources become available, photodissociative pumping promises high efficiencies since the fluorescence efficiency is significantly greater than that with the alternative pumping methods; up to 26% fluorescence-photon-to-exciting-photon efficiency has been reported for $HgBr_2$.[71] In addition to the potential for high efficiency, the photolytic method appears to avoid the degradation of the laser gas mixture, indicating potential for long-life closed-cycle operation.

Another advantage of the photodissociative mode of excitation is the ability to selectively excite to the upper laser level without

formation of electron-ion pairs and the myriad of excited states resulting from recombination. The optical-excitation method, then, is very useful in characterizing the laser kinetics, which would be applicable to all forms of excitation--particularly where scaling predictions are concerned.

In order to acquire some basic data on the gas kinetics of mercury-halide lasers, commercially available Xe flashlamps were considered as an excitation source. The relatively high inductance associated with linear-flashlamp circuits dictated the use of a coaxial lamp with an annular ground-return sheath. Such a lamp was manufactured by Phase-R Corporation, with a suprasil tube replacing the inner quartz tube in order to obtain Xe_2^* excimer fluorescence radiation down to ~ 160 nm.

Since HgX_2 is a solid at room temperature, operating temperatures of up to ~ 200°C are required. The present flashlamp/oven configuration is shown in Fig. 84. Heat tapes are used to heat the end piece with the copper coil as N_2 is passed through the coil into the inner oven cavity. The hot N_2 then flows along the length of the photolysis tube--between the tube and the coaxial Xe flashlamp--and exits through a hole in the oven cavity at the opposite end. Temperature measurements are made through this exit hole. By adjusting the heat loss at this end, the temperature of a portion of the photolysis tube can be regulated. If the remainder of this tube can be held at a higher temperature, the end temperature will determine the mercury-halide partial pressure within the tube. Heat tape is used on the lamp and exit-end oven piece to limit heat loss to the environment. Condensation on the end window has not been a problem.
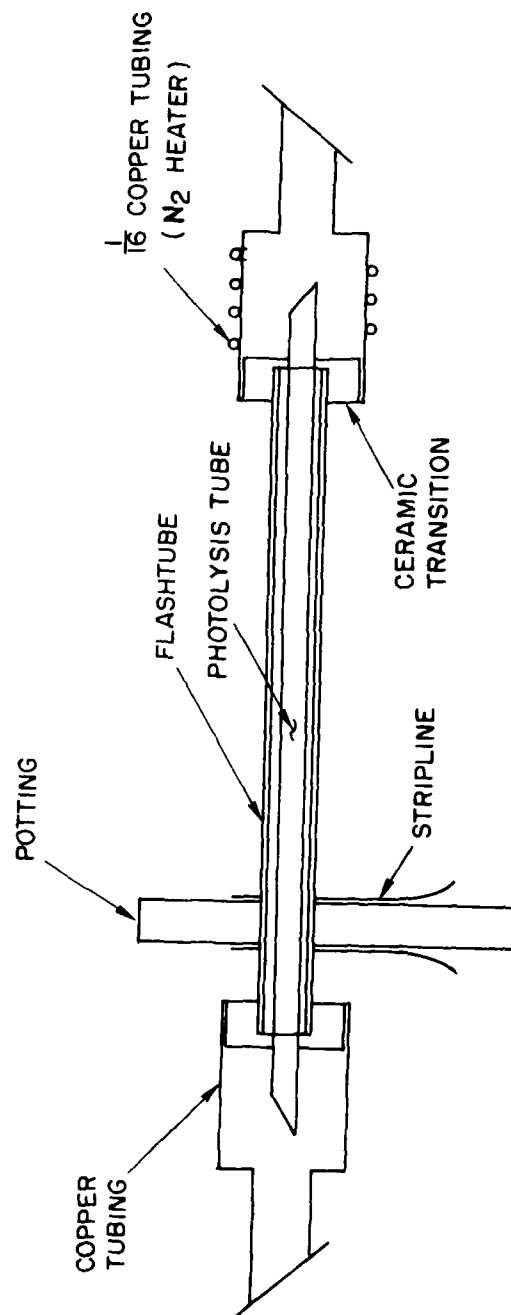
Figure 84. Schematic diagram of flash-photolysis apparatus.

The main drawback of this arrangement is the sensitivity of the flashlamp to high temperature. The electrical-energy-deposition capability of the lamp is ~ 180 J, but the stripline insulation will not accommodate the required high-speed high-voltage pulse at elevated temperatures. The outside of the lamp can be cooled but, thus far, sufficient N_2 flow cannot be maintained to adequately heat the HgX_2 for extended periods.

In attempting to predict the result of photoexcitation of $HgBr_2$, a disparity in reported photoabsorption cross sections has arisen. Figure 85 shows a comparison of published values. Although there is general agreement in the relative shape of the curves, the magnitude varies by nearly an order of magnitude. Also, the curve of Maya appears to be shifted toward lower wavelengths. The details of the experimental technique used by Templet, et al.,[76] and Schmitschek and Celto[73] are not available. Maya illuminated $HgBr_2$ vapor with the D_2 continuum, transmitted through quartz optics (cut-on ~ 185 nm). The transmitted spectrum was then resolved with a scanning monochromator. He considered such issues as Br_2 formation, existence of higher-order polymeric species, thermal dissociation at his operating temperatues (180 - 280°C), and the presence of excited-state absorption due to constant polychromatic illumination. All of these factors were considered negligible. However, in light of the ~ 5 nm shift of Maya's curve relative to the other two and the fact that quantitative data do not exist for the absorption band located at ~ 182 - 185 nm, a decision was made to measure the photoabsorption cross section of $HgBr_2$ with the in-house vacuum UV monochromator system.
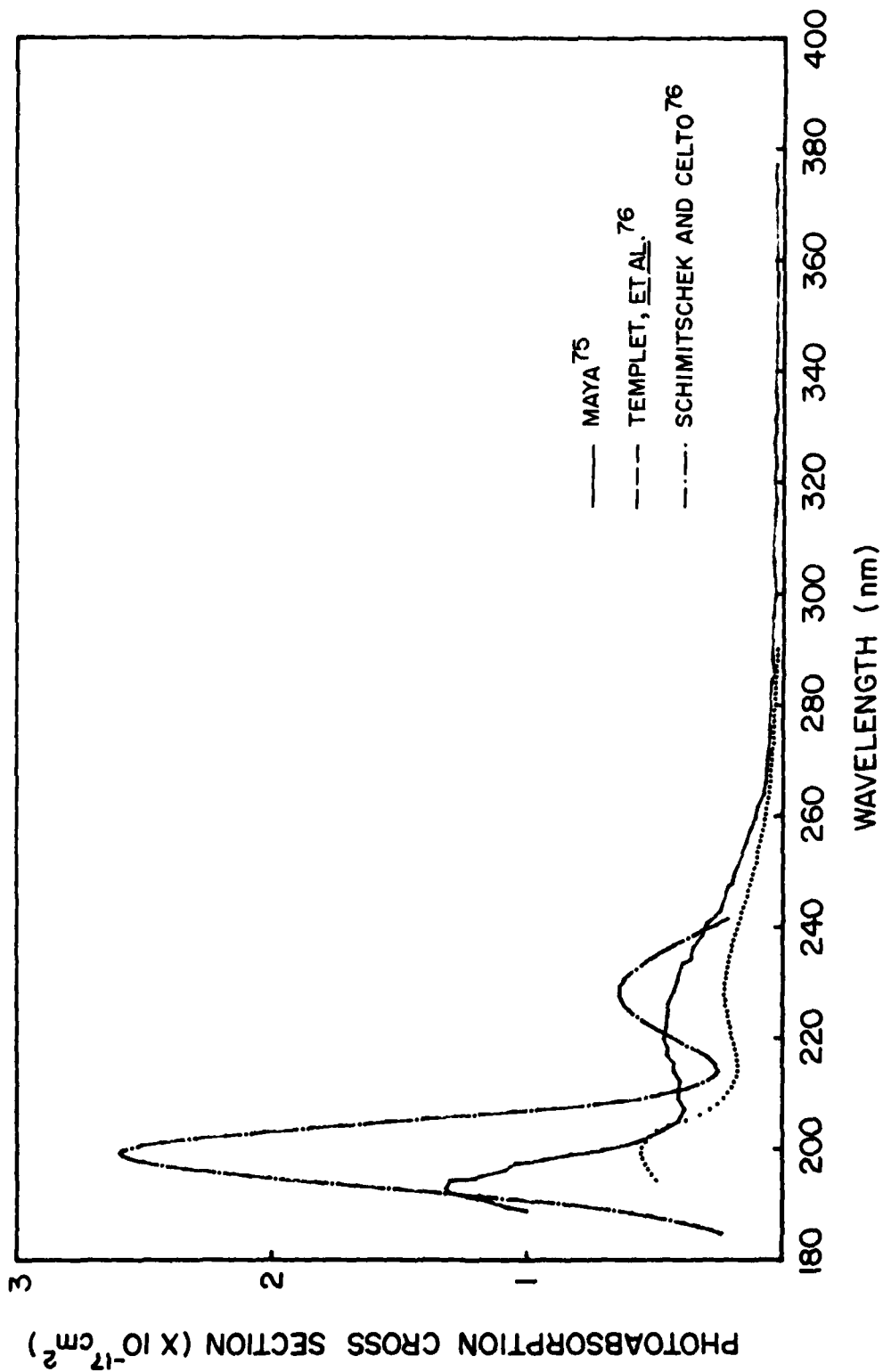
Figure 85. Reported photoabsorption cross sections for $HgBr_2$ from 185 to 380 nm.

Figure 86 shows the oven and absorption-cell arrangement which was mounted between the monochromator exit slit and the sodium-salicylate/ photomultiplier detector. The two thermal-isolation cells were constructed of stainless steel and maintained at a high vacuum ($\sim 10^{-6}$ Torr) to prevent conduction and convection losses; the outside flange was water cooled. The oven body was constructed of aluminum and was pressurized to $\sim$ 5 psig of He for heat transfer to the absorption cell. A slow flow of pre-heated He was maintained to aid in the removal of thermal gradients as well as to prevent the buildup of contaminants.

The absorption cell, constructed of quartz and having suprasil windows, contained a side-arm for pressure control. That is, the cell side-arm (or cold finger) is installed into the oven cold finger; during operation the remainder of the cell is maintained above the temperature of the cold finger (typically by $\sim$ 25°C). Therefore, the vapor pressure of the $HgBr_2$ can be determined by monitoring the oven-cold-finger temperature and converting to pressure using measured thermodynamic constants.[77] The estimated accuracy of the temperature measurements is $\pm$ 2°C, although this has not yet been verified.

The optical source is a hydrogen continuum emitted from an H_2 capillary-discharge lamp. The output of this lamp is spectrally scanned by the 0.5-m scanning monochromator, which results in a smoothly varying stable source of radiation in the wavelength range of $\sim$ 175 to above 300 nm, with a spectral resolution of 0.25 nm. Although the H_2 molecular-band line spectrum is present below $\sim$ 170 nm, it is beyond the wavelength of interest. Second-order lines of intense Lyman bands are removed by the Suprasil windows of the oven and absorption cell. Figure 87 shows the
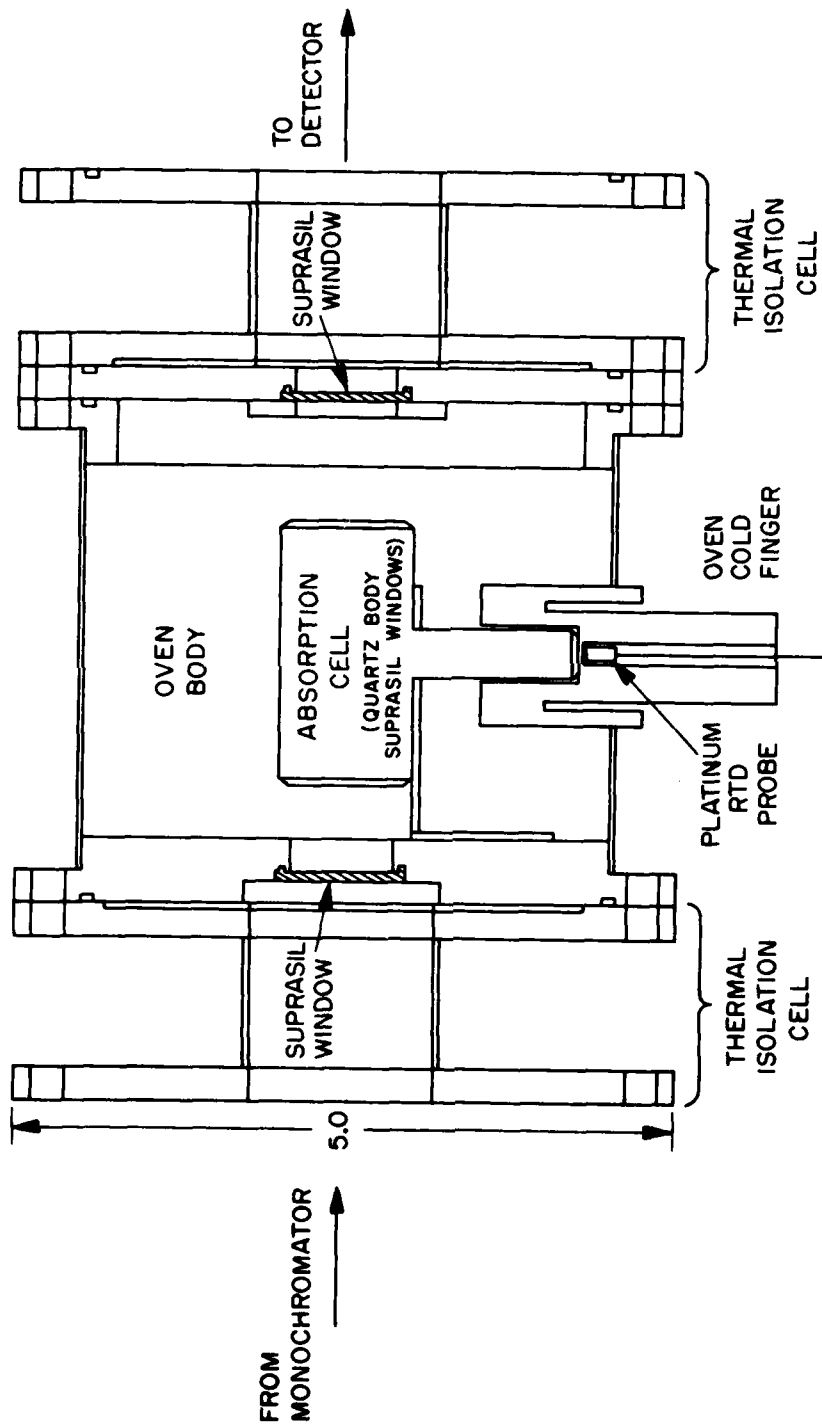
Figure 86. Schematic diagram of oven and absorption-cell arrangement for $HgBr_2$ photoabsorption-cross-section measurements.
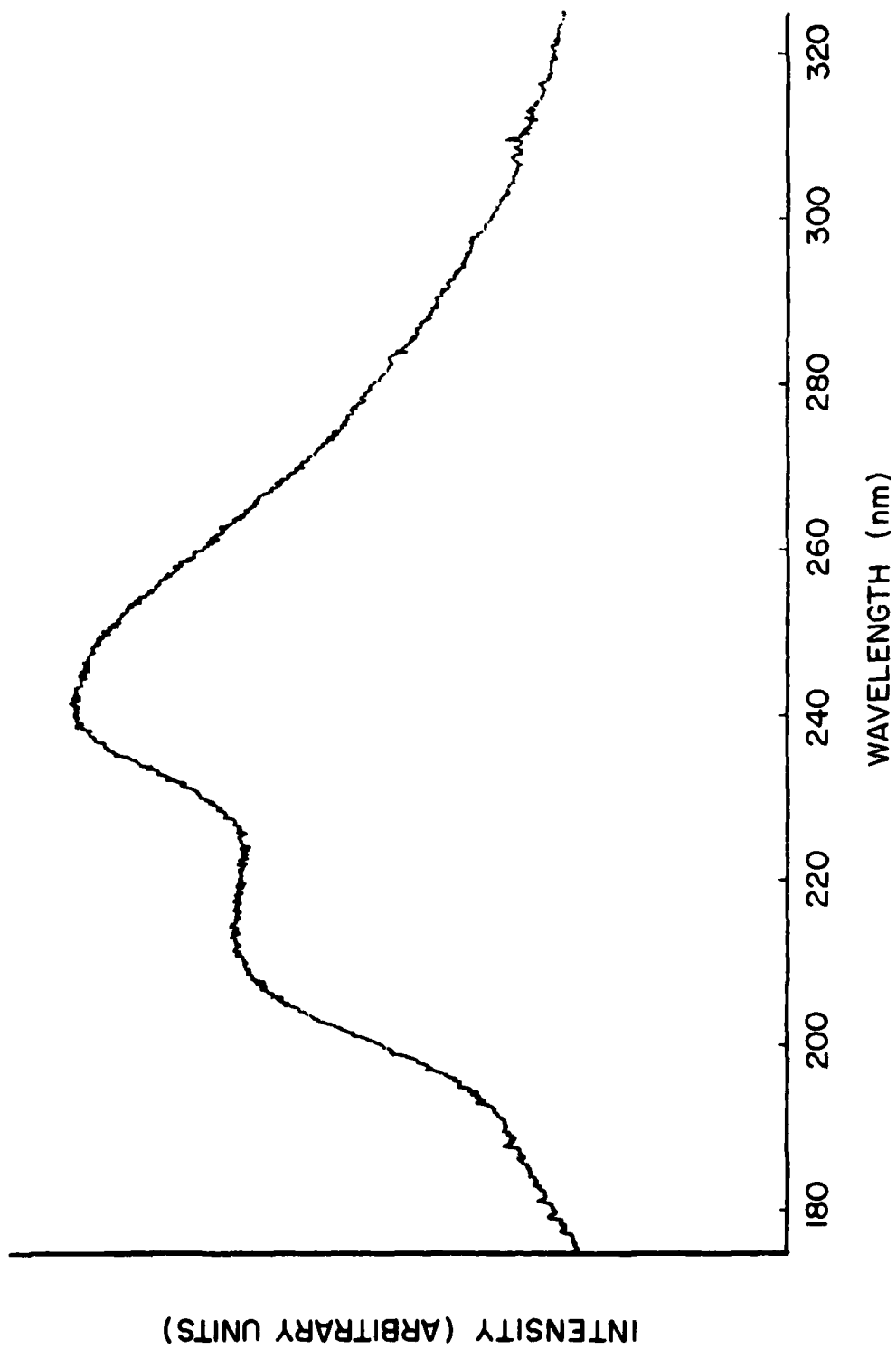
Figure 87. Source spectrum from H_2 lamp/monochromator for $HgBr_2$ photoabsorption measurements.

measured spectrum of this system, with the oven windows and absorption cell in place but with no $HgBr_2$ present. Although the intensity scale is in relative units, the peak intensity represents an absolute photon flux of $\sim 5 \times 10^7$ photons/sec.

Figure 88 is a schematic diagram of the experimental setup, showing the data-acquisition system. The capillary lamp was operated in the current-regulated mode; and, as long as the H_2 pressure and lamp temperature remained constant, a constant, repeatable UV output to the oven was obtained. The output of the photomultiplier was routed through an I/V converter and DVM into a minicomputer. The procedure was to store the transmitted spectrum of the 5-cm-long sample cell without $HgBr_2$ and then record the transmission with a known pressure of $HgBr_2$. The sample cell also contained ~ 250 Torr (room temperature) of ultrapure He. Assuming that absorption follows the Beer-Lambert law, the cross section (σ) could then be calculated as a function of wavelength from

$$\sigma = \frac{1}{n\ell} \ln \frac{I_o}{I} \qquad (13)$$

where ℓ is the absorption path length, I_o is the incident intensity as determined by the recorded transmission spectrum without $HgBr_2$ present, I is the measured intensity with $HgBr_2$ absorption present, and n is the $HgBr_2$ density. Combining the thermodynamic expression for $HgBr_2$ vapor pressure as a function of temperature[77] with temperature and pressure corrections, the density in the absorbing path was calculated from

$$n = n_o \frac{10^{[-(4167.4/T_1) + 10.181]}}{760} \frac{273.16}{T_2}$$
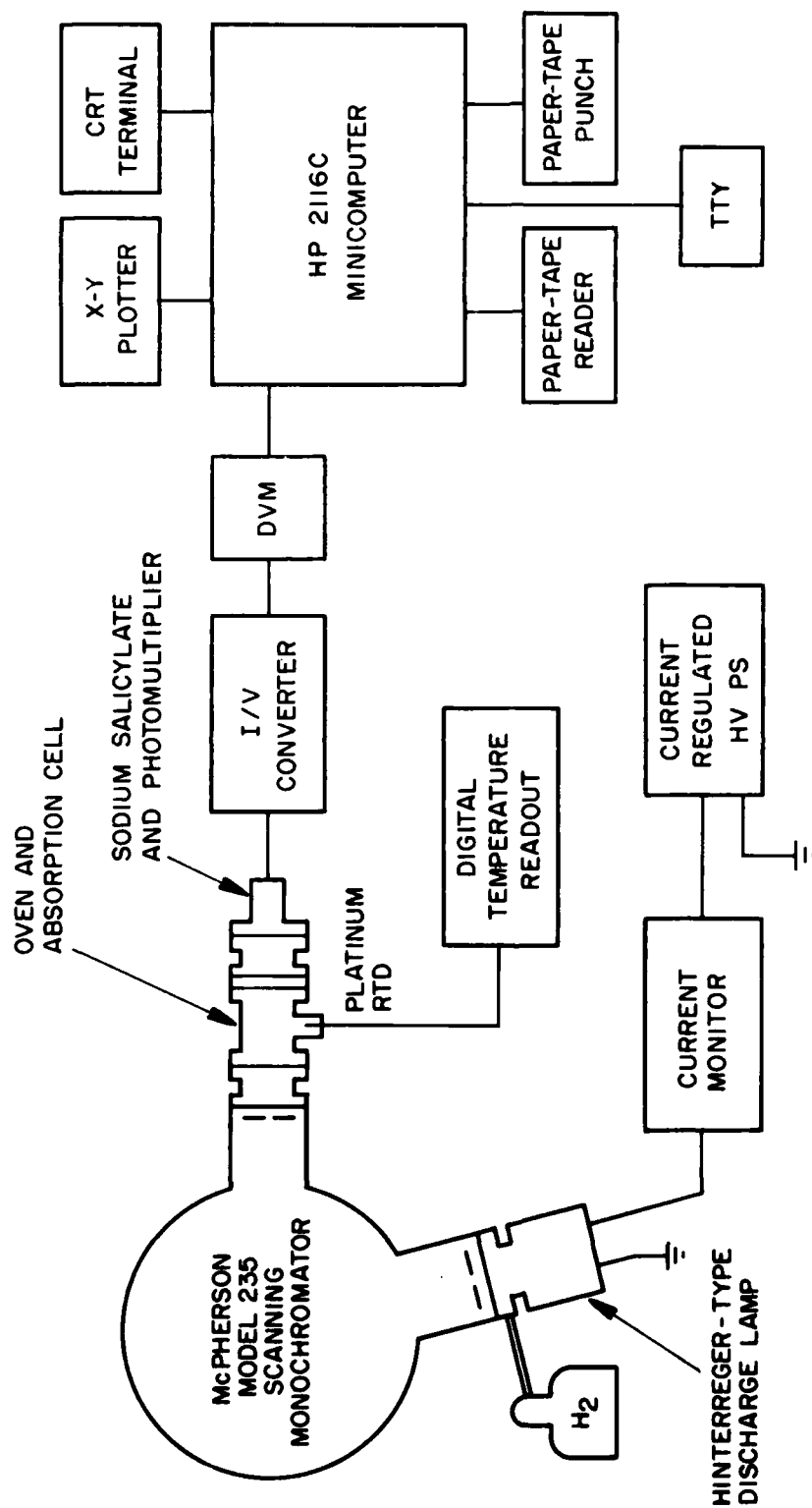
Figure 88. Schematic diagram of experimental apparatus for $HgBr_2$ photoabsorption-cross-section measurements.

160

where n_o is Loschmidt's number, T_1 is the temperature of the cold finger (pressure-determining point), and T_2 is the temperature of the vapor in the absorption path (essentially the oven temperature) in °K.

Figure 89 shows the photoabsorption cross section of $HgBr_2$ measured at 130°C (vapor pressure of 0.69 Torr). The general shape agrees well with those reported above 190 nm by previous authors, although--again-- there is disagreement as to the magnitude. The major uncertainty in our measurements arises from the temperature measurement. The estimated uncertainty of ~ 2°C results in a cross-section error bar of ~ 12%. Even if the error were as large as 5°C, the resulting uncertainty of ~ 30% still would not agree with Maya's uncertainty of ~ 20%. This discrepancy has yet to be resolved. A slight temperature trend was found in our data in the spectral range of ~ 195 to 225 nm, but the remaining absorption-cross-section values varied less than a few percent as the cold-finger temperature was varied from 110 to 130°C. Therefore, measurements should be made at higher temperatures (up to ~ 180°C) in order to determine whether the results are temperature dependent, which is indicative of a systematic error. In this case, the absorption path must be decreased in order to maintain a sufficient transmitted intensity for accurate measurements.

The shape of the absorption-cross-section plot of Fig. 89 suggests that several factors are applicable to the operation of a flashlamp-pumped $HgBr_2$ laser. Three bands are clearly visible, peaking at ~ 230, 198, and 183 nm. These have been designated by Weiland[69(a)] as the a, b, and c bands, respectively. The absence of structure in the a and b
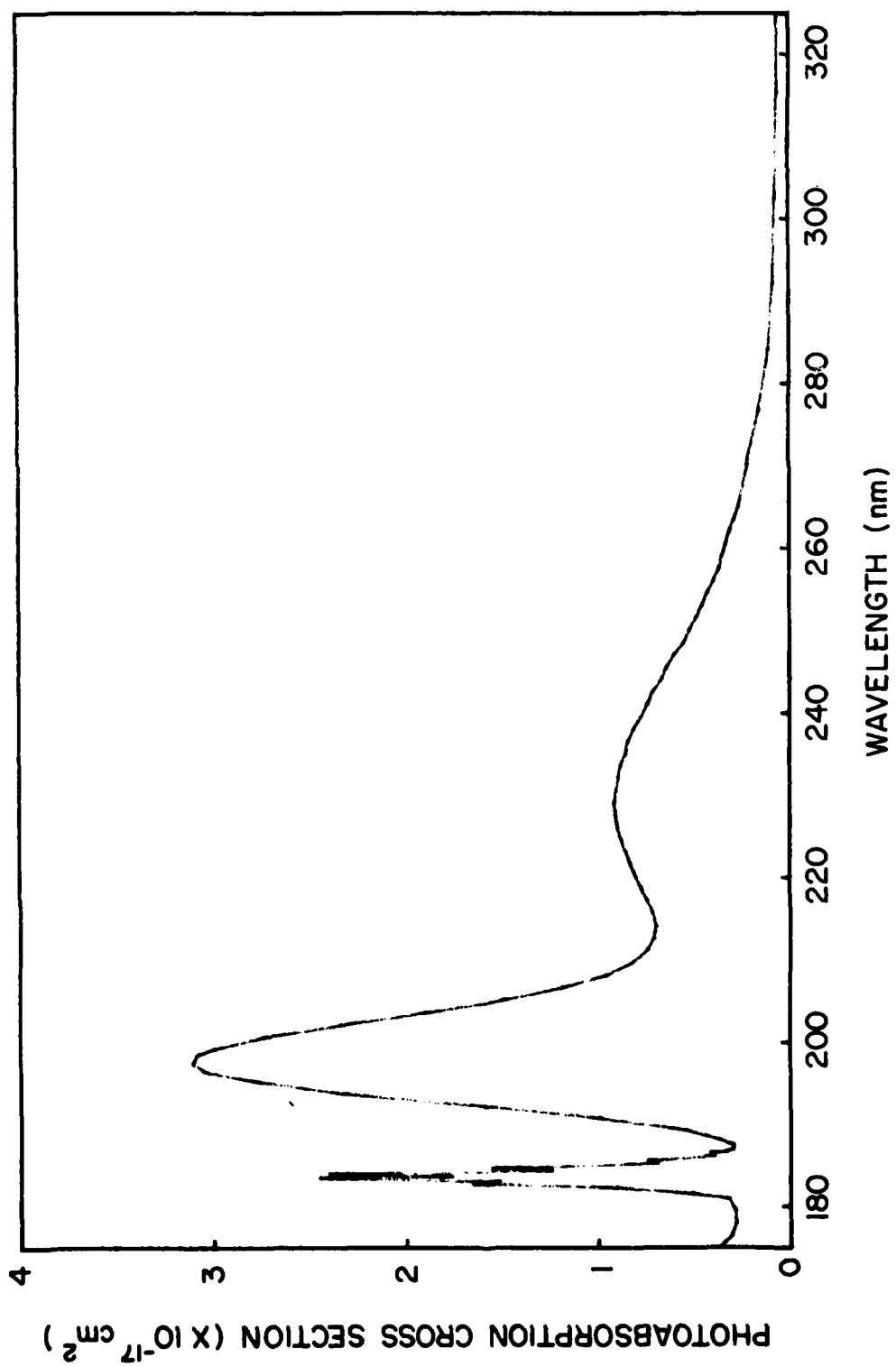
Figure 89. Measured photoabsorption cross section of $HgBr_2$ from 175 to 325 nm.

bands is indicative of transitions from the bound lower state to an unbound (dissociative) excited state. The a state, however, apparently dissociates[71] to the $X^2\Sigma_{\frac{1}{2}}^+$ ground state of HgBr. This is the lower laser level of the HgBr laser. The b state of $HgBr_2$ dissociates rapidly,[74,75] resulting in HgBr formation in the $B^2\Sigma_{\frac{1}{2}}^+$ excited state--which is the upper laser level. Consequently, efficient operation of a $HgBr_2$ photodissociation laser requires that the pump radiation lie in a band between ~ 190 and 205 nm and requires the absence of radiation from ~ 210 to ~ 260 nm.

The effect of absorption in the 182 to 186 nm region is unclear. Although our instrument resolution was relatively low, the high-resolution data of Wehrli[69(b)] and of Gedanken, et al.,[78] show that even though vibrational structure is indicated, it cannot be resolved. There is no rotational structure, which indicates that the c band is pre-dissociative (bound state mixed with a dissociative state). The end result of this dissociation is not clear. Maya[71] found no detectable fluorescence resulting from this excitation channel in HgI_2; it, therefore, seems likely that the HgBr formed by c-state predissociation is in some excited state lying above the upper laser level. The absence of observed transitions from high-lying states of HgBr to the B state[79] leads to the conclusion that optical pumping of the $HgBr_2$ (c) state does not contribute to laser operation. The question as to whether this pumping hinders laser-energy extraction by eventual population of the HgBr ground state can be answered by comparing the lifetimes of the c state and the resulting excited HgBr level with the dissociative and radiative lifetimes of the $HgBr_2$ (b) state → HgBr (B) state → HgBr (X) channel. The dissociation lifetime of $HgBr_2$ (b) is measured to be less than 1 nsec,[74] and the

radiative lifetime of $B^2\Sigma$ is on the order of 22 nsec.[80] The dissociative and radiative lifetimes of the higher pump-energy channel—most likely $HgBr_2(c) \rightarrow HgBr\ (C^2\Pi^{1/2}) \rightarrow HgBr(X)$—however, are not well known; therefore, no conclusion can be reached at this time.

Due to the low recorded spectral resolution (~ 0.15 nm per digitized point), the absorption-cross-section values of the c state are not yet reliable. Although the locations and relative magnitudes of the absorption peaks agree fairly well with the high-resolution measurements of Gedanken, et al.,[78] our limited resolution is obvious in an expanded plot. The plot, however, can be improved if the scan rate is decreased. Therefore, the cross-section measurements should be repeated in this wavelength region before the magnitudes can be considered reliable.

The limited accuracy of any absolute value of absorption cross section in the 182 to 186 nm region must be recognized. The existence of the pre-dissociative state implies that some bound-bound transitions do occur (to lower vibration levels of the c state). Therefore, some discrete structure should exist. The fact that our spectrum matches that obtained with a resolution of 0.025 nm indicates that there is much overlap of bound-bound and bound-free transitions. The measured cross-section values, then, represent the integrated values of possibly widely varying cross sections. If the optical pump source is extremely narrow, the absorption cross section may vary markedly from the value measured here. Since the relative heights (peaks and valleys) of our spectra agree quite well with the high-resolution spectra, however, the optical-source linewidth would have to be less than 0.025 nm before variation from our measured cross sections could be expected.

In conclusion, the photoabsorption cross section of $HgBr_2$ vapor has been measured in the spectral range of 175 to 325 nm, although several more measurements should be taken before the values can be considered reliable. The results indicate that optimum laser pumping can be achieved by limiting the photon energy to a wavelength band of ∼ 190 to 205 nm. The scaleability of the photodissociative HgBr laser to high gas pressures and large physical cross section is limited by the magnitude of the photoabsorption cross sections--from ∼ 0.3 to 3.1×10^{-17} cm^2.

SECTION VIII

CONCLUSION

Reliable, long-lifetime, closed-cycle rare-gas lasers have been
developed by employing high-purity, closed-cycle gas-flow systems and
pulsed transverse excitation via thyratron-switched pulsers in low-
inductance configurations.

The novel annular-flow-return laser has significant advantages
over conventional closed-cycle lasers. The design of the flow system
is relatively simple, and the gas-recirculation requirements are signifi-
cantly less than those for an equivalent closed-cycle-loop geometry--by about
a factor of two. The outlook for scaling of the annular-flow-return laser
to longer cavity lengths and to larger volumes appears to be favorable.
The annular return increases the size of a conventional blow-down con-
figuration only slightly. The annular-flow-return geometry lends itself
to implementation of simple heat exchangers when heating or cooling of
the flow is required. The absence of flat surfaces renders this con-
figuration structurally more rugged and more suitable for high-pressure
operation.

The reliability of the closed-cycle atomic-rare-gas lasers is
excellent. The shelf life is at least several months, and the He-Xe
has been operated for $> 10^9$ shots before any system failure.
in addition to the excellent continuous long-term operation
with no degradation of output power.
of the closed-cycle atomic-rare-gas lasers in a pulsed-
preferred in order to permit high-pressure operation

and thereby achieve high peak-power output. At pulse repetition rates greater than the inverse of the clearing time, the discharge is pre-ionized by residual ionization from the previous pulse. The highest pulse repetition rate is determined by discharge stability. However, at the modest pulse powers desired, repetition rates to 12 kHz for long periods (minutes) have been demonstrated. A pulse repetition rate of 5 kHz has been maintained easily for 8 hr.

The previously reported photoabsorption cross section and photo-ionization yield measurements of laser seeding agents have been shown to be free of collector field influences.

The UV scanning monochromator was calibrated, and the UV emission and transmission of CO-laser-mixture spark discharges in the spectral region amenable to the use of ethylene as a seedant were measured. The recorded spectrum of 1:3:9 $CO:N_2:He$ mixture was converted to an equivalent line spectrum for use in the modeling of a CO discharge laser. The UV emission of discharges in CO_2 laser mixtures was measured in order to determine the spectral distribution of radiation generated by the main discharge of a typical CO_2 laser. A method of filtering out the unwanted radiation to the laser windows was discussed.

A coaxial-geometry sliding spark and a planar dielectric-coupled discharge were investigated as preionization sources for the closed-cycle rare-gas laser. At the high repetition rates required, these methods were found to be impractical.

A Xe-flashlamp pumping device was constructed for photolytic excitation studies of mercury-halides. New photoabsorption cross-section measurements of $HgBr_2$ in the spectral range of 175 - 325 nm

have been made, although these should be repeated at higher temperatures before the data can be considered reliable. Results indicate that optimum HgBr laser pumping can be achieved by limiting the photon energy to a wavelength band of ~ 190 - 205 nm.

REFERENCES

1. R. A. Olson, D. Grosjean, B. Sarka, Jr., A. Garscadden, and P. Bletzinger, "High-Repetition-Rate Closed-Cycle Rare Gas Electrical Discharge Laser," Rev. Sci. Instrum. 47 (6), 677 (June 1976).

2. A. Hertzberg and I. R. Hurle, "On the Possible Production of Population Inversions by Gas-Dynamic Techniques," Bull. Am. Phys. Soc. (Series 2) 9, 582 (1964); I. R. Hurle and A. Hertzberg, "Electronic Population Inversions by Fluid Mechanical Techniques," Phys. Fluids 8, 1601 (September 1965); N. G. Basov and A. N. Oraevskii, "Attainment of Negative Temperatures by Heating and Cooling of a Gas System," Sov. Phys.--JETP 17, 1171 (November 1963).

3. J. Wilson, "Nitrogen Laser Action in a Supersonic Flow," Appl. Phys. Lett. 8, 159 (April 1966).

4. A. E. Hill, "Uniform Electrical Excitation of Large-Volume High-Pressure Near-Sonic CO_2-N_2-He Flowstream," Appl. Phys. Lett. 18, 194 (March 1971).

5. T. S. Fahlen, "Discharge Pumped Excimer Lasers," Presented at the 1978 Conference on Laser and Electro-Optical Systems, San Diego, CA, 6-9 February 1978.

6. W. B. Tiffany, R. Targ, and J. D. Foster, "Kilowatt CO_2 Gas-Transport Laser," Appl. Phys. Lett. 15, 91 (August 1969).

7. C. O. Brown and J. W. Davis, "Closed-Cycle Performance of a High-Power Electric-Discharge Laser," Appl. Phys. Lett. 21, 480 (November 1972).

8. D. C. Rabe, AFWAL Aero Propulsion Laboratory, private communication.

9. H. J. Seguin and G. Sedgwick, "Low Voltage Gas Transport TE CO_2 Laser," Appl. Optics 11, 745 (April 1972).

10. A. Eckbreth and F. S. Owen, "Flow Conditioning in Electric Discharge Convection Lasers," Rev. Sci. Instrum. 43 (7), 995 (July 1972).

11. E. Hoag, H. Pease, J. Stall, and J. Zar, "Performance Characteristics of a 10-kW Industrial CO_2 Laser System," Appl. Optics 13 (8), 1959 (August 1974).

12. R. B. Lancashire, D. L. Alger, E. J. Manista, J. G. Slaby, J. W. Dunning, and R. M. Stubbs, "The NASA High-Power Carbon Dioxide Laser: A Versatile Tool for Laser Applications," Opt. Eng. 16 (5), 505 (September/October 1977).

13. H. J. J. Seguin, A. K. Nam, and J. Tulip, "The Photoinitiated Impulse-Enhanced Electrically Excited (PIE) Discharge for High-Power cw Laser Applications," Appl. Phys. Lett. 32 (7), 418 (1 April 1978).

14. J. P. Reilly, "Pulser/Sustainer Electric-Discharge Laser," J. Appl. Phys. 43 (8), 3411 (August 1972).

15. A. E. Hill, "Continuous Uniform Excitation of Medium-Pressure CO_2 Laser Plasmas by Means of Controlled Avalanche Ionization," Appl. Phys. Lett. 22 (12), 671 (June 1973).

16. W. J. Wiegand and W. L. Nighan, "Influence of Fluid-Dynamic Phenomena on the Occurrence of Constriction in cw Convection Laser Discharges," Appl. Phys. Lett. 26 (10), 554 (15 May 1975).

17. W. L. Nighan and W. J. Wiegand, "Causes of Arcing in cw CO_2 Convection Laser Discharges," Appl. Phys. Lett. 25 (11), 633 (1 December 1974).

18. J. A. Beaulieu, "High Peak Power Gas Lasers," Proc. IEEE 59, 667 (April 1971).

19. R. Dumanchin, M. Michon, J. C. Farcy, G. Boudinet, and J. Rocca-Serra, "Extension of TEA CO_2 Laser Capabilities," IEEE J. Quantum Electron. QE-8, 163 (February 1972).

20. C. W. Glanford, M. F. Paris, P. R. Pearson, and D. C. Tyte, "High-Repetition-Rate Operation of a 'Double-Rogowski' TEA CO_2 Laser," IEEE J. Quantum Electron. QE-9, 683 (June 1973).

21. G. S. Dzakowic and S. A. Wutzke, "High-Pulse-Rate Glow-Discharge Stabilization by Gas Flow," J. Appl. Phys. 44, 5061 (November 1973).

22. J. Tulip, H. J. Seguin, and W. Faszer, "High-Repetition-Rate TEA-Laser Discharge Using Integrated Preionization and Switching," IEEE J. Quantum Electron. QE-12 (2), 155 (February 1976).

23. L. M. Laughman, R. J. Wayne, P. P. Chenausky, and C. J. Buczek, "A Compact High PRF Transversely Excited (TE) CO_2 Laser," Presented at the 1978 Conference on Laser and Electro-Optical Systems, San Diego, CA, 6-9 February 1978.

24. J. F. Prince and A. Garscadden, "Negative Ion Species in CO_2-N_2-He Discharges," Appl. Phys. Lett. 27 (1), 13 (1 July 1975).

25. H. Shields, A. L. S. Smith, and B. Norris, "Negative Ion Effects in TEA CO_2 Lasers," J. Phys. D: Appl. Phys. 9, 1587 (1976).

26. J. Thoenes, S. C. Kurzius, and C. M. Cason, "Effects of Closed Cycle CO_2 Electric Discharge Laser Gas Contamination," Presented at the 1978 IEEE International Conference on Plasma Science, Monterey, CA, 15-17 May 1978.

27. P. Bletzinger and C. A. DeJoseph, Jr., "Effect of Oxygen and Hydrogen on Electron Beam Discharges in Atmospheric Pressure CO_2 Mixtures," Presented at the 32nd Gaseous Electronics Conference, Pittsburgh, PA, 9-12 October 1979; P. Bletzinger and C. DeJoseph, Jr., "Plasma Chemical Processes in High-Pressure CO_2 Lasers," Presented at the 4th International Symposium on Plasma Chemistry, Zurich, Switzerland, 27 August-1 September 1979.

28. T. S. Fahlen and R. Targ, "High-Average-Power Xenon Laser," IEEE J. Quantum Electron. QE-9, 609 (1973).

29. T. S. Fahlen, "Pulsed IR Xenon Laser," AFAL-TR-79-1125 (Air Force Avionics Laboratory, Wright-Patterson Air Force Base, OH, July 1979).

30. R. Shuker, A. Szöke, E. Zamir, and Y. Binur, "Energy Transfer in Noble-Gas Mixtures: Penning Ionization in He/Xe," Phys. Rev. A11, 1187 (April 1975).

31. W. T. Silfvast, L. H. Szeto, and O. R. Wood II, "Recombination Lasers in Expanding CO_2 Laser-Produced Plasmas of Argon, Krypton, and Xenon," Appl. Phys. Lett. 31, 334 (September 1977).

32. Y.-J. Shiu, M. A. Biondi, and D. P. Sipler, "Dissociative Recombination in Xenon: Variation of the Total Rate Coefficient and Excited-State Production with Electron Temperature," Phys. Rev. A15, 494 (February 1977).

33. A. Gedanken, J. Jortner, B. Raz, and A. Szöke, "Electronic Energy Transfer Phenomena in Rare Gases," J. Chem. Phys. 57, 3456 (October 1972).

34. S. A. Lawton, J. B. Richards, L. A. Newman, L. Specht, and T. A. DeTemple, "The High-Pressure Neutral Infrared Xenon Laser," J. Appl. Phys. 50, 3888 (June 1979).

35. L. I. Gudzenko, L. A. Shelepin, and S. I. Yakovlenko, "Amplification in Recombining Plasmas (Plasma Lasers)," Sov. Phys.-Usp. 17, 848 (May-June 1975).

36. C. P. Christensen, "High-Repetition-Rate XeF Laser with Gas Recycling," Appl. Phys. Lett. 30 (9), 483 (1 May 1977).

37. T. S. Fahlen, "High-Pulse Rate 10-W KrF Laser," J. Appl. Phys. 49 (1), 455 (January 1978).

38. J. L. Miller, J. Dickie, J. Davin, J. Swingle, and T. Kan, "High Purity Construction Closed Cycle Flow Rare Gas Halide Laser," Preprint UCRL-83032 (Lawrence Livermore Laboratory, Livermore, CA, July 1979).

39. R. A. Tennant, "Chemical Contamination of KrF Lasers," Bidder's Briefing Handout (Los Alamos Scientific Laboratory, Los Alamos, NM, 1978).

40. R. A. Olson and D. F. Grosjean, Closed-Cycle Rare-Gas Electrical-Discharge Laser, Technical Report AFAPL-TR-77-13 (Air Force Aero Propulsion Laboratory, Wright-Patterson Air Force Base, OH, April 1977).

41. H. Egger, M. Dufour, and W. Seelig, "Inhomogeneities in TEA Laser Discharges," J. Appl. Phys. 47, 4929 (November 1976).

42. J. Hsia, "A Model for UV Preionization in Electric-Discharge-Pumped XeF and KrF Lasers," Appl. Phys. Lett. 30, 101 (15 January 1977).

43. A. F. Gibson, K. R. Rickwood, and A. C. Walker, "A Transversely Excited Multiatmosphere CO_2 Waveguide Laser," Appl. Phys. Lett. 31, 176 (1977); P. W. Smith, P. J. Maloney, and O. R. Wood II, "Waveguide TEA Laser," Appl. Phys. Lett. 23, 524 (1973).

44. L. G. H. Huxley and R. W. Crompton, <u>The Diffusion and Drift of Electrons in Gases</u> (John Wiley and Sons, NY, 1974), p. 600.

45. J. N. Bardsley and M. A. Biondi, "Dissociative Recombination," in <u>Advances in Atomic and Molecular Physics</u>, Vol. 6 (D. R. Bates and I. Esterman, eds.) (Academic Press, NY, 1970), p. 1.

46. W. B. Kunkel, "Analysis of Ionic Recombination Including Ion Production during Measurement," Phys. Rev. <u>84</u>, 218 (1951).

47. P. Bletzinger, D. A. LaBorde, W. F. Bailey, W. H. Long, Jr., P. D. Tannen, and A. Garscadden, "Influence of Contaminants on the CO_2 Electric-Discharge Laser," IEEE J. Quantum Electron. <u>QE-11</u> (7), July 1975.

48. R. A. Fitch, "Marx--and Marx-Like--High Voltage Generators," IEEE Trans. Nucl. Sci. <u>NS-18</u> (August 1971).

49. J. J. Lowke, A. V. Phelps, and B. W. Irwin, "Predicted Electron Transport Coefficients and Operating Characteristics of CO_2-N_2-He Laser Mixes," J. Appl. Phys. <u>44</u> (10)(October 1973).

50. P. Felsenthal and J. M. Proud, "Nanosecond-Pulse Breakdown in Gases," Phys. Rev. <u>139</u>, A1796 (1965).

51. O. R. Wood, E. G. Burkhardt, M. A. Pollack, and T. J. Bridges, "High-Pressure Laser Action in 13 Gases with Transverse Excitation," Appl. Phys. Lett. <u>18</u>, 112 (February 1971).

52. P. L. Chapovsky, V. N. Lisitsyn, and A. R. Sorokin, "High-Pressure Gas Lasers on Ar I, Xe I, and Kr I Transitions," Opt. Comm. <u>16</u>, 33 (January 1976).

53. T. Y. Chang, "Improved Uniform-Field Electrode Profiles for TEA Laser and High-Voltage Applications," Rev. Sci. Instrum. <u>44</u> (4), 405 (April 1973).

54. W. Rogowski, Arch. Electrotech. <u>12</u>, 1 (1923); J. D. Cobine, <u>Gaseous Conductors</u> (Dover, NY, 1958).

55. P. Burlamacchi and R. Salimbeni, "XeCl Excimer Laser Using Chlorinated Hydrocarbons as Cl Donors," Optics Commun. <u>26</u>, 233 (August 1978).

56. V. N. Ishchenko, V. N. Lisitsyn, and A. M. Raghev, "Efficient Discharge Pumping XeCl Laser," Optics Commun. <u>21</u>, 30 (April 1977).

57. R. C. Sze and P. B. Scott, "Intense Lasing in Discharge Excited Noble-Gas Monochlorides," Appl. Phys. Lett. <u>33</u>, 419 (1 September 1978).

58. R. Burnham, "Improved Performance of the Discharge-Pumped XeCl Laser," Optics Commun. <u>24</u>, 161 (February 1978).

59. L. Burlamacchi, P. Burlamacchi, and R. Salimbeni, "Long-Life Operation of an XeCl Eximer Laser," Appl. Phys. Lett. <u>34</u>, 33 (1 January 1979).

60. D. F. Grosjean and P. Bletzinger, "Photoionization and Photoabsorption Characteristics of Laser Seed Compounds," IEEE J. Quant. Elec. QE-13, 898 (Nov. 1977).

61. R. I. Shoen, "Absorption, Ionization, and Ion Fragment Cross Sections of Hydrocarbon Vapors under Vacuum-Ultraviolet Radiation," J. Chem. Phys. 37, 9 (Nov. 1962).

62. E. P. Velikhov, E. A. Muratov, V. D. Pis'Mennyi, A. M. Prokhorov, and A. J. Rakhimov, "Atmospheric-Pressure CO_2 Laser with Nonautonomous Discharge Controlled by Ultraviolet Radiation," JETP Lett. 20, 47 (July 1974).

63. J. A. R. Samson, Techniques of Vacuum Ultraviolet Spectroscopy (John Wiley and Sons, NY, 1967).

64. R. L. Kelly and L. L. Palumbo, Atomic and Ionic Emission Lines Below 2000 Å, NRL Report 7599 (Naval Research Laboratory, Washington, D.C., June 1973).

65. U. S. National Aeronautics and Space Administration, U. S. Air Force, U. S. Weather Bureau: "U. S. Standard Atmosphere, 1962," as reported in AIP Handbook, 3rd Edition (American Institute of Physics, NY, 1972), pp. 2-134.

66. See, for example, R. Babcock, I. Liberman, and W. D. Partlow, "Volume Ultraviolet Preionization from Bare Sparks," IEEE J. Quant. Elect. QE-12, 29 (January 1976); B. Norris and A. L. Smith, "Operation of Sliding-Spark Arrays for Laser Preionization," J. Phys. E10, 551 (1977).

67. See, for example, A Laflamme, "Double Discharge Excitation for Atmospheric Pressure CO_2 Lasers," Rev. Sci. Instrum. 41, 1578 (November 1970); J. Lachambre, J. Gilbert, F. Rheault, R. Fortin, and M. Blanchard, "Performance Characteristics of a TEA Double-Discharge Grid Amplifier," IEEE J. Quant. Elec. QE-9, 459 (April 1973).

68. C. R. Tallman, "A Study of Excimer Laser Preionization Techniques," paper WB-4 presented at the Topical Meeting on Excimer Lasers, Charleston, SC, 11-13 September 1979.

69. See, for example, (a) K. Wieland, "Molekülspektren mit Ionencharakter und ihre Beeinflussung durch Fremdgase," Contribution to the Study of Molecular Structures, Vol. Commem. Victor Henri (Maison Desoer, Liege, 1948), pp. 229-238; (b) M. Wehrli, "Electronenbandenspektren der Linearen Moleküle $HgCl_2$, $HgBr_2$, HgJ_2 und $TeCl_2$," Helv. Phys. Act. 11, 339 (1938); (c) K. Wieland, "Bandensysteme $B(^2\Sigma^+) \rightarrow \chi(^2\Sigma^+)$ und Dissoziationswerte der Radikale HgJ und HgBr," Z. Electrchem. 64, 761 (1960).

70. J. H. Parks, "Laser Action on the $B^2\Sigma_{\frac{1}{2}}^+ \rightarrow \chi^2\Sigma_{\frac{1}{2}}^+$ Band of HgCl at 5576 Å," Appl. Phys. Lett. 31, 192 (1 August 1977).

71. J. Maya, "Quantum Efficiency of Fluorescence Excited by Photodissociation in Metal Halide Vapors and Applications," IEEE J. Quant. Elec. QE-15, 579 (July 1979).

173

72. E. J. Schimutschek, J. E. Celto, and J. A. Trias, "Mercuric Dissociation Laser in an Electric Discharge," Opt. Lett. $\underline{2}$, 64 (March 1978).

73. E. J. Schimitschek and J. E. Celto, "Mercuric Bromide Dissociation Laser in an Electric Discharge," Opt. Lett. $\underline{2}$, 64 (March 1978).

74. J. G. Eden, "VUV-Pumped HgCl Laser," Appl. Phys. Lett. $\underline{33}$, 497 (September 1978).

75. J. Maya, "Ultraviolet Absorption Cross Sections of HgI_2, $HgBr_2$, and Tin (II) Halide Vapors," J. Chem. Phys. $\underline{67}$, 4976 (1 December 1977).

76. P. Templet, J. R. McDonald, S. P. McGlynn, C. H. Kendrow, J. L. Roebber, and K. Weiss, "Ultraviolet Absorption Spectra of Mercuric Halides," J. Chem. Phys. $\underline{56}$, 5746 (1 June 1972).

77. R. C. West (ed.), CRC Handbook of Chemistry and Physics, 52nd edition (Chemical Rubber Company, Cleveland, OH, 1971), pp. D-171 - D-177.

78. A. Gedanken, B. Raz, U. Even, and I. Eliger, "The Vacuum UV Spectrum of $HgBr_2$," J. Molecular Spect. $\underline{32}$, 287 (1969).

79. K. P. Huber and G. Herzberg, Constants of Diatomic Molecules (Van Nostrand Reinhond, NY, 1979).

80. R. W. Waynant and J. G. Eden, "HgX(B) Radiative Lifetime by Fast Photolysis of HgX_2 (X = Br, I)," Appl. Phys. Lett. $\underline{33}$, 708 (15 October 1978).

END

DATE
FILMED

9-80

DTIC